ANKARA YILDIRIM BEYAZIT UNIVERSITY

GRADUATE SCHOOL OF NATURAL AND APPLIED SCIENCES



INTEGRATION OF SOL-GEL DERIVED DOPED ZINC OXIDE FILMS AND SOLUTION-PROCESSED METAL NANOPARTICLES FOR THIN FILM PHOTODIODE AND SOLAR CELL APPLICATIONS

Ph.D. Thesis by

Mohamed Nouri SBETA

Department of Electrical and Computer Engineering

May, 2019

ANKARA

INTEGRATION OF SOL-GEL DERIVED DOPED ZINC OXIDE FILMS AND SOLUTION-PROCESSED METAL NPs FOR THIN FILM PHOTODIODE AND SOLAR CELL APPLICATIONS

A Thesis Submitted to

The Graduate School of Natural and Applied Sciences of

Ankara Yıldırım Beyazıt University

In Partial Fulfillment of the Requirements for the Degree of Doctor of Philosophy in Electrical Engineering, Department of Electrical & Computer Engineering

by

Mohamed Nouri SBETA

May, 2019

ANKARA

Ph.D. THESIS EXAMINATION RESULT FORM

We have read the thesis entitled **"INTEGRATION OF SOL-GEL DERIVED DOPED ZINC OXIDE FILMS AND SOLUTION-PROCESSED METAL NPS FOR THIN FILM PHOTODIODE AND SOLAR CELL APPLICATIONS"** completed by **MOHAMED NOURI SBETA** under the supervision of **PROF. DR. ABDULLAH YILDIZ** and we certify that in our opinion it is fully adequate, in scope and in quality, as a thesis for the degree of Ph.D.

Prof. Dr. Abdullah YILDIZ

Supervisor

Prof. Dr. Hüseyin CANBOLAT

Jury Member

Prof. Dr. Sefer Bora LİŞESİVDİN

Jury Member

Prof. Dr. Tülay SERİN

Jury Member

Prof. Dr. Şerafettin EREL

Jury Member

Prof. Dr. Ergün ERASLAN

Director

Graduate School of Natural and Applied Sciences

ETHICAL DECLARATION

I hereby declare that, in this thesis which has been prepared in accordance with the Thesis Writing Manual of Graduate School of Natural and Applied Sciences,

- All data, information and documents are obtained in the framework of academic and ethical rules,
- All information, documents and assessments are presented in accordance with scientific ethics and morals,
- All the materials that have been utilized are fully cited and referenced,
- No change has been made on the utilized materials,
- All the works presented are original,

and in any contrary case of above statements, I accept to renounce all my legal rights.

Date: 13.05.2019 **Signature:**

Name & Surname: Mohamed Nouri SBETA

ACKNOWLEDGMENTS

I would like to express my sincere gratitude to my supervisor, Prof. Dr. Abdullah YILDIZ for his tremendous support and motivation during my study. His immense knowledge and precious recommendations constituted the milestones of this study. His guidance assisted me all the time of my research and while writing this thesis.

My thanks to all friends in Prof. Abdullah' group for their help and moral support which encouraged me to finalize this work.

My gratitude and deep thanks to my wife for bearing my burden and for her unlimited support and continued encouragement throughout this work.

May, 2019 **Mohamed Nouri SBETA**

INTEGRATION OF SOL-GEL DERIVED DOPED ZINC OXIDE FILMS AND SOLUTION-PROCESSED METAL NPs FOR THIN FILM PHOTODIODE AND SOLAR CELL APPLICATIONS

ABSTRACT

The thesis work aimed at deposition, characterization, and optimization of sol-gel-derived undoped ZnO, Al-doped ZnO (AZO) and Ga-doped ZnO (GZO) thin films with emphasizing on GZO films. The films were successfully deposited on glass substrates using spin coating technique and their optical and electrical properties were optimized in order to be eligible for optoelectronic devices applications. By the deposition of GZO films on p-Si substrate, p-n heterojunctions (GZO/p-Si) were successfully formed and GZO/p-Si based optoelectronic devices were fabricated and optimized. The enhancement potential in the optical response of GZO/p-Si devices via metal nanoparticles (NPs) was investigated by spin-coating of solution-processed 100 nm size Ag and Au NPs on GZO layer.

The structural, surface morphological, optical, and electrical properties of the deposited ZnO thin films were investigated using x-ray diffractometer (XRD) and scanning electron microscope (SEM), atomic force microscopy (AFM), UV-vis spectroscopy, and the four-point probe and Hall effect measurement systems, respectively. The ratio of the electrical conductivity to the absorption coefficient was used as a figure of merit (*FOM*) for evaluating the quality of films. *FOM* value of ~1.6×10^{-5} Ω^{-1} was measured for the deposited AZO and GZO thin films.

The performance of GZO/p-Si devices were analyzed from the current-voltage (*I-V*) characteristics measured in the dark and under AM1.5 and UV illumination conditions. Compared to literature, excellent rectification behavior, high photoresponsivity and competitive photovoltaic property were exhibited by the devices. The inclusion of Au and Ag metal NPs into the devices led to enhanced optical absorption and consequently improved the performance of the devices in terms of photoelectric properties.

Keywords: Sol-gel method, AZO thin films, GZO thin films, metal nanoparticles, photodiode, photovoltaic.

İNCE FİLM FOTODİYOT VE GÜNEŞ HÜCRESİ UYGULAMALARI İÇİN SOL-JEL YÖNTEMİYLE ELDE EDİLEN KATKILI ÇİNKOKSİT FİLMLERİ VE ÇÖZELTİ-İŞLEMLİ METAL NP'LARIN ENTEGRASYONU

ÖZ

Tez çalışmasında, sol-gel türevli ZnO, Al-katkılı ZnO (AZO) ve Ga-katkılı ZnO (GZO) ince filmlerin GZO filmleri üzerinde durulması, biriktirilmesi ve optimizasyonu amaçlanmıştır. Filmler, spin kaplama tekniği kullanılarak cam substratlar üzerinde başarıyla biriktirildi ve optik ve elektriksel özellikleri, optoelektronik cihaz uygulamaları için uygun olacak şekilde optimize edildi. GZO filmlerinin p-Si substratına biriktirilmesiyle, p-n (GZO/p-Si) heterojeksiyonları başarıyla oluşturuldu ve GZO/p-Si bazlı optoelektronik cihazlar imal edildi ve optimize edildi. GZO/p-Si cihazlarının metal nanoparçacıklar (NP'ler) vasıtasıyla optik tepkisinde gelişme potansiyeli, GZO tabakası üzerinde işlenen 100 nm boyunda Ag ve Au NP'lerin döndürülerek kaplanmasıyla incelenmiştir.

Depolanan ZnO ince filmlerin yapısal, yüzey morfolojik, optik ve elektriksel özellikleri x-ışını difraktometresi (XRD) ve taramalı elektron mikroskobu (SEM), atomik kuvvet mikroskobu (AFM), UV-vis spektroskopisi ve dördü kullanılarak incelenmiştir. puanlı prob ve Hall efekt ölçüm sistemleri. Elektriksel iletkenliğin emme katsayısına oranı, filmlerin kalitesini değerlendirmek için bir değer (FOM) olarak kullanılmıştır. Depolanan AZO ve GZO ince filmleri için ~ 1.6×10^{-5} Ω^{-1} FOM değeri ölçüldü.GZO/p-Si cihazlarının performansı karanlıkta ve AM1.5 ve UV aydınlatma koşullarında ölçülen akım-gerilim (*I-V*) özelliklerinden analiz edildi. Literatür ile karşılaştırıldığında, mükemmel düzeltme davranışı, yüksek fotoreopozivite ve rekabetçi fotovoltiac özelliği cihazlar tarafından sergilendi. Au ve Ag metal NP'lerinin cihazlara dahil edilmesi, optik absorpsiyonun artmasına neden oldu ve sonuç olarak cihazların fotoelektrik özellikler bakımından performansını arttırdı.

Anahtar kelimeler: Sol-gel yöntemi, AZO ince filmler, GZO ince filmler, metal nanopartiküller, fotodiyot, fotovoltaik.

CONTENTS

Ph.D. THESIS EXAMINATION RESULT FORM ii

ETHICAL DECLARATION iii

ACKNOWLEDGMENTS iv

ABSTRACT v

ÖZ vi

NOMENCLATURE ix

LIST OF TABLES xi

LIST OF FIGURES xii

CHAPTER 1: INTRODUCTION 1

CHAPTER 2: THEORETICAL BASES 6

2.1 Zinc oxide (ZnO) semiconductor 6

2.2 Sol-gel preparation of ZnO thin films 8

2.2.1 Sol-Gel process 8

2.2.2 Deposition of ZnO thin films 9

2.3 Plasmonic effect of metal NPs 13

2.4 ZnO/p-Si heterojunction-based diode 15

2.4.1 ZnO-based solar cell 18

2.4.2 ZnO-based Photodiode 21

CHAPTER 3: EXPERIMENTAL WORK 23

3.1 Deposition and characterization of ZnO:X films and metal NPs 23

3.1.1 Deposition process 23

3.1.1.1 Deposition of ZnO:X thin films 23

3.1.1.2 Deposition of metal NPs (Au and Ag) 31

3.1.2 Properties characterization measurements 32

3.2 Fabrication and characterization of GZO/p-Si heterojunction-based 47

3.2.1 Fabrication process 47

3.2.2 Performance characterization measurements 51

CHAPTER 4: RESULTS AND DISCUSSION 55
4.1 Deposited ZnO:X thin films 55
4.1.1 Al-doped ZnO (AZO) thin films 55
4.1.2 Ga-doped ZnO (GZO) thin films 63
4.2 Fabricated GZO/p-Si heterojunction-based devices 78
4.2.1 Basic devices 78
4.2.2 Metal NPs-coated devices 85
CHAPTER 5: CONCLUSION 89
REFERENCES 93
CURRICULUM VITAE 101

NOMENCLATURE

Acronyms

AFM	Atomic Force Microscopy
AR	Anti-Reflection
at.	Atomic
AZO	Al-doped ZnO
DEA	Diethanolamine
DI	De-Ionized
DP	Dopant Precursor
DR	Doping Ratio
FOM	Figure Of Merit
FWHM	Full Width at Half Maximum
GZO	Ga-doped ZnO
LPCVD	Low Pressure Chemical Vapor Deposition
MEA	Monoethanolamine
p-Si	p-type Silicon
PV	Photovoltaic
RMS	Root Mean Square
rpm	Revolution per minute
SEM	Scanning Electronic Microscope
SM	Solution Molarity
TCO	Transparent Conductive Oxide
TEA	Triethylamine
TeA	Triethanolamine
TFT	Thin Film Transistor
UV	Ultraviolet
UV-vis	Ultraviolet-visible
XRD	X-Ray Diffractometer
ZAD	Zinc Acetate Dihydrate

Roman Letter Symbols

ΔE_c	Conduction band offset
ΔE_g	Bandgap energy difference
ΔE_v	Valence band offset
A	Area
A	Absorbance
A^*	Theoretical Richardson constant
a, c	Lattice constant of films
C_j	Junction capacitance
c_o	Lattice constant of bulk
D	Grain size
d	Thickness
D_n	Minority carrier electron diffusion coefficient (cm2/s)
D_p	Minority carrier hole diffusion coefficient (cm2/s)
e	Electron charge
E_f	Fermi energy
E_g	Bandgap energy
f_{3db}	Frequency at 3 decibels
FOM	Figure of merit
FF	Fill factor
G	Generation rate of electron-hole pairs
$g(x)$	Generation function at depth x
I_d, J_d	Diode current, diode current density
I_L, J_L	Light current, light current density
I_{mp}, J_{mp}	Current, current density at maximum power point
I_o, J_o	Reverse saturation current, reverse saturation current density
I_{sc}, J_{sc}	Short circuit current, short circuit current density
k	Boltzmann's constant
L_n	Minority carrier electron diffusion length (cm)
L_p	Minority carrier hole diffusion length (cm)
n	Refractive index or ideality factor
N_A	Avogadro's number
n_{po}	Thermal-equilibrium minority electron concentration (cm-3)
P	Porosity
P_{in}	Input power

P_{max}	Maximum power
p_{no}	Thermal-equilibrium minority hole concentration (cm-3)
PR	Photoresponsivity
PS	Photosensitivity
R	Reflectance
R_s	Series resistance
R_{sh}	Shunt resistance
T	Temperature
T	Transmittance
TC	Texture Coefficient
t_r	Rise time
V_{mp}	Voltage at maximum power point
V_{oc}	Open circuit voltage
W	Width of depletion region

Greek Letter Symbols

α	Absorption coefficient
β	Full width of half maximum (FWHM)
χ_{Si}	Electron affinity of Si
χ_{ZnO}	Electron affinity of ZnO
ε	Strain
Φ	Work function
ϕ_{bi}	Built-in contact barrier potential
ϕ_{bn}	Barrier potential for electrons
ϕ_{bo}	Zero bias built-in barrier potential
ϕ_{bp}	Barrier potential for holes
η	Efficiency
λ	Wavelength
μ_n	Electron mobility
μ_p	Hole mobility
θ_B	Bragg angle
ρ	Electric resistivity
σ	Electric conductivity

LIST OF TABLES

Table 3.1 The investigated parameters of Sol-Gel process ……. 23

Table 3.2 List of chemicals used for preparation of coating solutions …… 29

Table 3.3 Typical recipe for deposition of 3 at. % Ga-doped ZnO (GZO) thin film ……... 30

Table 3.4 Specifications of the used dispersions of Au and Ag NPs ……... 31

Table 3.5 Systems of characterization measurements ……..... 32

Table 4.1 The estimated parameters for the AZO films of various solvent-stabilizer combinations ……. 56

Table 4.2 The estimated parameters for the deposited AZO films of various doping ratios ……... 60

Table 4.3 The estimated values of some physical parameters for the GZO films …..... 65

Table 4.4 Some physical parameters of GZO films with varying spin acceleration time 70

Table 4.5 The investigated parameters and their best results for GZO/p-Si devices …. 78

Table 4.6 Some physical parameters for GZO layer of GZO/p-Si device ……. 83

Table 4.7 GZO/p-Si diode parameters in the dark ……... 84

Table 4.8 Bare and metal NPs-coated GZO/p-Si diodes parameters in the dark and their photoresponsivity under UV illumination ……. 88

Table 4.9 PV parameters under AM1.5 illumination for bare and metal NPs-coated GZO/p-Si devices ……. 88

LIST OF FIGURES

Figure 2.1 The wurtzite crystal structure of ZnO with the lattice parameters *a* and *c* ……..……. 6

Figure 2.2 Schematic diagram of various paths in the sol-gel method ……... 8

Figure 2.3 Interrelation representation for the reactions of hydrolysis and condensation involved in the sol-gel process which lead to formation of moieties Zn-oxo acetate colloidal starting from ZAD …… 11

Figure 2.4 Schematic representation of typical spin-coating process ……..… 11

Figure 2.5 A typical profile for spinning speed ……..…. 12

Figure 2.6 Light trapping by forward scattering from metal nanoparticles at the surface of the absorbing semiconductor thin film ……..… 13

Figure 2.7 The light interaction with a metallic NP ……..... 14

Figure 2.8 Oscillation amplitude for a linear oscillator as a function of the external force frequency (a), and optical absorption spectrum corresponding to 30 nm Ag NPs embedded in a silica glass (b) …… 14

Figure 2.9 Optical absorption spectra for Ag and Au NPs of different sizes ….. 15

Figure 2.10 Schematic diagram n-ZnO/p-Si heterojunction-based photoelectric device (a), and energy band diagram of n-ZnO/p-Si junction at equilibrium (b) ……..……. 16

Figure 2.11 The equivalent circuit of an ideal solar cell (a), and a solar cell with a series resistance, R_s and a shunt resistance, R_{sh} (b) ……..…… 20

Figure 2.12 The equivalent circuit of a photodiode (a) and the reverse bias characteristic *J-V* curves of photodiode under dark and light conditions (b) ……..... 22

Figure 3.1 Flow chart of Sol-Gel method for fabrication of ZnO:X thin films .. 24

Figure 3.2 Steps of chemical synthesis process ……..……. 27

Figure 3.3 XRD measurement schematic ……...…. 33

Figure 3.4 Rigaku Miniflex 600 XRD measurement system (a), XRD pattern of a deposited ZnO thin film (b) ……..… 34

Figure 3.5 Schematic of a Scanning Electron Microscope ……..…… 35

Figure 3.6 FEI QUANTA 400F brand SEM system (a), SEM image of a deposited GZO thin film (b) ……. 36

Figure 3.7 AFM schematic …….…… 37

Figure 3.8 Q-Scope 250 brand AFM system (a), AFM image of a deposited GZO thin films (b) ……..…… 37

Figure 3.9 UV-Visible spectroscopy schematic ……..…… 38

Figure 3.10 UV-170 SHIMADZU brand UV-vis spectroscopy system (a), measured transmittance spectrum of a deposited GZO thin film (b) 39

Figure 3.11 Measured transmittance spectrum with generated maxima and minima envelopes of a deposited GZO thin film ……..…. 40

Figure 3.12 Tauc's bandgap energy of a deposited GZO film ……..…… 42

Figure 3.13 Layout of four-point probe measurement method (a), Setup of the measurement system (b) ……..…... 43

Figure 3.14 Schematic of Hall effect measurement (a), Nano Magnetics Hall effect measurement system (b) ……..…. 44

Figure 3.15 Schematic diagram of basic structure (a) and metal NPs-coated structure (b) of n-GZO/p-Si heterojunction-based device ……..… 46

Figure 3.16 Fabrication sequence for n-GZO/p-Si heterojunction-based devices 47

Figure 3.17 Dicing of Si wafers ……..... 47

Figure 3.18 Metallization process schematic …….….... 49

Figure 3.19 Measured *I-V* characteristics of Ag/GZO front contact (a), and Al/p-Si back contact (b) ……..…. 50

Figure 3.20 Four-wire configuration for *I-V* measurement using Keithley 2400 SMU ……..…. 51

Figure 3.21 Sun simulator measurement setup (a), Dark and Light *I-V* characteristics of a fabricated device (b) ……..……. 51

Figure 3.22 Dark and Illuminated *I-V* characteristics of a standard solar cell ….. 53

Figure 4.1 XRD patterns for the AZO films of various solvent-stabilizer combinations ……..…… 57

Figure 4.2 AFM images for the AZO films of the various solvent-stabilizer combinations ……..…. 58

Figure 4.3 Optical transmittance spectra for the AZO films of various solvent-stabilizer combinations, the Tauc's graph is shown in the inset …… 59

Figure 4.4 The measured XRD patterns for the deposited AZO thin films of various doping ratio ……..…. 61

Figure 4.5 Optical transmittance spectra for the AZO films of various doping ratios, the Tauc's graph is shown in the inset …… 62

Figure 4.6 Average visible transmittance, electrical resistivity and figure of merit vs doping ratio for the AZO films …… 63

Figure 4.7 XRD patterns for the GZO films of various doping ratios …… 66

Figure 4.8 AFM images for the GZO films of various doping ratios ……..… 66

Figure 4.9 Optical transmittance spectra for the GZO films of various doping ratios, the Tauc's graph is shown in the inset …… 67

Figure 4.10 Average visible transmittance, electrical resistivity and figure of merit vs doping ratio for the GZO films …… 68

Figure 4.11 X-ray diffraction patterns for GZO films deposited at different spin acceleration time. Inset shows an enlarge (002) peak of the films … 71

Figure 4.12 The two-dimensional AFM micrographs ($15 \times 15\ \mu m^2$) for the GZO films with different spin acceleration time, as indicated inside the pictures ……..……. 72

Figure 4.13 SEM micrographs of GZO films at various spin acceleration time, as indicated inside the pictures ……..……. 73

Figure 4.14 Optical transmittance of GZO films as a function of wavelength. $(\alpha h\nu)^2$ as a function of photon energy $h\nu$, and the band gap as a function of spin acceleration time are shown in the inset ……..…. 74

Figure 4.15 Dependence of the thickness and the porosity on spin acceleration time for GZO films ……..... 75

Figure 4.16 Resistivity of GZO films with various spin acceleration time …..…. 77

Figure 4.17 Electrical resistivity vs doping ratio of GZO films (a), cross-sectional SEM image for two cycles spin-coated GZO film on Si substrate (b) ……...…. 79

Figure 4.18 The measured XRD pattern for the GZO film deposited on Si substrates. The insets are the surface SEM (a) and AFM (b) images for the film ……..… 81

Figure 4.19 The measured transmittance spectrum for the GZO film deposited on glass substrate. The inset is Tauc's plot for the film …….… 82

Figure 4.20 Semi-log *I-V* characteristics in the dark and under UV and AM1.5 illuminations (a), linear *I-V* characteristics in the dark (b), and the PV characteristics under AM1.5 illumination (c) for the device ….... 84

Figure 4.21 The measured absorbance spectra for the Ag and Au NPs-contained dispersions. The inset is a SEM image of the top surface of the 100 nm Au NPs deposited on the GZO-coated Si substrate …….… 87

Figure 4.22 Semi-log *I-V* characteristics in the dark and under the illumination of AM1.5 and UV (reverse bias region only) (a), linear *I-V* characteristics in the dark (b), and the PV characteristics under AM1.5 illumination (c) for the metal NPs-coated devices …… 88

CHAPTER 1

INTRODUCTION

Recently, zinc oxide (ZnO) has received a considerable attention from the scientific researchers as a promising semiconducting material of wide range of applications. ZnO is characterized by various distinguished properties such as high transparency for visible light, high electron mobility, high thermal conductivity, large free exciton binding energy, large piezoelectric constants, surface conductivity of high sensitivity to the presence of adsorbed species, and many others [1]. In principle, being ZnO is a direct wide band gap semiconductor, it enables optoelectronic applications in the blue and UV regions of the light spectrum. Combined with its other properties, ZnO is useful for fabricating many devices such as gas sensors, transducers, actuators, transparent thin-film transistors (TFT), photodiodes, thin film solar cells and many others [1]. For solar cell devices, ZnO can be used for different functions such as a transparent conductive oxide (TCO) layer, an active n-type semiconductor layer, an antireflection coating layer and a transparent buffer (window) layer.

The undoped ZnO has native n-type conductivity and the group-III impurities B, Al, Ga and In can act as shallow donors in ZnO enhancing its n-type conductivity in a stable manner. Among these dopants, Ga is considered a superior one since it is maintaining the high transparency of ZnO films after the doping process [2], it is not reactive with oxygen as much as others and it has relatively less lattice distortion with good electrical conductivity as well [3]. The undoped and doped ZnO thin films can be deposited using different methods and techniques such as sputtering, low pressure chemical vapor deposition (LPCVD), atomic layer deposition (ALD), Sol-Gel process, and many others. Among these methods, Sol-Gel method is the most readily controllable, and offers several other advantages including low temperature processing, possibility of coating on large area substrates, higher specific surface area, superior homogeneity and purity, better microstructural control of metallic particles, narrow pore size and uniform particle distribution and naturally, and most importantly, cost effectiveness [4]. A theoretical background on fundamentals of ZnO semiconductor and sol-gel preparation of ZnO thin films is given in chapter 2.

In literature, there are many published works on sol-gel-derived undoped and doped ZnO thin films [5-14]. The structural, optical and electrical properties of obtained ZnO thin films can differ considerably according to the change in the experimental conditions. Generally, tuning some experimental deposition conditions of sol-gel process such as annealing temperature [14], spin speed [15], substrate [16], solvent [17], stabilizer [18], and others lead to significant modifications in the properties of ZnO films. Such a control in its properties makes the ZnO material a good candidate for many different applications. This can particularly be vital for device applications of ZnO where these modifications can significantly affect the performance of devices. For instance, while the electrical conductivity of ZnO films can generally be improved with increasing the annealing temperature due to the improved crystal quality, however a shrinking or widening in band gap energy (E_g) of these films can be occurred [19, 20]. This demonstrates that any change in one parameter can affect the other parameters. This kind of interrelation among the parameters makes it almost impossible to control one parameter independent of the others by changing only one experimental condition of the deposition process. Despite the rather good knowledge of the effect of various deposition parameters on the properties of ZnO films deposited by sol-gel method using spin-coating technique, a gap exits in literature regarding the effect of spin-coating acceleration time (t_{acc}) parameter. According to our survey, there is no study in literature has addressed the various mechanisms dictating the unusual change in the properties of ZnO films with varying t_{acc}. As an original work in this thesis, an experimental study was carried out to investigate the influence of t_{acc} on the properties of Ga-doped ZnO (GZO) thin films deposited by a spin-coating process. The experimental details and results of this study are given in chapter 3.

The first stage of this thesis aimed at deposition, characterization and optimization of sol-gel-derived undoped ZnO and Al, Ga and B-doped ZnO (ZnO:X) thin films with emphasizing on Ga-doped ZnO (GZO) thin films. The objective is to obtain doped ZnO thin films of high transparency and conductivity that can be eligible for optoelectronic devices applications. In the second stage of this thesis, the optimized GZO thin films are used for the fabrication of photoelectric devices based on GZO/p-Si heterostructure. The details of the experimental work carried out for the deposition

of ZnO thin films are described in chapter 3, and the obtained results are presented and discussed in chapter 4.

Due to their various advantages, ZnO/p-Si heterojunction-based photoelectric devices have recently received a growing interest from the scientific research community [21, 22]. In addition to the distinguished properties of ZnO, the simple fabrication process, low temperature process of the deposition of ZnO films, and abundance and non-toxicity of ZnO make these devices promising for many applications and candidate to be an alternative to Si-based homojunctions for optoelectronic applications [21]. A theoretical background on ZnO/p-Si heterojunction-based diodes and their operation as photodiodes and solar cells are given in chapter 2. For the ZnO/p-Si heterojunction-based photodiodes and solar cells, the incident light is absorbed and converted to photogenerated carriers. The high energy photons can be absorbed in the ZnO layer, while the low energy photons transmitted through the ZnO layer can be absorbed in the p-Si substrate [21, 23]. In addition to act as front active n-type semiconductor, ZnO can also act as antireflection coating for Si providing simpler fabrication processing and cost saving [24].

Based on simulation study, B. Hussain et al. [24] showed that conversion efficiency (η) of 19 %, short circuit current (I_{sc}) of 37.7 mA and open circuit voltage (V_{oc}) of 622 mV are anticipated under the optimized parameters for the ZnO:Ga/p-Si heterojunction-based solar cell. However, such high performance for ZnO/p-Si heterojunction-based solar cells is far out of reach experimentally so far. Practically, there are many issues such as quality and parameters of ZnO layer, lattice mismatch between ZnO and p-Si, top surface recombination, optical properties and some others can determine the performance of these devices. The high quality ZnO layer of optimized thickness and doping ratio is the most crucial issue that determines the performance of ZnO/Si heterojunction-based devices. Such a high quality ZnO layer can full fill the main requirements for high performance device such as the low concentration of bulk defect states, high carrier concentration, low sheet resistance and good optical properties. Reducing the concentration of the defect states at the ZnO/Si junction interface and top surface of ZnO layer is another important issue affecting the collection of photogenerated carriers. Introducing an intermediate buffer layer between ZnO and p-Si and top surface passivation layer can partially realize this target.

Application of light trapping techniques can improve the optical properties of device and enhance its response to the incident light [21, 25-29]. Experimentally, figures of 130 mV and 128 μA for I_{sc} and V_{oc}, respectively, were reported by H. Bo et. al. for Al-doped ZnO (AZO)/p-Si heterojunctions fabricated by direct-current (DC) magnetron sputtering [32]. I_{sc} of 194 μA/cm^2 and V_{oc} of 320 mV were the best results achieved by Weiying Z. et al. for n-AZO/p-Si heterojunctions prepared by direct current reactive sputtering [27].

There are many studies in literature on ZnO/p-Si photodiodes. In contrast to the conventional Si-based photodiode, the ZnO film improves the photodiode's responsivity in the UV/blue region. Therefore, ZnO-based photodiodes can be superior for UV illumination applications and they are generally UV photodiodes. photosensitivity (*PS*), photoresponsivity (*PR*) and temporal photoresponse behavior are the main measures used to judge the performance of photodiodes. *PS* of 7.56×10^3 and average *PR* of 0.10 A/W at -3V under 100 mW/cm^2 AM1.5 illumination were reported by S. Karatas et al. for Ru-doped ZnO/p-Si photodiodes fabricated by the Sol-gel Method [30]. S. K. Singh et al. achieved higher *PR* of 0.26 A/W at -2V under 365 nm wavelength UV illumination of 650 μW/cm^2 light intensity for RF-sputtered ZnO/Si heterojunction photodiode [31]. Strong *PR* of 0.5 A/W for 310 UV illumination under a -30V bias was reported by I. Jeong et al. for n-ZnO/p-Si structure [23].

As previously mentioned, many issues can be considered for improving the performance of ZnO/Si heterojunction-based devices. One alternative is to trap incident light inside the device which extends the optical path of the light providing higher absorption possibility. Application of light trapping techniques can permit reducing the physical thickness of active layer while keeping it optically thick leading to material saving and consequently cost reduction. This issue is more important for thin film-based photoelectric devices. Many techniques such as surface texturing, antireflection coating and back reflection have been used for maximum use of incident light. Recently, metal nanoparticles (NPs) such as Ag and Au NPs have been employed in this regard [32, 33]. Metallic nano-structuring performing plasmonic effect can be used as subwavelength scattering elements to couple and trap the incident light into the device. Some parameters of NPs such as size, distribution and location in the device

structure can affect their potential for light trapping. A theoretical background on plasmonic effect of metal NPs is given in chapter 2.

In additional to the enhancement in the optical properties, embedding the metal NPs into the top surface of n-ZnO/p-Si heterojunction-based device can reduce the sheet resistance of ZnO film leading to reduced series resistance [21]. An increase in photogenerated current by factor of 1.35 was reported by Y.-U. Ko et *al.* for n-ZnO/p-Si heterojunction diode, via embedding Ag nanoparticles into device structure [21]. P. Shokeen et *al.* reported an increase in the short circuit current density by factor of 470 % for a ZnO/p-Si heterojunction solar cell with depositing Ag nanoparticles on the top surface of the cell [34]. For incorporating metal NPs into the device structure, different methods such as drop-casting, dip coating and spin coating have been established [35, 36]. In the thesis work, since the ZnO:X are deposited by the spin coating technique, the same technique is used for coating the metal NPs using solution-processed metal NPs. Using similar process for fabricating both the ZnO:X thin films and metal NPs can facilitate their integration and give an advantage to the thesis work.

Despite the many published papers on ZnO/p-Si heterojunction-based diodes, the published papers on GZO/p-Si heterojunction structures are remarkably few [37, 38]. In addition, according to our survey, no study in the literature has investigated the GZO/p-Si heterojunction-based photoelectric diode with the incorporation of metal NPs. The second stage of this thesis aimed at fabrication and optimization of GZO/p-Si heterojunction-based diodes work as photodiodes and solar cells devices. Employing the metal NPs for enhancing the optical response of these devices is investigated through fabricating devices of top surface coated with metal NPs. The details of the experimental work carried out for the fabrication of devices are described in chapter 3, and the obtained results are presented and discussed in chapter 4. The thesis documentation is ended with the chapter 5, which documents the conclusions arisen from the entire thesis work.

CHAPTER 2

THEORETICAL BASES

2.1 Zinc oxide (ZnO) semiconductor

ZnO is a direct wide bandgap semiconducting material (typically 3.37 eV at room temperature [39]) which crystallizes in the wurtzite structure (Figure 2.1). It can be grown as a single crystal or polycrystalline material in the form of bulk or thin film. ZnO is characterized with many distinguished properties such as high transparency for visible light, high electron mobility, high thermal conductivity, large free exciton binding energy, large piezoelectric constants, surface conductivity of highly sensitive to the presence of adsorbed species and many others [1]. In addition, the band gap of ZnO can be engineered by adding Mg or Cd. An increase and a decrease in the bandgap can be achieved by adding Mg to ZnO and Cd to ZnO, respectively. MgZnO and CdZnO alloys of moderate concentrations assume the wurtzite structure of ZnO with band gaps in the range of 2.3 to 4.0 eV [40, 41].

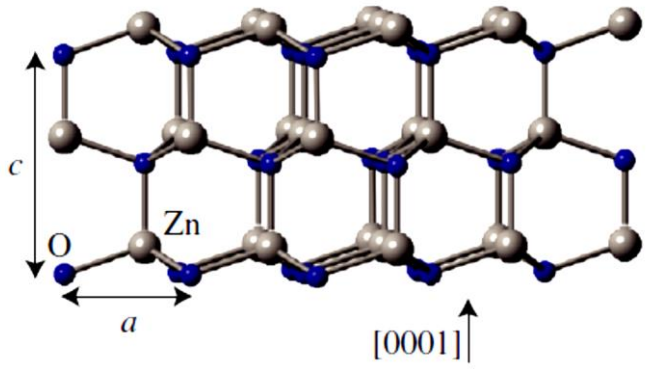


Figure 2.1: The wurtzite crystal structure of ZnO with the lattice parameters *a* and *c*.

The intrinsic (undoped) ZnO exhibits native n-type conductivity caused by the native (intrinsic) defects. These defects are imperfections in the crystal lattice that involve only the constituent elements. They include vacancies (missing atoms at regular lattice positions), interstitials (extra atoms occupying interstices in the lattice) and antisites (a Zn atom occupying an O lattice site or vice versa). Native defects can strongly influence the electrical and optical properties of ZnO and affect some parameters such

doping efficiency, minority carrier lifetime and luminescence efficiency [42]. The n-type conductivity of ZnO can be improved by the single doping or co-doping process. The group-III impurities such as Boron (B), Aluminum (Al), Gallium (Ga) and Indium (In) can act as shallow donors in ZnO and enhance its n-type conductivity in a stable manner. Carrier concentration up to $8x10^{20}$ and $3.7x10^{20}$ cm^{-3} were experimentally observed for ZnO with Al and Ga doping, respectively [43, 44]. In contrary, p-type doping of ZnO using acceptor impurities is found to be very difficult. ZnO of stable and reproducible p-type conductivity has not yet achieved and identifying the key factors for resolving this issue is still challenging [45]. In addition to the electrical properties, the doping process can strongly influence the structural and optical properties of ZnO. Generally, no absolute judgement for the quality of ZnO films and their properties are modified according to targeted application.

The many distinguished properties of ZnO make it suitable for wide range of applications. In principle, ZnO with its direct wide band gap is a suitable material for various optoelectronic applications in the blue and UV regions of the light spectrum. Combined with its other properties, ZnO is useful for fabricating many devices such as transparent thin-film transistors (TFT), photodiodes, thin film solar cells, gas sensors, transducers, actuators and many others [1]. In these devices, ZnO can play different roles, for instance, it can act as a transparent conductive oxide (TCO) layer, an active n-type semiconductor layer and a transparent window.

Single crystal ZnO with a high degree of purity is only required for some advanced applications, and for most of its technological applications. ZnO is generally used in the form of polycrystalline films with relatively less crystalline quality or purity [1]. ZnO polycrystalline films are obtained with a variety of deposition methods and techniques including sputtering technique, low pressure chemical vapor deposition (LPCVD), atomic layer deposition (ALD), chemical spray pyrolysis, electrochemical deposition, sol-gel synthesis and some others. Among these methods, sol-gel method is the most readily controllable, and offers several other advantages such as low temperature processing, the possibility of coating on large area substrates, higher specific surface area, superior homogeneity and purity, better microstructural control of metallic particles, uniform particle distribution and naturally, most importantly, cost effectiveness [4].

2.2 Sol-Gel preparation of ZnO thin films

2.2.1 Sol-Gel process

Sol-gel process is classified as a wet chemistry method where an oxide network is growth from molecular precursors through reactions of hydrolysis-condensation. Evolution of oxide network in a continuous liquid form (gel) takes place through a gelation of a colloidal suspension (sol) [46]. This method allows processing materials as thin films, ceramics and powders directly from the synthetized solution. Figure 2.2 presents a schematic diagram shows the various paths of sol-gel method for processing different forms of materials.

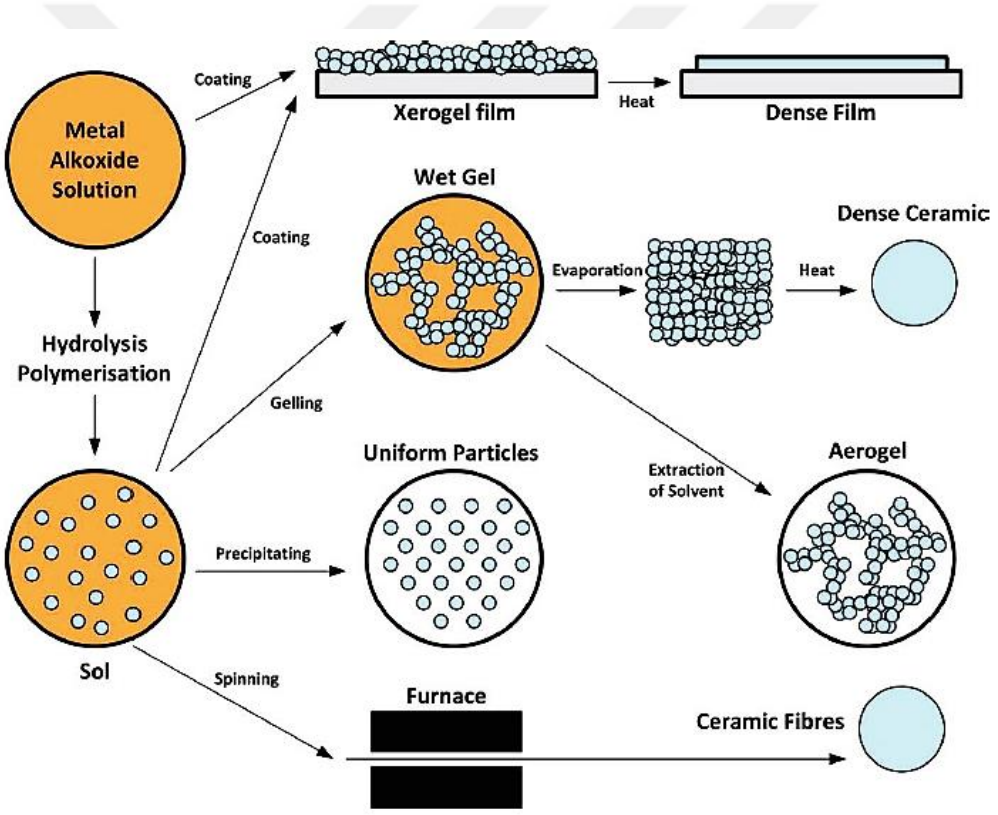


Figure 2.2: Schematic diagram of various paths in the sol-gel method [46].

The films are formed by depositing the prepared solution mixture over the substrates by means of dipping, spinning or spraying. The solution will dry during the deposition time as the solvent evaporates resulting densified films. In order to achieve the required oxide composition and crystallinity, a thermal treatment should be applied at well-defined conditions.

Achieving good homogeneity is an essential requirement for the solution state in order to provide the advantages for preparing a pure-phase material at low synthesis temperatures [47]. The deposition of sol-gel derived thin films is performed by main steps include the preparation of solution mixture (coating solution), coating the prepared solution on the substrate using the selected technique, and the application of pre-heating and annealing processes for the deposited films. Each step has its parameters that can affect the quality of the deposited thin films. Some of these parameters are the precursor's form and concentration, the used of solvent and stabilizer, the coating process conditions, the type of substrate, and the conditions of the pre-heating and annealing processes

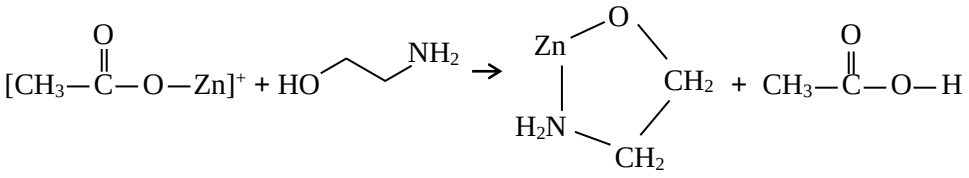
2.2.2 Deposition of ZnO thin films

Sol-Gel method has been widely used for the preparation and deposition of ZnO thin films [48]. The films are prepared by coating of the precursor solution over the substrates by means of spraying, dipping or spinning. Nitrates, chlorides and acetates were used as sol-gel precursors for ZnO, providing thin films with different morphological features and crystallization. Zinc nitrate and chloride present high solubility in water or organic solvents, but one main draw Sol-Gel method is used widely for the derivation and deposition of ZnO thin films. The films are obtained by deposition of the coating solution over the chosen substrates by means of spinning, spraying or dipping techniques. Many chemicals such acetates, nitrates and chlorides were used as precursors for sol-gel derived ZnO thin films. The different precursors affect the formation of ZnO material and can provide films of different structural and morphological features. Although zinc nitrate and chloride have the advantage of high solubility in water or organic solvents, the anionic species retained in the final material are difficult to be removed giving a disadvantage for these precursors. In the other side, in addition to its practical advantages such as reduced cost and easy handling, zinc acetate dihydrate (ZAD) has the advantage of the easy removal of the acetate anions residuals during the pre-heating and annealing steps, and therefore, it is preferred and widely used as a ZnO precursor [48-51].

Chemically, sol-gel derived ZnO material is formed because of a sequence of linked reactions based basically on the precursor hydrolysis and condensation leading to

formation of the oxide network. Although, hydrated zinc acetate is easily soluble in organic solvents such ethanol or 2-methoxyethanol, amino additives, known as stabilizers, are required for obtaining clear solution. The stabilizers like monoethanolamine (MEA), diethanolamine (DEA), triethanolamine (TeA) and others can act as both a base and a complexing agent. Many roles such as reacting with precursor and facilitating the formation of complexes can be performed by these stabilizers. Moreover, the stabilizers can play the role of chelating ligands, which provide avoiding the precipitation and allow the formation of stable solutions. MEA and DEA are the most frequently used stabilizers in preparation of ZnO using sol-gel method. MEA and DEA provide preparing coating solutions of the most homogeneous, stable and transparent coating solutions. One of the advantages of MEA and DEA that they have boiling temperatures of 170 and 270 °C, respectively, which are lower than that for TeA (335 °C). The low boiling temperature of the additives (particularly MEA) provide more effective removal of the retained organic residuals during pre-heating and annealing processes of the films [18].

As MEA stabilizer (C_2H_7NO) act as a complexing agent, it makes the reactions of hydrolysis and condensation of Zinc acetate dihydrate precursor ($Zn(C_2H_3O_2)_2{\cdot}2H_2O$) relatively slow which improves the stability of ZnO solution. Zinc acetate dihydrate in solution produces mono-acetate $(C_2H_3O_2)Zn^+$ species. The reaction between $(C_2H_3O_2)Zn^+$ and C_2H_7NO would result in the formation of a chelated species with the release of acetic acid $ZnC_4H_6O_4$ [52].



A relevant role is played by the acetate community through complexing Zn^{2+} in competition with MEA. Figure 2.3 shows the relationships representations for the complex chemical of the main species. The three nucleophilic species (MEA, OH^- and CH_3COO^-) compete each other for the Zn^{2+} sites. As a result of the attack of the hydroxy group, is formed. Zinc-oxo-acetate oligomers are expected to appear at the initial stage from gradually forced hydrolysis of Zn-MEA or $Zn\text{-}OCOCH_3$ soluble

complexes. The progressive condensation of the hydrolyzed moieties gives rise to colloids [53].

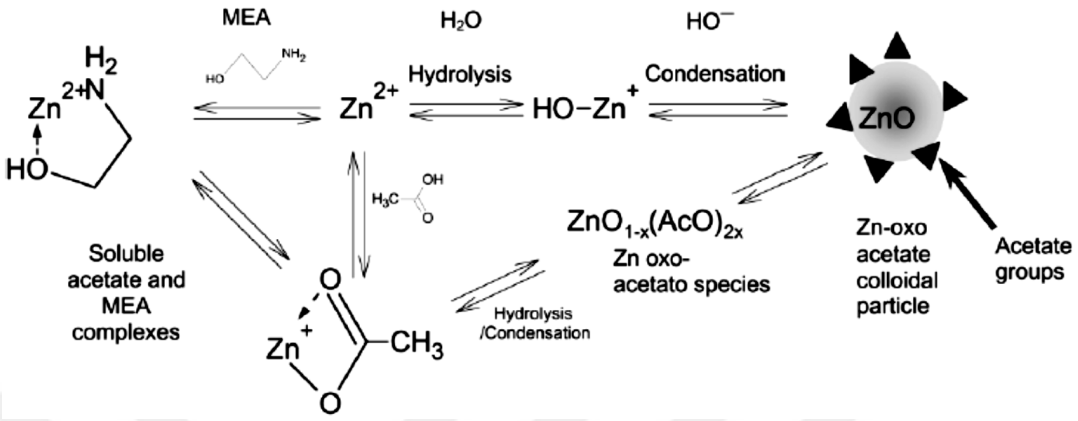


Figure 2.3: Interrelation representation for the reactions of hydrolysis and condensation involved in the sol-gel process which lead to formation of moieties Zn-oxo acetate colloidal starting from ZAD [53].

Among the techniques used for the deposition of the coating solution of ZnO on the substrate, the spin coating is preferable for many reasons including the simple setup and the ability of easily producing uniform and thin films of a few nanometer thick and up. Such films can quickly be deposited with a repeatable quality; therefore, it is widely applied for the reproducible prepartion of thin film coatings over large areas with high structural uniformity [54]. As shown if Figure 2.4, the spin coating process generally involve the application of coating solution over the entire area of the substrate while the it is rotating (dynamic dispense) or non-rotating (static dispense), then the substrate is spun according to set values of the parameters (speed and time) of the spin coater; the solution spread overall the top surface of the substrate and finally uniform thin film will be obtained.

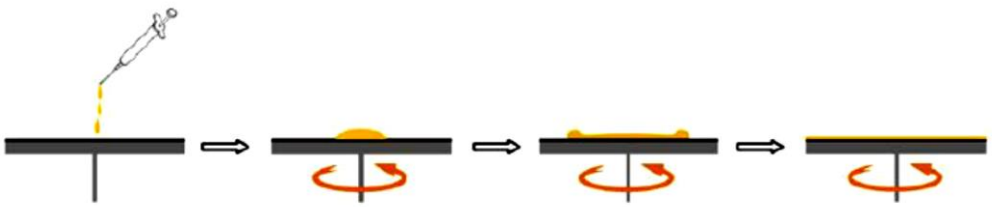


Figure 2.4: Schematic representation of typical spin-coating process

As previously explained, using static dispense mode, the process of spin coating starts with dropping the coating solution on the entire area of the substrate, then a spin process with a certain profile is applied. Figure 2.5 shows a simple spinning profile consisting of three different periods; (1) period of accelerated speed (t_1), (2) period of fixed speed (t_2-t_1) and (3) period of decelerated speed (t_3-t_2). The action of spinning at high speed cause spread out of the solution leaving a uniform and very thin layer of the dropped solution on the top surface of the substrate. During this time, the solvent evaporates leaving the desired material on the substrate. The spin speed defined by revolution per minute (rpm) and time (s) generally define the final film thickness. Relatively minor variations of ±50 rpm can cause a resulting thickness change of 10%. Since the dropped solution (resin) begins to dry during the first part of the spin cycle, it is important to accurately control the spin acceleration time. In some processes, 50% of the solvents in the resin will be lost due to the evaporation in the first few seconds of the process. The drying rate of the resin fluid during the spin process is defined by the nature of the fluid itself (volatility of the used solvent) as well as by the air surrounding the substrate during the spin process.

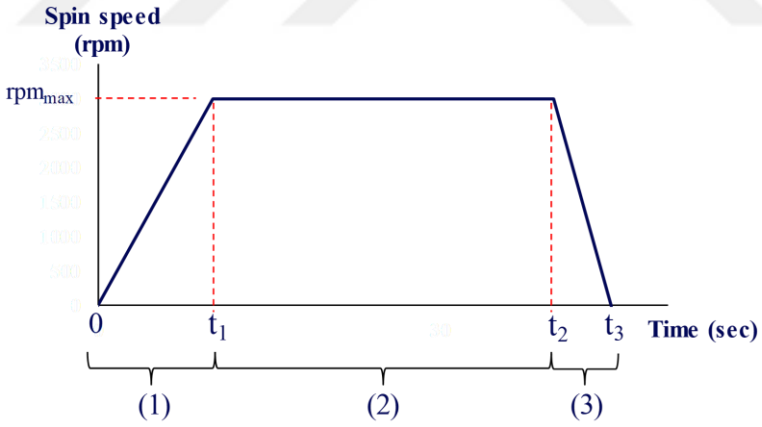


Figure 2.5: A typical profile for spinning speed

In addition to the spinning parameters, the final films thickness and other properties will depend on the nature of the coating solution. For instance, the final films get thicker with an increase in the viscosity and concentration of the solution. Furthermore, the surface tension of the solution and the wettability of the substrates play a crucial role to obtain films of the desired features and properties.

2.3 Plasmonic effect in metal nanoparticles

Metallic nanoparticles (NPs) exhibit unique optical, electronic, chemical, photoelectrochemical or magnetic properties which render them to be used for various applications [55]. Under the effect of surface plasmons (SP) resonance, metal NPs can be used as subwavelength scattering elements to couple freely propagating electromagnetic waves of light into an absorbing semiconductor thin film (Figure 2.6). Light scattering from a small metal nanoparticle embedded in a homogeneous medium is nearly symmetric in the forward and reverse directions. This situation changes when the particle is placed close to the interface between two dielectrics, in which case, light will scatter preferentially into the dielectric of the larger permittivity (larger refractive index).

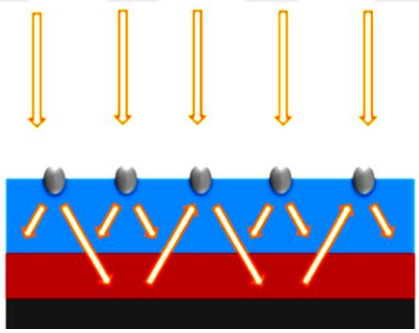


Figure 2.6: Light trapping by forward scattering from metal nanoparticles at the surface of the absorbing semiconductor thin film.

SP resonance is a collective oscillation of conduction electrons excited by the electromagnetic field of light. It corresponds to an interaction between matter and the electromagnetic field of the light. When the particle is illuminated, the electromagnetic field of the light exerts a force on these conduction electrons moving them toward the NP surface. As these electrons are confined inside the NP, negative charge will be accumulated in one side and positive charge in the opposite one, creating an electric dipole. This dipole generates an electric field inside the NP opposite to that of the incident light that will force the electrons to return to the equilibrium position (Figure 2.7). The larger the electron displacement, the larger the electric dipole and consequently the restoring force. The situation is similar to a linear oscillator with a restoring force proportional to the displacement from the equilibrium position. If the electrons are displaced from the equilibrium position and the field is later removed,

they will oscillate with a certain frequency that is called the resonant frequency; in the case of SP, it is named the plasmonic frequency [56].

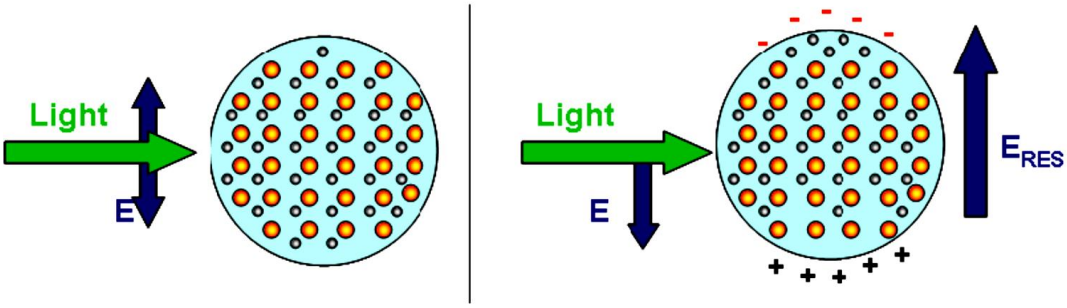


Figure 2.7: The light interaction with a metallic NP. The electric field of the light induces the movement of conduction electrons which accumulate at the NP surface creating an electric dipole. This charge accumulation creates an electric field opposite to that of the light [56].

When an alternating force is applied to a linear oscillator, the system oscillates with the same frequency of the external force, but the amplitude and phase will depend on both the force and the intrinsic parameters of the oscillator. In particular, the oscillating amplitude will be maxima for the resonant frequency (Figure 2.8a). It is quite straightforward to understand that if the frequency of the external force is the same that the plasmonic frequency of the NP, it will be easy to make the electrons oscillate, but as we move far away from this frequency the movement of electrons will be more difficult, i.e., with reduced amplitude. The resonant frequency for these oscillations in metallic NPs corresponds typically to UV-Vis light and consequently, the SP arise absorption bands in this region of the spectrum as Figure 2.8b illustrates [56].

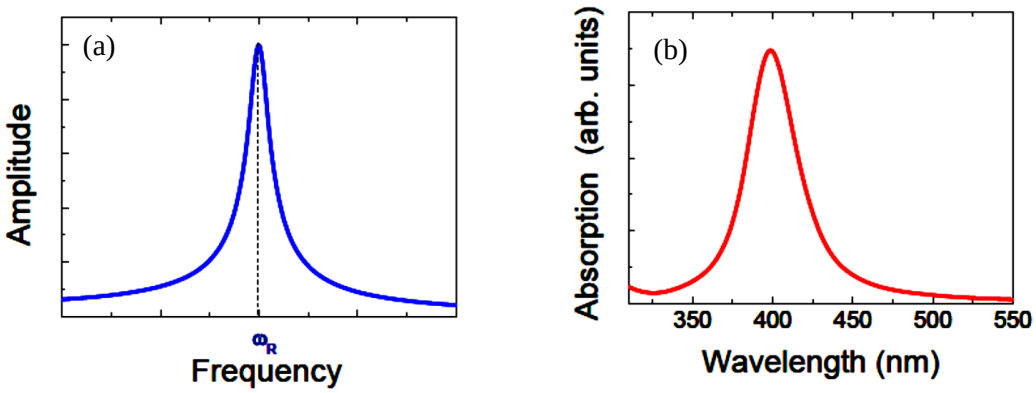


Figure 2.8: Oscillation amplitude for a linear oscillator as a function of the external force frequency (a), and optical absorption spectrum corresponding to 30 nm Ag NPs embedded in a silica glass (b).

Noble metal nanoparticles like silver (Ag) and gold (Au) can support localized surface plasmons, where light can be resonantly absorbed or scattered depending on the metal nanoparticles' size, shape, spacing, and the surrounding environment. Ag and Au metals have their own advantages and disadvantages, e.g., Au nanoparticles do not oxidize easily under ambient conditions, while Ag nanoparticles have higher scattering efficiency than Au [57]. Small Ag and Au nanoparticles of roughly 30 nm have absorbance peaks near to 400 and 525 nm, respectively. As particle size increases, the peaks broaden and shift toward longer wavelengths (Figure 2.9). Larger nanoparticles have also increased capability of light scattering [58].

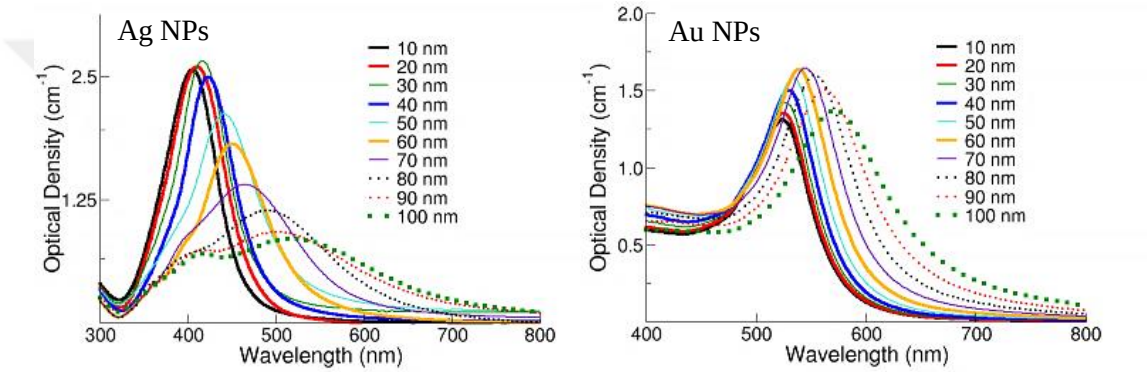


Figure 2.9: Optical absorption spectra for Ag and Au NPs of different sizes.

Integration of plasmonic resonance schemes with conventional photodetectors and photovoltaic cells has been extensively studied and an improvement in the efficiency for such devices by making use of the optical trapping properties of surface plasmons were clearly demonstrated [59, 60]. For incorporating metal nanoparticles into device, different methods have been established including island forming by thermal annealing of a deposited metal thin film and spin coating of chemically synthesized metal nanoparticles (nanoparticles-contained solutions) [33].

2.4 n-ZnO/p-Si heterojunction-based diode

Dissimilar to the p-n homojunction which is formed using the same semiconductor material, the p-n heterojunction is generally formed by growing one semiconductor onto a different semiconductor. ZnO-based p-n heterojunctions can be formed by the deposition of n-ZnO film onto p-Si (Figure 2.10a). ZnO film can be used as the n-type

layer of the heterojunction device since it is easy to have high n-type conductivity especially when it doped with Al or Ga. Recently, n-ZnO/p-Si heterojunction-based UV photodiodes and solar cells have attracted a significant interest because of various advantages such as ZnO's direct and wide bandgap, a simple and low-cost processing and capability of working in severe environments [21, 61]. For these devices, the incident light is absorbed and converted to photogenerated carriers. The high energy photons can be absorbed in the ZnO layer, while the low energy photons transmitted through the ZnO layer can be absorbed in the depletion region of p-Si [21, 23]. In addition to the good electrical and optical properties of ZnO film, for the device, it can provide a strong UV response and it can act as an electrically active n-layer as well as antireflection (AR) coating because of the close match of its refractive index with the required value for Si surface [61].

Each semiconductor in the ZnO/Si heterojunctions is characterized by its own lattice structure with different lattice constants, band gaps, work functions, and electron affinities. When they joined, there will be a misalignment in the conduction and valence bands causing discontinuities in the energy bands as the Fermi levels line up at equilibrium (Figure 2.10b). The conduction band offset, ΔE_c and the valence band offset, ΔE_v accommodate the difference in the band gap, ΔE_g between the two semiconductors. In the ideal case, ΔE_c would be the difference in electron affinities $q(\chi_{ZnO} - \chi_{Si})$, and ΔE_v would be found from ΔE_c + ΔE_g. This is known as the Anderson affinity rule [62]. The barriers potential, ϕ_{bn} and ϕ_{bp} for electrons and holes are different from each other and from the built-in contact barrier potential, ϕ_{bi}.

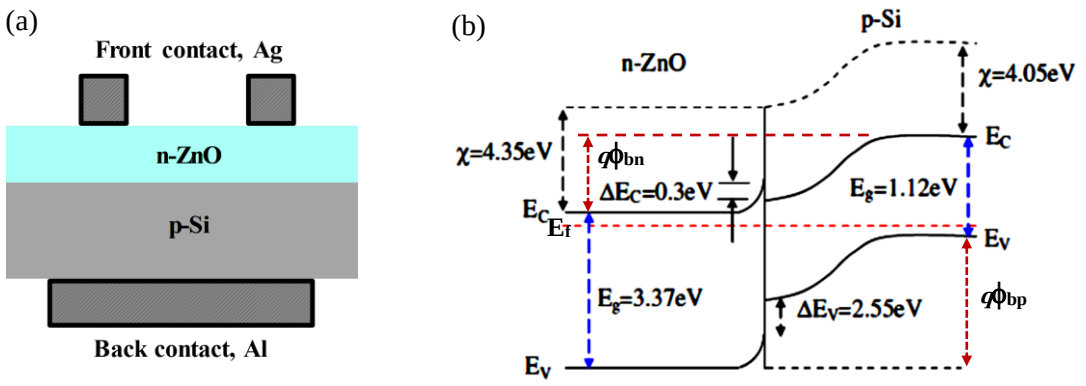


Figure 2.10: Schematic diagram n-ZnO/p-Si heterojunction-based photoelectric device (a), and energy band diagram of n-ZnO/p-Si junction at equilibrium (b).

Generally, there can be two different mechanisms for current flow across p-n heterojunction determined by the discontinuities in the energy bands; diffusion current same as p-n homojunction and thermionic emission same as Schottky contact [63]. The interplay between the potential barrier and the band offset ultimately determines the current flow mechanism in p-n heterojunction depending on the band alignment.

When the maximum energy point (band spike) for the conduction band of ZnO is lower than E_c of p-Si, ϕ_{bn} and ϕ_{bp} are determined as $\phi_{bn} = E_{c,\mathrm{ZnO}} - E_{c,\mathrm{Si}}$ and $\phi_{bp} = \phi_{bn} + \Delta E_g$. In this case, the current flow across the heterojunction is governed by diffusion current mechanism similar to that of p-n homojunction. The other case when the conduction band spike of ZnO is higher than E_c of p-Si, the electron transport is limited by the spike in the conduction band produced by ΔE_c. In this case, the thermionic mechanism similar to that of Schottky contact is assumed. The conditions at which the spike becomes limiting depend generally on the doping in the *n* and *p-type* regions and the bias voltage across the junction. Spike becomes more limiting when the p-region is heavily doped. Even if the spike does not limit the current flow at low forward bias, it can become limiting as the bias increases expecting diffusion current at lower forward voltages and thermionic-emission-limited current at higher voltages [63].

Although the actual derivation of the current density-voltage (*J–V*) relationship of the p-n heterojunction is generally complex, the general form of the *J–V* equation can be considered similar to that of a Schottky barrier diode and is generally dominated by one type of carrier [64]. Accordingly, the *J-V* relationship of n-ZnO/p-Si heterojunction in the dark can be formulated as follows [64]:

$$J_d = J_o \left[\exp\left(\frac{eV}{nkT}\right) - 1\right] \qquad (\mathbf{2.1})$$

$$J_o = A^* T^2 \exp\left(\frac{-e\phi_{bo}}{kT}\right) \qquad (\mathbf{2.2})$$

where J_d is the dark current density, J_o is the reverse saturation current density, V is the applied voltage, n is the ideality factor, k is Boltzmann's constant, A^* is the theoretical Richardson constant (= 32 A/cm^{2}k^2 for ZnO), T is junction temperature in Kelvin and ϕ_{bo} is the zero bias barrier potential.

Equation (2.1) is of the same form as that of the p-n homojunction diode. The differences are in the magnitudes of J_o and the switching characteristics. For ideal p-n homojunction diode, J_o is given by Equation 2.3 [40]:

$$J_o = \frac{eD_n n_{po}}{L_n} + \frac{eD_p p_{no}}{L_p} \qquad (\mathbf{2.3})$$

where D_n and D_p are minority carrier electron and minority carrier hole diffusion coefficient (cm^2/s), n_{po} and p_{no} are thermal-equilibrium minority carrier electron and minority carrier hole concentration (cm^{-3}) and L_n and L_p are minority carrier electron and hole diffusion length (cm).

The current transport mechanism for the two junctions is different. The current in the p-n homojunction diode is determined by the diffusion of minority carriers while the current in the Schottky barrier diode is determined by thermionic emission of majority carriers over a potential barrier.

2.4.1 ZnO-based solar cells

The n-ZnO/p-Si heterojunction-based solar cell is designed by making the top layer, ZnO, thin and highly doped whereas the lower bulk Si is thick and less doped. The incident light is absorbed and converted to photogenerated carriers. The high energy photons can be absorbed in the ZnO layer, while the low energy photons transmitted through the ZnO layer can be absorbed in the depletion region of p-Si [21, 23]. This is convenient since most of the depletion region, hence the built-in electric field, is in fact contained at the interface, but within the Si side. This is in fact the reason why the highly conductive ZnO is deposited onto Si when fabricating a solar cell. Si has a high absorption coefficient, $\alpha(\lambda)$ while ZnO has a low one in the visible region. In the spectral range between 300 to 1150 nm, $\alpha(\lambda)$ varies from $2xl0^6$ to 1 cm^{-1} for crystalline Si and varies from 1 to 4 cm^{-1} for ZnO [65]. $\alpha(\lambda)$ is therefore a parameter which describes to what extent incident light can be converted into electricity. Since the goal is to minimize the photon absorption in the ZnO layer and to maximize it in the Si, it is best to achieve a thin deposition of ZnO (~0.1 μm). $\alpha(\lambda)$ is the sum of the fundamental absorption coefficient and the free carrier absorption coefficient. The fundamental absorption occurs when one electron-hole (E-H) pair generated by a

photon with energy slightly higher or equal to the energy band gap of the semiconductor. The free carrier absorption occurs when a photon with much larger energy generates one electron-hole pair and the excess energy will be dispersed (lost) as thermal energy.

The generation rate, G of electron-hole (E-H) pairs in a semiconductor is defined as G = g(x)/A, where A is the illuminated area and g(x) is the generation function at a depth x described by Equation 2.4 [66].

$$g(x) = \alpha(\lambda)\exp[-\alpha(\lambda).x] \qquad (\mathbf{2.4})$$

E-H pairs generated at a rate G have a finite lifetime. For carrying off the generated carriers into the external circuit, an electric field must be present to separate the free carriers and draw them out through the front and back contacts of the solar cell. The required electric field is provided by the built-in potential in the p-n junction of the solar cell. In fact, the presence of the built-in potential makes the conversion of sunlight into an electrical current is possible with a structure like the p-n junction. The electric field will attract the newly generated electrons from the p-type region (Si) towards the n-type region (ZnO) and out the front contact and the newly generated holes from the n-type into the p-type and out the back contact creating an external current flow. High doping in the thin layer of ZnO is required to achieve a high conductivity for separated carriers to be drawn out through the front contact.

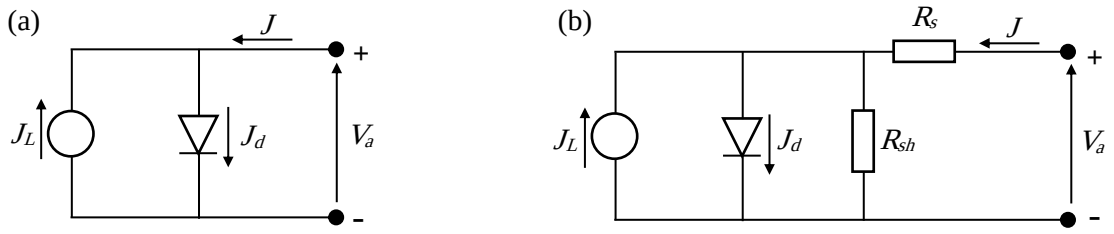


Figure 2.11: The equivalent circuit of an ideal solar cell (a), and a solar cell with a series resistance, R_s and a shunt resistance, R_{sh} (b).

The ideal solar cell is represented by a simple equivalent circuit in which a diode and current source are connected in parallel (Figure 2.11a). The *J-V* characteristic of an illuminated cell is given by Equation 2.5 [66], where J_L is the light (photogenerated) current.

$$J = J_d - J_L = J_o \left[\exp\left(\frac{eV}{kT}\right) - 1\right] - J_L \qquad (\mathbf{2.5})$$

Under uniform generation rate, G, J_L is given by Equation 2.3-7:

$$J_L = e\mathrm{G}(L_n + W + L_p) \qquad (\mathbf{2.6})$$

where L_n and L_p is the minority-carrier-diffusion length for electrons and holes, respectively, and W is the width of the depletion region. It means that only carriers generated in the depletion region and in the regions up to the minority-carrier-diffusion length from the depletion region contribute to the light current.

The current density at zero applied voltage (V = 0) is defined as short circuit current density, J_{sc} which is equal to I_L in the ideal case. The voltage at which no current flows through the external circuit (J = 0) is defined as open circuit voltage, V_{oc}. The ratio between the maximum power ($P_{max} = J_{mp}.V_{mp}$) generated by a solar cell and the product of V_{oc} with J_{sc} is defined as fill factor, FF. The J_{sc}, V_{oc} and FF are measures of the solar cell's performance. V_{oc} depends on J_L and it can be calculated from Equation 2.5 assuming that J = 0 and $J_L = J_{sc}$.

$$V_{oc} = \frac{kT}{e}\ln\left(\frac{J_{sc}}{J_o} + 1\right) \qquad (\mathbf{2.7})$$

FF as a function of V_{oc} is expressed as [66];

$$FF = \frac{J_{mp}V_{mp}}{J_{sc}V_{oc}} = \frac{V_{oc} - \ln(V_{oc} + 0.72)}{V_{oc} + 1} \qquad (\mathbf{2.8})$$

Efficiency, η is another measure of performance and is calculated by dividing the maximum power, P_{max} generated by the solar cell over the incident power density, P_{in} of the source of light. The irradiance value P_{in} of 1000 W/m^2 for the AM1.5 spectrum has become a standard for measuring the conversion efficiency of solar cells,

$$\eta = \frac{P_{max}}{P_{in}} = \frac{J_{mp}V_{mp}}{P_{in}} = \frac{J_{sc}V_{oc}FF}{P_{in}} \qquad (\mathbf{2.9})$$

In practice, the performance parameters (J_{sc}, V_{oc}, FF and η) are influenced by a series resistance, R_s, and a shunt resistance, R_{sh}. The influence of these parameters on the J-

V characteristic of the solar cell can be studied using the equivalent circuit shown in Figure 2.11b. Where *A* is the area of the solar cell, the *J*-*V* relation is given by [66];

$$J = J_o \left\{ \exp\left[\frac{e(V - AJR_s)}{nkT}\right] - 1 \right\} + \frac{V - AJR_s}{R_{sh}} - I_L \qquad (\mathbf{2.10})$$

In order to improve the solar cell's efficiency, the series resistance should be as low as possible ($R_s = 0$ for the ideal case) and the shunt resistance should be as high as possible ($R_{sh} \rightarrow \infty$ for the ideal case). Generally, the low shunt resistance decreases the open circuit voltage, whereas the high series resistance decreases the short circuit current. Furthermore, the values of these resistances may be easily observed from the *I*-*V* characteristics. Specifically, the series resistance is the inverse of the slope of the *I*-*V* curve in the 1st quadrant, whereas the shunt resistance is that in the 3rd quadrant.

2.4.2 ZnO-based photodiodes

A photodiode is a p-n junction diode operated under reverse bias condition. Similar to the solar cell, photodiode depends on the excess in the minority carriers in its operation. A very small current (limited to the reverse saturation current) can flow through the device in the dark, while a high current can flow under illumination due to the high excess in the minority carriers generated by photons. The ideal photodiode is represented by a switch contacting under illumination and non-contacting in the dark. Practical photodiodes can detect light of very low intensity and they can be calibrated for highly accurate measurements within the range from 10^{-9} to above 100 mW/cm^2 of light intensity [67]. In contrast to conventional Si-based photodiode, the ZnO film improves the photodiode's responsivity in the UV/blue region. Therefore, ZnO-based photodiodes have useful for UV illumination applications and defined as UV photodiodes.

Photodiodes can be represented by an equivalent circuit similar to that of the solar cell. As shown in Figure 2.12a, in addition to the current source representing the light current density, J_L, conventional diode representing the dark current density, J_d, series resistance, R_s and shunt resistances, R_{sh}, a junction capacitance (C_j) is included in the circuit. The reverse bias characteristic current density-voltage (*J*-*V*) curves of photodiode in the dark and under light of various intensities are shown in Figure 2.12b.

It can be noticed from the figure that the ratio of I_d to J_L is reverse voltage dependent. For this reason, the sensitivity of photodiode to light is usually determined at a specific value of reverse voltage.

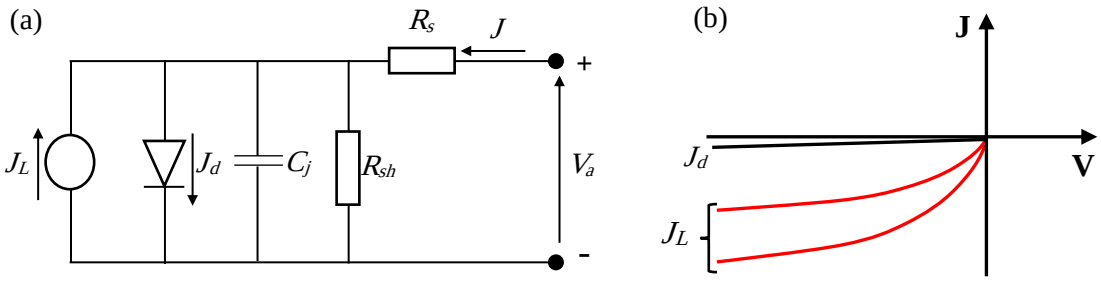


Figure 2.12: The equivalent circuit of a photodiode (a) and the reverse bias characteristic *J-V* curves of photodiode under dark and light conditions (b).

The performance of photodiodes is generally judged according to their sensitivity to light and their rise/fall time and frequency response. Photosensitivity and photoresponsivity are measures of the sensitivity of photodiodes to light.

- Photosensitivity, *PS* is simply defined as the ratio of light current density, J_L to dark current density, J_d at a specific value of reverse applied voltage, where:

$$PS = \frac{J_L}{J_d} \qquad (\mathbf{2.11})$$

- Photoresponsivity, $PR(\lambda)$ is defined as the ratio of light current density, J_L to the input light power density, P_{in} at a given wavelength [67]:

$$PR(\lambda) = \frac{J_L}{P_{in}}\ (A/W) \qquad (\mathbf{2.12})$$

- The rise time and fall time of a photodiode is defined as the time for the signal to rise or fall from 10 % to 90 % or 90 % to 10 % of the final value, respectively. This parameter can be also expressed as frequency response, t_r which is the frequency at which the photodiode output decreases by 3db. It is approximated by [67]:

$$t_r \cong \frac{0.35}{f_{3\text{db}}}\ (s) \qquad (\mathbf{2.13})$$

CHAPTER 3

EXPERIMENTAL WORK

3.1 Deposition and characterization of ZnO:X films and metal NPs

3.1.1 Deposition process

3.1.1.1 Deposition of ZnO:X films

Sol-Gel method was used for the deposition of undoped and doped ZnO films on glass substrates. The flow chart and the inputs/output parameters of the processes of sol-gel method are shown in Figure 3.1. Many parameters of these processes were investigated and optimized according to the available materials and equipment. The whole sol-gel process was first optimized by working on the deposition of Al-doped ZnO (AZO) thin films. Throughout this work, many processes of sol-gel method were optimized including chemical synthesis, solution aging, spin coating, and annealing processes. The investigated parameters of these processes are shown in Table 3.1.

Table 3.1: The investigated parameters of Sol-Gel process

Process	Step	Investigated parameters
Preparation of coating solution	Chemical synthesis	▪ Doping precursor ▪ Doping ratio ▪ Solution molarity ▪ Solvent-stabilizer combination ▪ Mixing sequence of chemicals
	Solution aging	▪ Time
Process of film coating	Spin coating	▪ Spin speed ▪ Spin acceleration time ▪ Coating cycles
	Pre-heating	▪ Temperature ▪ Time
	Annealing	▪ Temperature ▪ Time

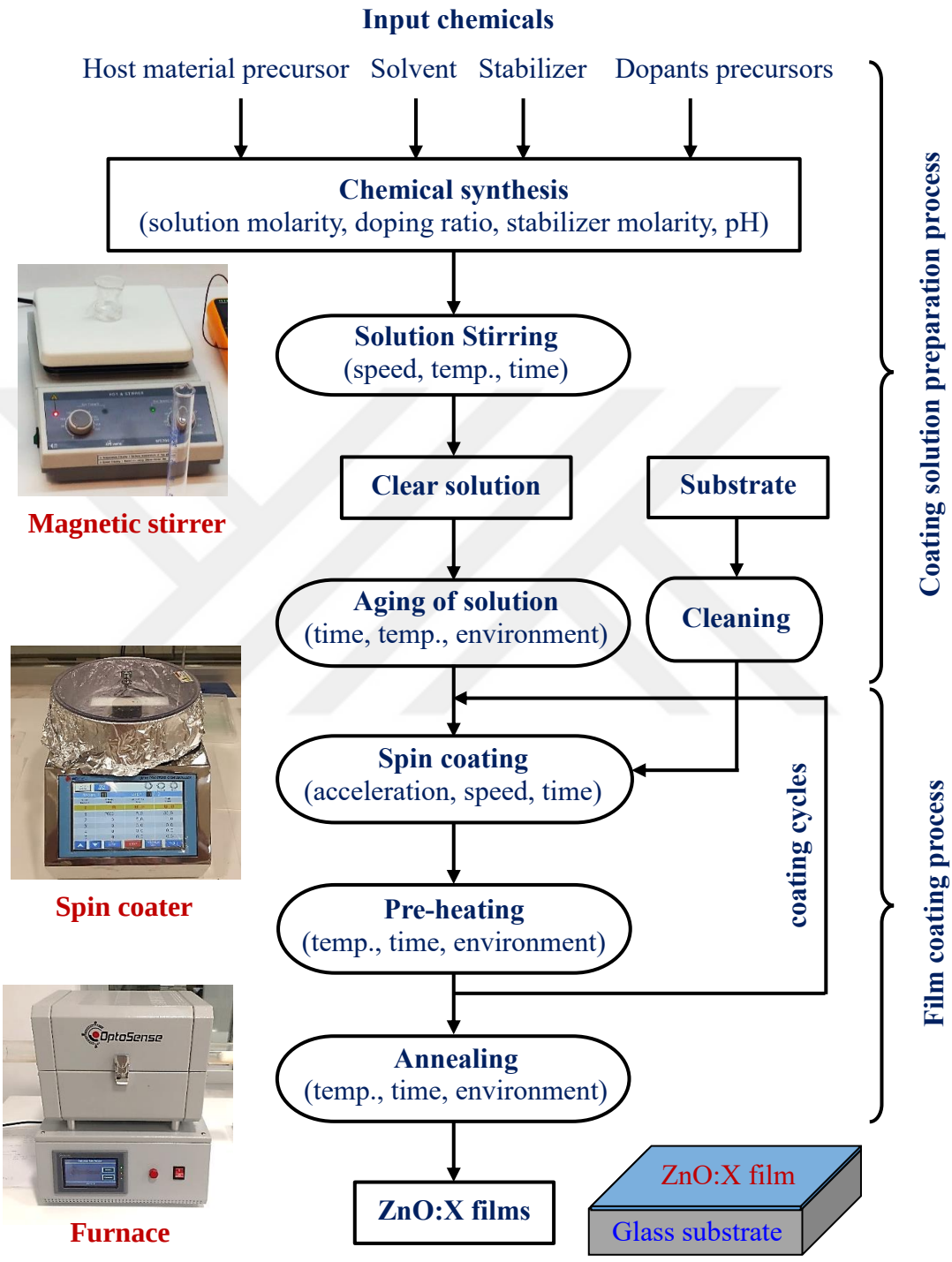


Figure 3.1: Flow chart of Sol-Gel method for fabrication of ZnO:X thin films

The obtained results of the optimized parameters were then applied for the deposition of the thin films of Gallium-doped ZnO (GZO), Boron-doped ZnO (BZO), and Gallium and Boron co-doped ZnO (GBZO). As an original work, an extra experiment was carried out for investigating the influence of the spin acceleration time on the properties of GZO films for the first time in the literature. The results of this experiment were published in the Journal of Sol-Gel Science and Technology [68].

Amongst the performed experiments, hereafter the main experiments were carried out for the investigation of sol-gel process parameters for the deposition of ZnO:X thin films:

- Preliminary experiment for deposition of Al-doped ZnO (AZO) thin films of various values of Al doping ratio.

Doping ratio (at. %)			
0	1	2	3

- Deposition of AZO (3 at. %) thin films with altering the spin coating parameters vs solution molarity.

Spin acceleration time (sec)	**Solution molarity**		
	0.2M	0.4M	0.6M
5			
10			
20			
40			

- Deposition of AZO (3 at. %) thin films using different combinations of solvents and stabilizers for the synthesis of coating solutions.

Stabilizer	**Solvent**	
	Ethanol	2-methoxyethonal
Monoethanolamine (MEA)		
Diethanolamine (DEA)		
Triethylamine (TEA)		

- Deposition of AZO (3 at. %) thin films with altering the solution molarity vs solvent-stabilizer combinations.

Solvent-stabilizer combination	**Solution molarity**	
	0.2M	0.5M
Ethanol-MEA		
2-methoxyethonal-MEA		

- Deposition of AZO films with extended range of Al doping ratio values using the optimized parameters of deposition process.

Doping ratio (at. %)				
1	2	3	4	5

- Deposition of Gallium single-doped ZnO (GZO) thin films under various values of doping ratio.

Doping ratio (at. %)				
1	2	3	4	5

- Deposition of GZO (2 at. %) thin films using different values of spin acceleration time parameter in purpose of investigating influence of this parameter on the properties of GZO films.

Spin acceleration time (sec)					
0	2	4	6	8	10

- Deposition of Boron single-doped ZnO (BZO) thin films under various values of doping ratio.

Doping ratio (at. %)				
1	2	3	4	5

- Deposition of Gallium and Boron co-doped ZnO (GBZO) thin films by applying the formula ZnO:Ga_{3-x}-B_x. The doping parameter, x was varied from 0 to 1 with a step of 0.25 while keeping the total doping ratio fixed at 3 at. %.

Doping parameters (x)				
0	0.25	0.5	0.75	1

The steps of deposition process can be described as follows:

1- Chemical synthesis of coating solution

The zinc precursor (zinc acetate dihydrate, ZAD) and dopant precursors, DPs are dissolved separately in an organic solvent (ethanol, methanol, 2-methoxyethanol) and stirred simultaneously for 15 min, then both solutions are mixed and stirred for 15 min. Simultaneously, a stabilizer (Monoethanolamine, MEA, Diethanolamine, DEA, Triethylamine, TEA) is dissolved separately using the same solvent and stirred for 15 min and then added to mixed solution. The mixture is stirred for 2 h to get a clear, transparent, and homogeneous solution (Figure 3.2). The mixed chemicals are stirred using a magnetic stirrer with speed of 600 rpm at 60 °C. The concentration of ZAD in the solvent (solution molarity, SM) is adjusted to the desired value (0.2 - 0.6 mol/l), and the doping ratio, DR is calculated as ([dopant]/[dopant + Zn]) to be at the desired value (0 - 5 at. %). The ratio of stabilizer to (ZAD + dopant precursor, DP) is maintained at 1:1 molar ratio. The resultant solution is then aged in a closed chamber at room temperature for a certain period (24 - 48 h) before it is used as a coating solution. A list of the used chemicals is shown in Table 3.2.

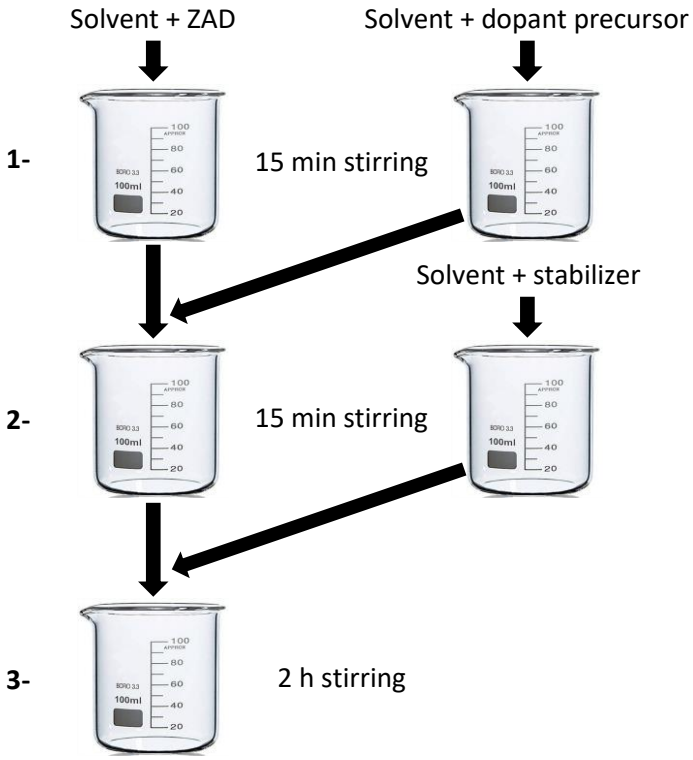


Figure 3.2: chemical synthesis steps

The solution molarity, molar ratio of stabilizer, doping ratio and pH value are the main parameters of the prepared coating solution that affect the properties and quality of the deposited films and the mass values of the mixed chemicals should be calculated precisely based on the required values of these parameters. The mass values of the used chemicals are calculated as follows:

- Mass calculation of Zn precursor (ZAD) to get the desired solution molarity (SM):

$$\text{ZAD mass (g)} = \text{ZAD molar mass (g / mol)} * \text{mol of ZAD (mol)} \quad (\mathbf{3.1})$$

$$\text{Mol of ZAD (mol)} = \text{SM (mol/l)} * \text{solvent volume} \quad (\mathbf{3.2})$$

- Mass calculation of dopant precursor (DP) to get the desired doping ratio (DR):

$$\text{DP mass (g)} = \frac{\text{DP molar mass (g/mol)} * \text{No. of dopant atoms}}{N_A * \text{No. of dopant atoms per molcule of its precursor}} \quad (\mathbf{3.3})$$

where N_A is Avogadro's number ($N_A = 6.022140857x10^{+23}$) and:

$$\text{No. of dopant atoms} = \frac{\text{DR (at.\%)} * \text{No. of Zn atoms}}{100 - \text{DR (at.\%)}} \quad (\mathbf{3.4})$$

$$\text{No. of Zn atoms} = N_A * \text{mol of ZAD} \quad (\mathbf{3.5})$$

In case of co-doping (x = 1 and 2), the equation 3.4 is slightly modified as follows:

$$\text{No. of atoms of dopant\#x} = \frac{\text{DR of dopant\#x (at.\%)} * \text{No. of Zn atoms}}{100 - \text{total DR (at.\%)}} \quad (\mathbf{3.6})$$

- Mass calculation of stabilizer to get 1:1 molar ratio to (ZAD + DP):

$$\text{Stabilizer mass (g)} = \text{stabilizer molar mass (g/mol)} * \text{mol of (ZAD + DP)} \quad (\mathbf{3.7})$$

the total mol of all dopants precursors is considered, where:

$$\text{Mol of DP} = \frac{\text{DP mass (g)}}{\text{DP molar mass (g/mol)}} \quad (\mathbf{3.8})$$

Table 3.2: List of chemicals used for preparation of coating solutions.

Chemical material	Type	Formula	Molar mass (g/mol)	Brand
Ethanol	Solvent	C_2H_6O	46.07	EMSURE
Methanol	Solvent	CH_4O	32.04	EMSURE
2-Methoxyethanol	Solvent	$C_3H_8O_2$	76.09	SIGMA-ALDRICH
Monoethanolamine (MEA)	Stabilizer	C_2H_7NO	61.08	EMSURE
Diethanolamine (DEA)	Stabilizer	$C_4H_{11}NO_2$	105.14	MERCK
Triethylamine (TEA)	Stabilizer	$C_6H_{15}N$	101.19	SIGMA-ALDRICH
Zinc acetate dihydrate (ZAD)	Zn precursor	$ZnC_4H_6O_4$	219.50	EMSURE
Aluminum Chloride	Aluminum precursor	$AlCl_3$ (anhydrous)	133.34	EMSURE
Aluminum Nitrate nonahydrate	Aluminum precursor	$Al(NO_3)_3.9H_2O$	375.13	SIGMA-ALDRICH
Gallium (III) nitrate hydrate	Gallium precursor	$Ga(NO_3)_3 \cdot xH_2O$	255.74	SIGMA-ALDRICH
Trimethyl borate	Boron precursor	$C_3H_9BO_3$	103.91	ALDRICH

2- Coating of films

The thin film of ZnO:X material is spin-coated on a pre-cleaned square glass substrate (1.5x1.5 cm^2). The static dispense method is used to apply the coating solution onto the entire area of the substrate surface, then the substrate is accelerated (0-10 sec) to the final spin speed (1000-3000 rpm) for approximately 30 s. After the spin coating, the film is preheated at 300-500° C for 5-10 min, to evaporate the solvent and to remove organics. The spin coating-preheating cycles are repeated many times to get the required thickness, and then, the film is annealed at 500 °C for an hour in an open-air microprocessor-controlled furnace to decompose the residual organics as well as to form the polycrystalline oxide films. Prior to the coating process, the glass substrates are undergone a cleaning procedure. They are first washed with a detergent using a soft sponge and rinsed with deionized (DI) water, then sequentially they are ultrasonically cleaned with acetone, ethanol and DI water, respectively by placing them into the solutions beakers and holing for 5 min at 50 ^oC. Finally, they are

thermally dried at 120 ºC for 10 min. A typical developed recipe for the depositions of GZO thin film is given in Table 3.3.

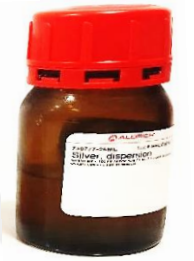
Table 3.3: Typical recipe for deposition of 3 at. % Ga-doped ZnO (GZO) thin film.

Process	Step	Description			
Preparation of coating solution	Chemical synthesis	**Chemicals synthesis parameters**			
		Solution molarity (ZAD/Solvent)	Stabilizer molarity (MEA/(ZAD + DP))	Doping ratio (DR)	pH
		0.2 mol/l	1:1 molar ratio	3 atomic %	6
		Chemicals and quantities			
		Zinc precursor (ZAD)	Ga dopant precursor	Stabilizer	Solvent
		Zinc acetate dihydrate	Gallium (III) nitrate hydrate	MEA	Ethanol
		1.317 g	0.047 g	0.378 g	30 ml
	Stirring process	**Magnetic stirrer parameters**			
		Speed	Temp.	Time	Environment
		600 rpm	60 ºC	2 h	Ambient air
	Aging process	**Aging process parameters**			
		Time	Temp.	Environment	
		48 h	RT	Ambient air	
Film coating	Coating process	**Spin coating parameters**			
		Speed	Acc. time	Time	Temp.
		2000 rpm	2 sec	30 sec	RT
		Pre-heating parameters			
		Temp.	Time (min)	Environment	
		500 ºC	5 min	Ambient air	
		Coating cycles: 10			
		Substrate: square glass wafers			
	Annealing process parameters				
	Temp. (^{o}C)	Time	Environment		
	500 ºC	60 min	Ambient air		

3.1.1.2 Deposition of metal NPs (Au and Ag)

Spin coating technique was used to deposit the solution processed metal nanoparticles (NPs) on GZO-coated Si substrates. Dispersions of spherical-shape metal NPs of different materials were used including colloidal gold (Au) NPs, stabilized suspension in 0.1 mM Phosphate Buffered Saline (PBS), reactant free (SIGMA-ALDRICH, product numbers 753688) and silver (Ag) NPs of 100 nm diameter, dispersed in aqueous buffer with 0.02 mg/ml mass concentration, contains sodium citrate as stabilizer (SIGMA-ALDRICH, product number 730777). The specifications of these metal NPs dispersions are shown in Table 3.4.

Table 3.4: Specifications of the used dispersions of Au and Ag NPs.

Parameter		**Metal NPs dispersion** (25 ml)	
Physical appearance			
NPs material		Au NPs	Ag NPs
Particle size (nm)		100	100
Concentration (particle/ml)		3.84 x10^9	3.6 x10^9
Absorption peak	Wavelength (nm)	562	480
	FWHM (nm)	90	198

The spin coating process was optimized to obtain uniform distribution as well as optimum density of particles on the surface. The deposition of NPs is performed by dropping the NPs solution on the substrate and held for 10 min, then the substrate is spun out by the spin coater. The spin coating recipe is 2000 rpm speed, 2 sec acceleration time and 60 s spinning time. Finally, the substrate is rinsed with deionized water (DI) and then treated thermally at 350 ^oC for 10 min in atmospheric air for drying and removal of chemical residuals.

3.1.2 Properties characterization measurements

The properties and quality of the deposited films and metal NPs were evaluated by investigating their structural, optical and electrical properties. The structural properties were investigated using X-ray diffractometer (XRD), scanning electron microscopy (SEM), and atomic force microscope (AFM). The optical properties were investigated using ultraviolet-visible (UV-vis) spectrophotometer. The electrical properties were investigated using the four-point probe and Hall effect measurement systems. Table 3.5 shows the measurable and derivable parameters of the used measurement systems. A brief description for each system along with the calculations of derivable parameters is given in this section.

Table 3.5: Systems of characterization measurements

Measurement system	Type of characterization	Measurable parameters	Derivable parameters
XRD	Crystal structure properties	▪ Diffraction peaks	▪ Material dentification ▪ Crystallinity ▪ Texture coefficient ▪ Crystal size ▪ Lattice constant ▪ Crystal strain
SEM	Microstructure properties	▪ Nanoscale view imaging	▪ Grain size ▪ Material density
AFM	Surface morphology	▪ Nanoscale topographic imaging	▪ Surface roughness ▪ Surface voids ▪ Particle (grain) size
UV-vis spectrometer	Optical properties	▪ Transmittance ▪ Absorbance ▪ Reflectance	▪ Film thickness ▪ Band gap energy ▪ Refractive indices ▪ Material density
Four-point probe	Electrical properties	▪ Sheet resistance	▪ Film resistivity
Hall effect	Electrical properties	▪ Carrier type ▪ Carrier density ▪ Carrier mobility	▪ Resistivity ▪ R-T profile

1- X-ray diffractometer (XRD)

XRD is a non-destructive technique used for determining the properties of the crystal structure of material. The X-rays are incident on the sample at an angle α. The primary beam is absorbed by or transmitted through the sample; only the diffracted beam is recorded on the film (Figure 3.3). The diffracted beam emerges at twice the Bragg angle θ_B [69].

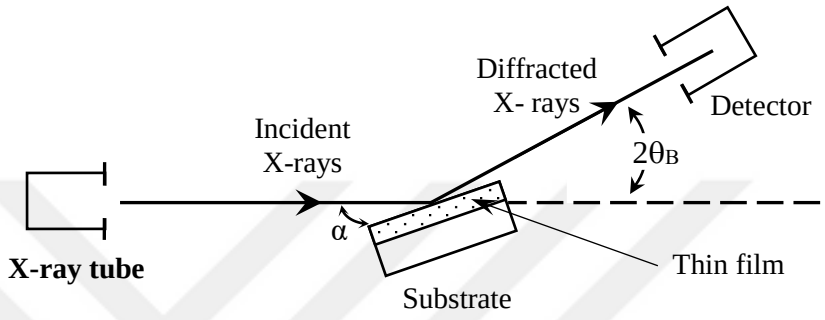


Figure 3.3: XRD measurement schematic

The crystal structure of the deposited films was investigated by Rigaku Miniflex 600 Table-Top Powder X-ray diffractometer, XRD (Figure 3.4a) using Cu anode material operating at 40kV and 15mA with Cu Kα radiation having wavelength 1.54059 Å. In the thesis work, the diffraction patterns were collected over the $2\theta_B$ range 25-70° with a step size of 0.02°.

A sample of measured XRD patterns for one of the deposited ZnO thin films is shown in Figure. 3.4b. The detected diffraction peaks reveal the that the material has a crystalline structure and their crystals are oriented in planes corresponding to the diffraction peaks. The peak of the highest intensity represents generally the preferred plane of crystals orientation. Each material has a standard XRD diffraction pattern (Joint Committee on Powder Diffraction Standards, JCPDS card), and the unknown material can be identified when its measured XRD pattern matches one of the JCPDS cards. For instance, the measured XRD patterns of the deposited ZnO thin film well matches the JCPDS 00-036-1451 card which belongs to the ZnO material of a hexagonal wurtzite structure. If no diffraction peaks are detected, then the material has amorphous structure and it cannot be identified using this kind of measurements.

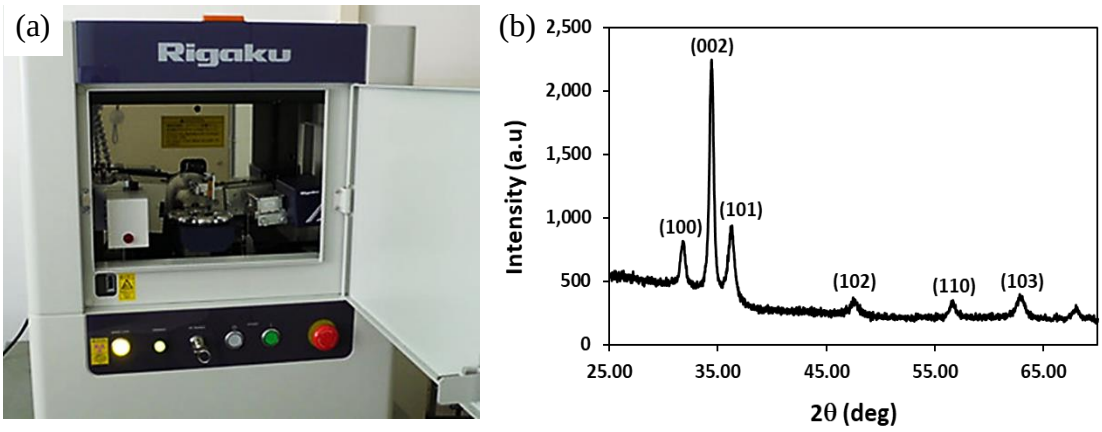


Figure 3.4: Rigaku Miniflex 600 XRD measurement system (a), XRD pattern of a deposited ZnO thin film (b).

In addition to the identification of a material and its crystallinity, the following parameters can be estimated or identified from the XRD data:

- The lattice constants, *a* and *c* are estimated using the formula [15]:

$$\frac{1}{d_{hkl}^2} = \frac{4}{3}\left(\frac{h^2 + hk + k^2}{a^2}\right) + \frac{l^2}{c^2} \qquad (\mathbf{3.9})$$

- The texture coefficient, *TC* is calculated using the formula [10]:

$$TC_{(hkl)} = \left(\frac{I_{(hkl)}/I_{r(hkl)}}{[1/n\sum I_{(hkl)}/I_{r(hkl)}]}\right) \qquad (\mathbf{3.10})$$

where d_{hkl} is the plane spacing, h, k, l are Miller's indices, and I and I_r are the measured and reference peak intensity, respectively.

- The crystal (grain) size, *D* is estimated using Scherer's formula [10]:

$$D = \frac{0.94\lambda}{\beta cos\theta_B} \qquad (\mathbf{3.11})$$

where λ is the wavelength of the XRD radiation source ($\lambda = 1.541$Å), β is the full width at half maximum (FWHM) of the diffraction peak, and θ_B is Bragg angle.

- The crystal strain, ε is estimated using the formula [70]:

$$\varepsilon = \frac{c - c_0}{c_0} \qquad (\mathbf{3.12})$$

where c and c_0 are is the crystal constant of deposited film and bulk material, respectively.

2- Scanning Electron Microscope (SEM)

SEM is a non-destructive technique which uses an electron beam (e-beam) to produce a microscale magnified image of the sample. The image is produced by scanning the sample with a focused electron beam and detecting the secondary and/or backscattered electrons signals that contain information about the surface topography and composition of the sample. As it's shown in Figure 3.5, SEM system consists of an electron gun, a lens system, scanning coils, an electron collector, and a cathode ray display tube (CRT) [69].

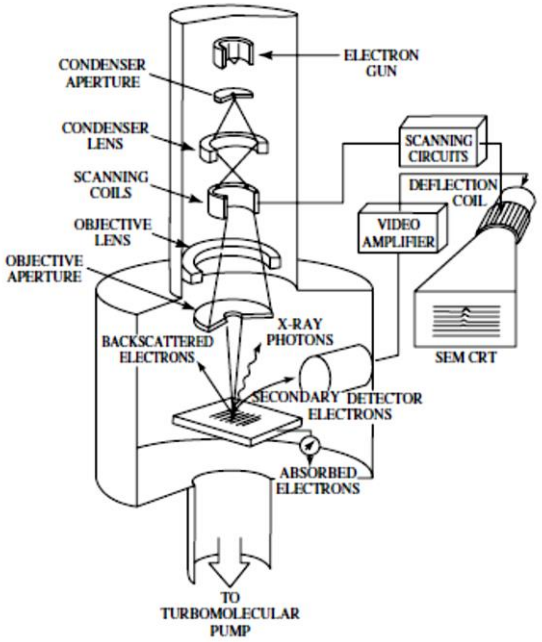


Figure 3.5: Schematic of a Scanning Electron Microscope [69].

The use of electrons has two main advantages over optical microscopes: much larger magnifications are possible since electron wavelengths are much smaller than photon wavelengths and the depth of field is much higher [69].

The microstructure surface topography of the deposited films was investigated using FEI QUANTA 400F brand SEM system (Figure 3.6a). This system, which belongs to the central laboratory of Middle East Technical University (METU, Ankara-Turkey), can provide magnification from 40x up to 250,000x. Throughout the produced images, one can study the surface topography and particles size or shape (morphology) of a sample in nanometers resolution. Combined with EDX (Energy Dispersive X-ay Spectroscopy), it is possible to reveal the elemental composition of any object under studies as well as its distribution/ mapping across the studied area. EDX elemental composition could be expressed quantitatively as weight percentage or atomic percentage. A sample of obtained SEM image for one of the deposited GZO thin films is shown in Figure. 3.6b.

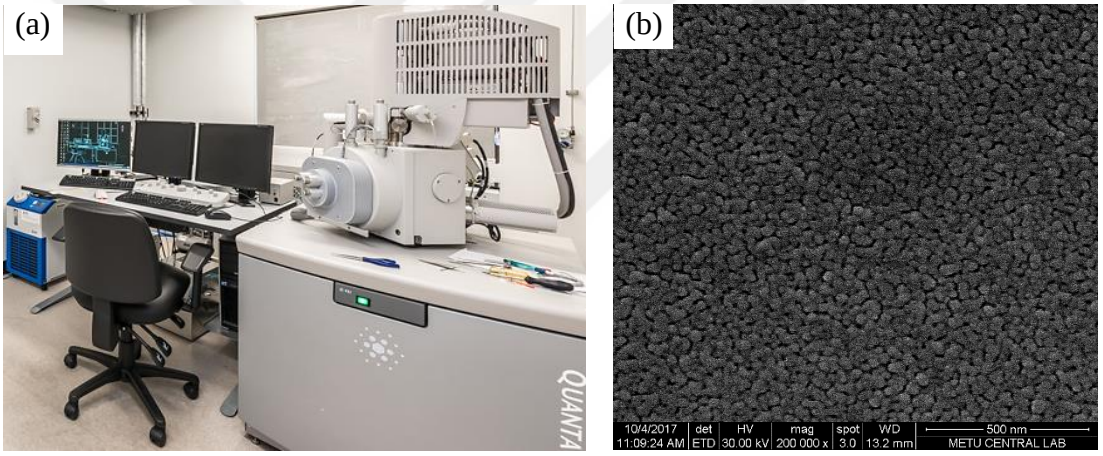


Figure 3.6: FEI QUANTA 400F brand SEM system (a), SEM image of a deposited GZO thin film (b).

3- Atomic Force Microscopy (AFM)

Atomic force microscopy (AFM) is a nondestructive tool, and it is suitable for conducting as well as insulating samples. It operates by measuring the force between a probe and the sample. As it's shown in Figure. 3.7, a laser beam is focused on the back of a cantilever that has a tip that interacts with a surface; the beam reflects into a four-quadrant photodetector. Normal forces between the tip and surface deflect the cantilever up or down. Lateral forces twist the cantilever left and right. These deflections are measured by monitoring the deflection of the reflected laser and be used to generate an image of the surface topography [71].

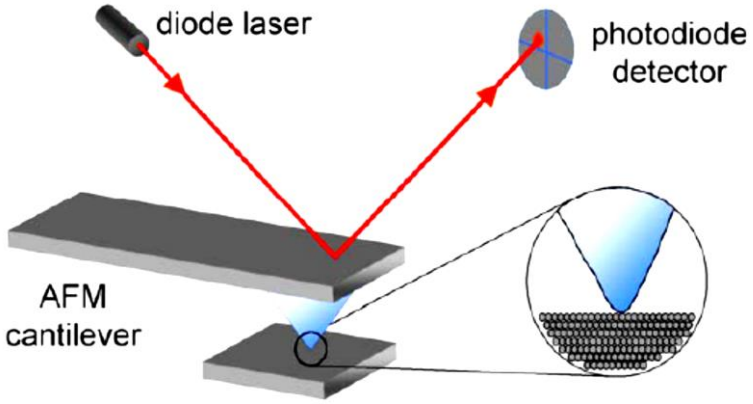


Figure 3.7: AFM schematic

Q-Scope 250 brand AFM system (Figure. 3.8a) was used to characterize the surface properties of the deposited thin films. A non-touching scan mode (wave mode) is used to produces a 3D topological view of the sample surface**.** The X-Y sample stage of this system can accommodate samples up to 5"½ x 5½" x 1", and scan size up to 50µm x 50µm is achievable. Moreover, the scan resolution can be adjusted up to 800 dpi to reveal greater surface detail (higher image quality). Throughout analyzing the produced image, many parameters can be estimated. Among these parameters, the most important ones are the root mean square (RMS) value of surface roughness and particles size and their histograms. A sample of obtained AFM image for one of the deposited GZO thin films is shown in Figure. 3.8b.

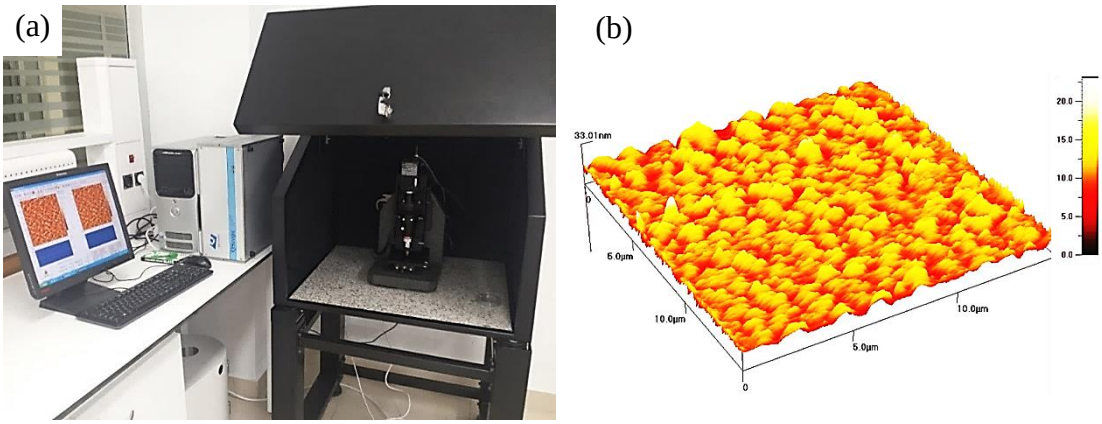


Figure 3.8: Q-Scope 250 brand AFM system (a), AFM image of a deposited GZO thin films (b).

4- Ultraviolet-visible (UV-vis) spectroscopy

UV-vis spectroscopy is a non-destructive technique used for measuring the transmittance and absorbance of solids, solutions and gases. It refers to absorption or reflectance spectroscopy in the ultraviolet-visible spectral region. A monochromator is used to select the wavelength at which a transmission or absorption measurement is made. A simple schematic of UV-vis spectroscopy system is shown in Figure 3.9. It measures the intensity of light passing through a sample (**I**) and compares it to the intensity of light before it passes through the sample ($\mathbf{I_0}$). The ratio $\mathbf{I/I_0}$ is called the "transmittance (T)" and is usually expressed as a percentage (T %). The absorbance, A is based on the transmittance and it can be calculated using the following relation [72]:

$$A = -\log(T\%/100) \qquad (\mathbf{3.13})$$

The UV-visible spectrophotometer can also be configured to measure reflectance. In this case, the spectrophotometer measures the intensity of light reflected from a sample (**I**) and compares it to the intensity of light reflected from a reference material ($\mathbf{I_0}$). The ratio $\mathbf{I/I_0}$ is called the "reflectance" and is usually expressed as a percentage (%R).

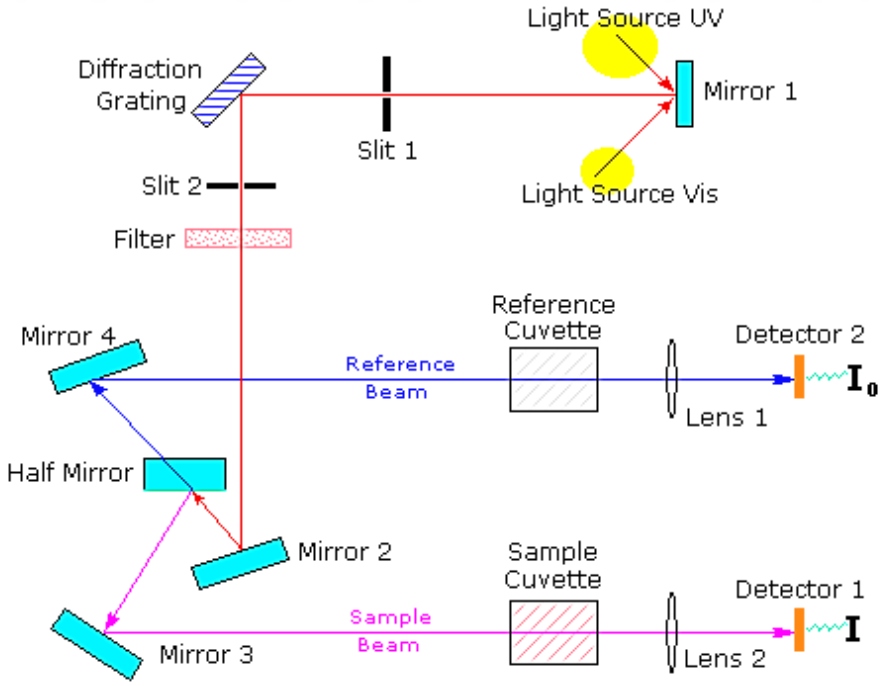


Figure 3.9: UV-Visible spectroscopy schematic

In the thesis work, UV-1700 series SHIMADZU brand dual-beam UV-vis spectroscopy (Figure 3.10a) was used for transmittance and absorbance measurements. The wavelength range of the measurements can be set from 190 to 1100 nm with adjustable wavelength step. A sample of transmittance measurement for one of the deposited GZO thin films is shown in Figure 3.10b. The measurement shows the wavelength bands in which the film is absorbing (non-transparent) and non-absorbing (transparent). According to Figure 3.10b, the deposited film is highly transparent in wavelengths above 400 nm, while it is almost completely absorbing in the wavelengths below 400 nm. Being the transmittance spectrum has fringes, this is an indicator that the film has a smooth and uniform surface.

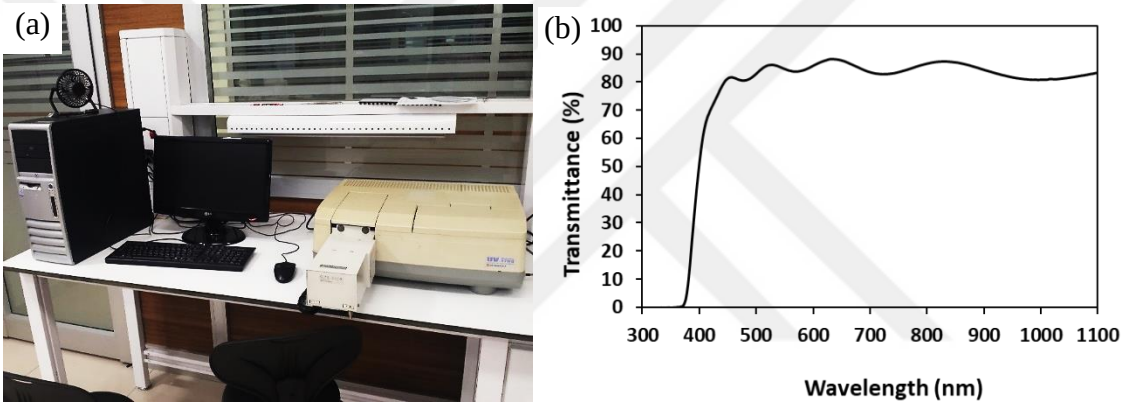


Figure 3.10: UV-170 SHIMADZU brand UV-vis spectroscopy system (a), measured transmittance spectrum of a deposited GZO thin film (b).

In addition to defining the absorbance and transparency spectra of the film, the following important parameters can be estimated using the measured transmittance and absorbance data:

- **Estimation of film thickness, *d* and refractive index, *n***

A well-known method called Swanepoel method [73] can be used to estimate the thickness and refractive index of the thin films. The application of Swanepoel method requires a creation of envelope curves of transmission maxima and minima as a continuous function of λ**.** Using magnitudes of maxima and corresponding minima from the envelopes, it is possible to find the refractive index *n* and the film thickness

d at any value of λ **.** By adjusting the order number of maxima, it is possible to calculate a more accurate value of *d* and consequently, an average value of *d* can be derived.

The steps of this method can be summarized as follows [73]:

1- Generating the envelopes of interference maxima and minima (Figure. 3.11).

A Matlab code was developed for the generation of maxima and minima envelops.

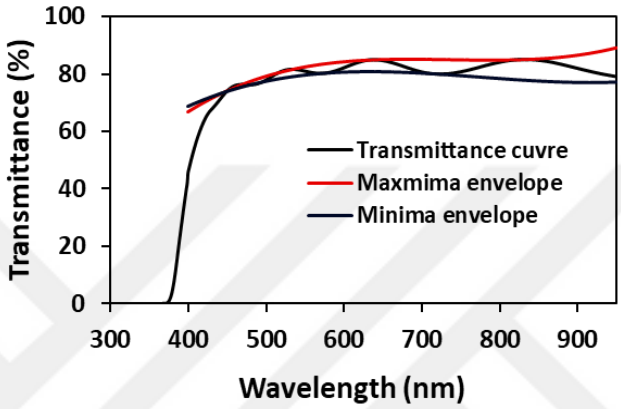


Figure 3.11: Measured transmittance spectrum with generated maxima and minima envelopes of a deposited GZO thin film.

2- Approximate value of the refractive index of the film, n_1 in the spectral region of medium and weak absorption, can be calculated by the expression**:**

$$n_1 = [N_1 + (N_1{}^2 - n_s{}^2)^{1/2}]^{1/2} \qquad (\mathbf{3.14})$$

and

$$N_1 = \frac{2n_s(T_M - T_m)}{T_M . T_m} + \frac{(n_s^2 + 1)}{2} \qquad (\mathbf{3.15})$$

where one value of T_M or T_m is an experimental interference extreme and the other one is derived from the corresponding envelope**.** The necessary values of n_s can be obtained from the transmittance spectrum of the substrate, T_s (λ) using the well-known equation:

$$n_s = \frac{1}{T_s} + (\frac{1}{T_s^2} - 1)^{1/2} \qquad (\mathbf{3.16})$$

3- Approximate value of the film thickness d_1, can be calculated by the expression**:**

$$d_1 = \frac{\lambda_1.\lambda_2}{2(\lambda_1.n_{e2} - \lambda_2.n_{e1})} \quad (\mathbf{3.17})$$

where; n_{e1} and n_{e2} are the refractive indices at two adjacent maxima (or minima) at λ_1 and λ_2**.**

4- The average value of the calculated approximate film thicknesses is used to calculate the "order number" m_0 for the different extremes using the equation:

$$2n_1.d_1(\text{average}) = m_0\lambda \quad (\mathbf{3.17})$$

and

$$m_0 = 2n_1d_1(\text{average})/\lambda \quad (\mathbf{3.18})$$

5- The accuracy of *d* can now be significantly increased by taking the corresponding exact integer or half integer values of m_0(m) associated to each extreme, where**:**

$$d_2 = m\lambda/2n_1 \quad (\mathbf{3.19})$$

6- The average value of d_2, can now be used to calculate more accurate value of the refractive index, n_2, where**:**

$$n_2 = m\lambda/2d_2(\text{average}) \quad (\mathbf{3.20})$$

- **Estimation of bandgap energy, E_g**

Tauc's model was used for graphically estimation of E_g using the measured transmittance spectrum along with the estimated thickness (Figure. 3.12). The model is based on the following equation [74]:

$$(\alpha hv)^2 = A(hv - E_g) \quad (\mathbf{3.21})$$

where α (cm^{-1}) is absorption coefficient, hv (eV) is photon energy, and A is a relation constant. The linear dependence of $(\alpha hv)^2$ with hv implies that the films are direct transition type semiconductors.

The absorption coefficient spectrum can be estimated from the measured transmittance spectrum using the following relation [74]:

$$\alpha\,(\lambda) = \frac{1}{d}\ln[T(\lambda)] \qquad (\mathbf{3.22})$$

where T is transmittance spectrum of films. The value of E_g is obtained by plotting $(\alpha hv)^2$ versus hv and extrapolating the linear region in the graph to the hv axis.

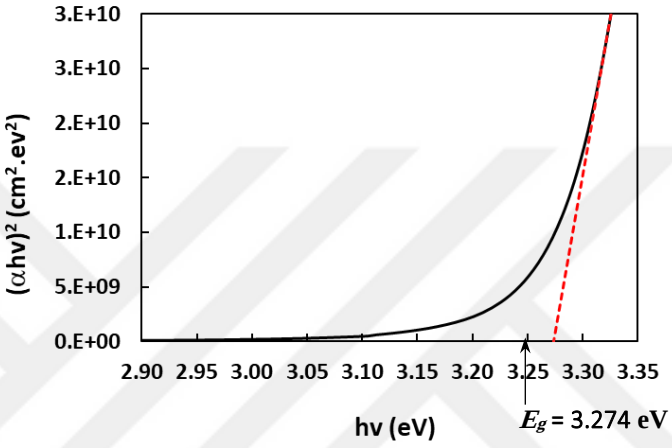


Figure 3.12: Tauc's bandgap energy of a deposited GZO film

- **Estimation of film porosity, *P***

The estimated value of *n* at certain wavelength is used to calculate the film porosity, *P* as follows [75]:

$$P = 1 - \frac{(n_{bulk}^2 + 2)(n_{film}^2 - 1)}{(n_{film}^2 + 2)(n_{bulk}^2 - 1)} \qquad (\mathbf{3.23})$$

where n_{film} and n_{bulk} are the refractive indices of the film and bulk material, respectively.

5- Four-point probe measurement

The electrical sheet resistance, R_{sh} of the deposited thin films was measured at room temperature by using the in-line four-point probe measurement system. Figure 3.13-a shows the schematic of the four-point probe measurement. As shown in Figure 3.13b,

the used measurement setup consists of Signatone S-302-4 Four-Point Probe stand and Keithley model 2400 source meter unit (SMU). The sheet resistance, R_{sh} of the film is calculated using the following formula [76]:

$$R_{sh} = \frac{\pi}{\ln(2)}\left(\frac{V}{I}\right) = 4.532\left(\frac{V}{I}\right) \qquad (\mathbf{3.24})$$

By knowing R_{sh} and film thickness, d, the electrical resistivity, ρ can be calculated as:

$$\rho = R_{sh}.d \qquad (\mathbf{3.25})$$

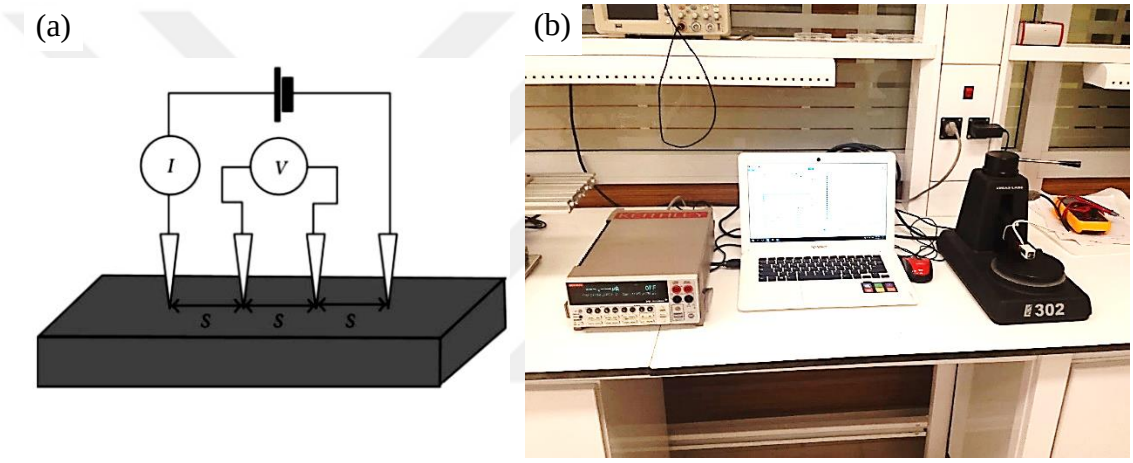


Figure 3.13: Layout of four-point probe measurement method (a), Setup of the measurement system (b).

6- Hall effect measurement

The Hall effect measurement technique has wide applications in the characterization of semiconductor materials. The key feature of Hall effect measurements is the ability to determine the carrier density, the carrier type, and the mobility. Essentially, the Hall effect can be observed when the combination of a magnetic field, B_Z applied along z-axis, and a current, I_x applied along the x-axis, of the sample causes an induced electrical field perpendicular (in y-axis) to both the applied magnetic field and the current (Figure 3.14a). The induced electric field in the y direction is called the Hall field, E_H which produces a voltage across the semiconductor, which is called the Hall voltage, V_H [64]. Nano Magnetics brand system (Figure 3.14b) was used to perform

room-temperature Hall effect measurements. The system is equipped with Van der Pauw and Hall bar measurement designs and temperature control option for low temperature-high temperature measurements which provide higher accuracy and wide options of measurements.

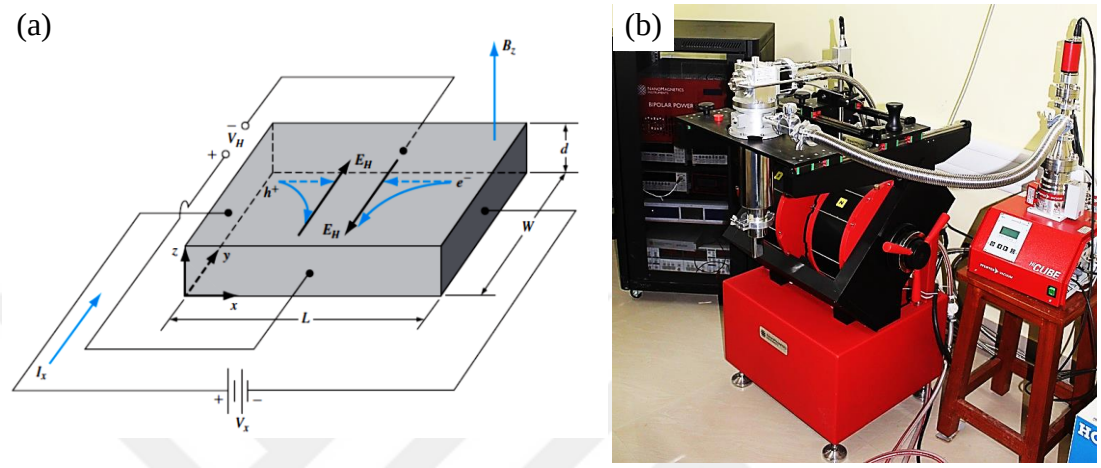


Figure 3.14: Schematic of Hall effect measurement (a) [64], Nano Magnetics Hall effect measurement system (b).

At room temperature measurements, the concentration of minority carriers in the extrinsic semiconducting material can be neglected and only the majority carrier's concentration is considered. Accordingly, for an n-type semiconductor, the majority carrier's concentration (electrons), n and mobility, μ_n of sample film material can be calculated as follows [64]:

$$n = -\frac{I_x B_z}{edV_H} \qquad (\mathbf{3.26})$$

and

$$\mu_n = \frac{I_x L}{enV_x W d} \qquad (\mathbf{3.27})$$

The resistivity of sample film can be derived as:

$$\rho = \frac{Wd}{L}\frac{V_x}{I_x} \qquad (\mathbf{3.28})$$

7. Calculation of film figure of merit, *FOM*

The quality of ZnO thin film as a transparent conductive oxide is judged according to its both optical and electrical properties. The ratio of the electrical conductivity, σ to the visible absorption coefficient, α is an appropriate quantitative measure used as a figure of merit (*FOM*) to identify the film quality, where [77]:

$$FOM = \sigma/\alpha = -1/[R_{sh} ln(T + R)] \qquad (3.29)$$

where R_{sh} is sheet resistance and T and R are the average transmittance and reflectance of the film, respectively. A larger value of *FOM* indicates that the film has better quality in terms of optical and electrical properties.

3.2 Fabrication and characterization of n-ZnO:X (GZO)/p-Si heterojunction-based devices

Figure 3.15a shows the basic structure of the fabricated n-GZO/p-Si heterojunction-based photodiode/solar cell devices. The basic structure was first optimized in terms of the emitter layer (sol-gel derived n-GZO thin film) parameters including thickness, doping ratio and crystallinity, the metallization of front and back sides and the sequence of fabrication steps. The metal NPs (solution-processed) including Au NPs and Ag NPs of 100 nm size were then incorporated into the device structure for enhancing the optical properties and improving the overall performance of device (Figure 3.15b).

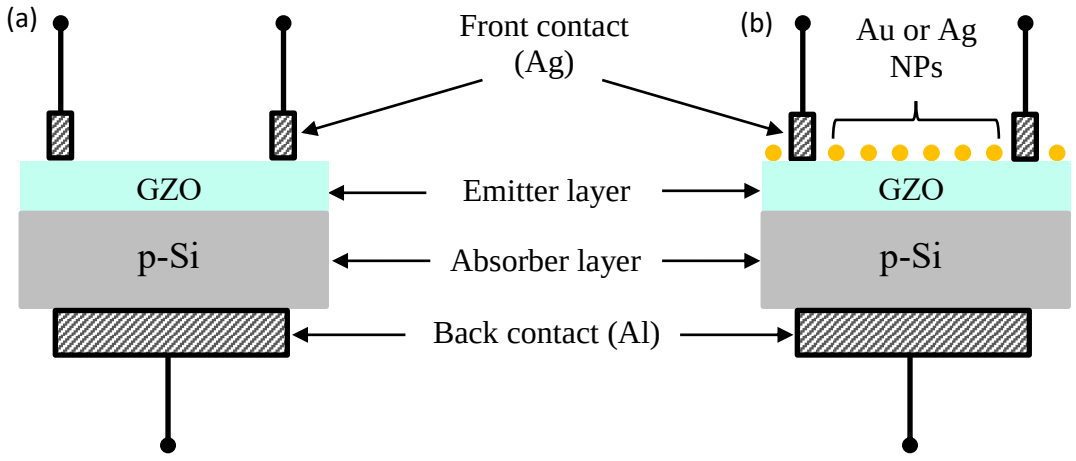


Figure 3.15: Schematic diagram of basic structure (a) and metal NPs-coated structure (b) of n-GZO/p-Si heterojunction-based device.

Two types of circular single crystal, (100) orientation plane, 1 side polished, boron doped p-Si wafers were used as a substrate and p-type side of the device heterojunction. One type is 4" diameter, 500µm thick and 1-20 Ω.cm resistivity. The other type is 3" diameter, 380µm thick and 1-10 Ω.cm sheet resistance. These Si wafers were diced to small square wafers of 1.5x1.5 cm^2 for device fabrication. The various layers as well as the output characteristics of the fabricated devices were characterized to investigate the properties of layers and performance of device. A measurement setup was used to measure the output current-voltage (*I-V*) characteristics for the devices in the dark and under illumination of sun simulator light source (AM1.5) and UV light source.

2.4.3 Fabrication process of device

Figure 3.16 presents the sequence of the main steps of the fabrication process of the devices. A detailed description for these steps is given below:

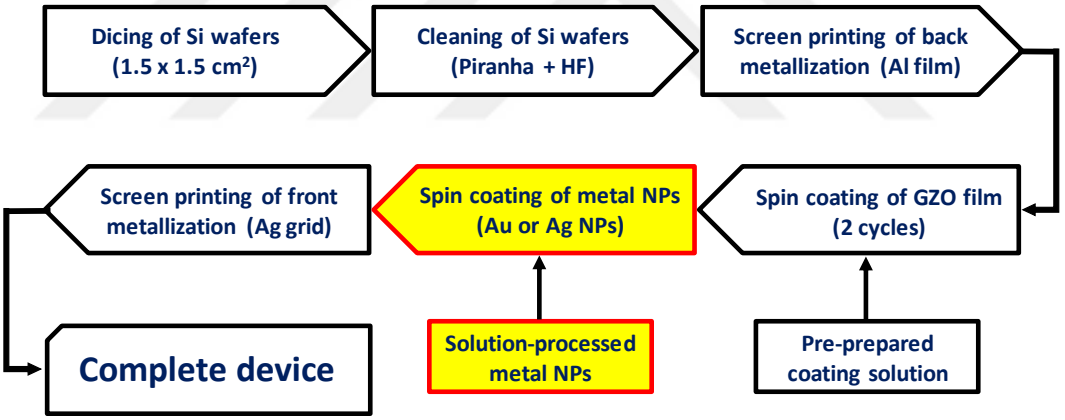


Figure 3.16: Fabrication sequence for n-GZO/p-Si heterojunction-based devices

1- Preparation of coating solution

The coating solution for the deposition of ZnO:X thin films is prepared using the developed recipe during the previous part of work.

2- Dicing of Si wafers

SPI supplies brand diamond scribe, refillable style 60, included angle: 60° was used to dice the Si wafer to square pieces of 1.5 x 1.5 cm^2 as shown in Figure 3.17. About 24 and 16 square pieces can be obtained from 4" and 3" wafers, respectively.

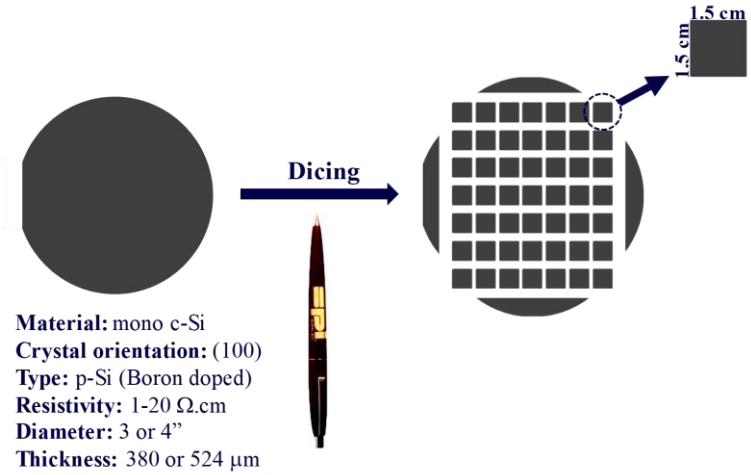


Figure 3.17: Dicing of Si wafers

3- **Cleaning of Si wafers**

Cleaning process is crucial for Si wafers for removal of surface contamination and native SiO_2 layer. Both Piranha and RCA cleaning standards were applied for removal of organic and metallic contamination and hydrofluoric acid (HF) cleaning standard was applied for removal of SiO_2 layer. According to the used recipe, the Si wafer undergoes the following sequential steps of cleaning process:

1	• Immersing in Piranha solution for 15 min at 80 °C. • Piranha: (sulfuric acid, H_2SO_4 : hydrogen peroxide, H_2O_2 = 3:1).
2	• Immersing in DI water for 30 s.
3	• Immersing in RCA-1 solution for 5 min at 80 °C. • RCA-1: (DI water : ammonium Hydroxide, NH_4OH : H_2O_2 = 5:1:1).
4	• Immersing in DI water for 3 min.
5	• Immersing in HF (2 %) for 1 min at RT.
6	• Immersing in DI water for 30 s.
7	• Immersing in RCA-2 solution for 15 min at 80 °C. • RCA-2: (DI water : hydrochloric Acid, HCL : H_2O_2 = 1:1:6).
8	• Immersing in DI water-1 for 5 min + 30 s in DI water-2.
9	• Thermal drying at 150 °C for 10 min.

3- Spin coating of ZnO:X film and metal NPs

A pre-prepared coating solution is used for the deposition of n-ZnO:X thin films on the front (polished) side of the p-Si substrate using the spin coating technique. The film thickness can be controlled to a certain extend by altering the number of coating cycles. The same technique is used to deposit the solution processed Au or Ag NPs on the n-ZnO:X layer. The details of the deposition process of both ZnO:X films and solution processed metal NPs are described in sections 3 3.1.1.1 and 3.1.1.2.

4- Metallization of device

The realization of ohmic metal/semiconductor contact is a tricky requirement for both the front and back contacts of the device. Generally, there are two alternatives that can be used to get a such ohmic contact; one alternative is using a metal of work function, $\boldsymbol{\Phi}$ higher than that of the p-type semiconductor ($\boldsymbol{\Phi}_{metal} > \boldsymbol{\Phi}_{p\text{-}Si}$) or lower than that of the n-type semiconductor ($\boldsymbol{\Phi}_{metal} < \boldsymbol{\Phi}_{n\text{-}Si}$), the other alternative is forming a heavily doped semiconductor layer at the contact side which provide a tunneling transportation mechanism of majority carriers [64]. The metallization can be made using vacuum thermal evaporation or screen-printing techniques. The later technique was used in the thesis work.

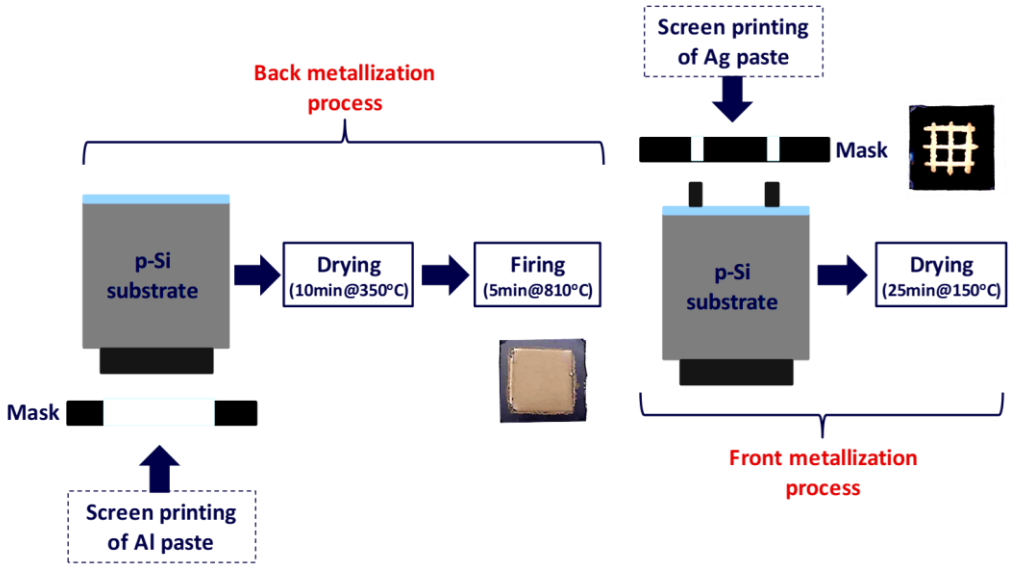


Figure 3.18: Metallization process schematic

- **Front metallization:**

Silver, Ag paste (SIGMA-ALDRICH, product numbers 735825) was used for front metallization grid. Silver is a good choice for forming ohmic contact with ZnO layer since it has a wok function value higher than that of ZnO material ($\boldsymbol{\Phi}_{Ag}$ ~ 4.26 eV [64] < $\boldsymbol{\Phi}_{ZnO}$ ~ 4.5 eV [77]). In spite the work function condition is theoretically satisfied, the ohmic contact behavior is not necessary to be realized and it should be tested experimentally. Figure 3.19a shows the measured current-voltage relation through the Ag/ZnO contact and the linear relation confirms the formation of ohmic contact behavior. The screen-printing technique was used to apply the Ag paste on the top surface of device. A mask was used to form a regular grid (Figure 3.18) to allow the passing of light to the device. The applied paste was dried thermally at 150 ^{o}C for 25 min.

- **Back metallization:**

The back metallization of device was performed using Aluminum, Al paste (BL01 series LEED-INK Brand). Due to the high work function value of p-Si material (~ 4.91 eV for (100)), it is generally difficult to realize a metal ohmic contact with it based on the work function condition. Instead, forming a heavily doped p^{++}-Si thin layer in contact with the metal is more practical alternative to form ohmic contact behavior based on tunneling transportation mechanism of majority carriers [64]. Al is a proper choice as a metal to form an ohmic contact with p-Si semiconductor. Al is a trivalent atom and it can be used to act as an acceptor dopant to dope the p-Si to form p^{++}-Si.

To form ohmic Al/p-Si back contact for our device, Al paste is applied on the back surface of the p-Si substrate and dried thermally at 350 ^{o}C for 10 min, then it is immediately exposed to a firing process at 810 ^{o}C for 5 min. After the firing process, p^{++}-Si thin layer in contact with Al film is formed. The formation of p^{++}-Si thin layer underneath the Al film ensures the realization of ohmic contact, and also leads to formation of back p-Si/p^{++}-Si junction which facilitates the collection of photogenerated charge carriers [78], this junction is known as back surface field (BSF). Figure 3.19b shows the measured *I-V* relation through the Al/p-Si contact. The linear *I-V* relation exhibits that the contact has a perfect ohmic behavior.

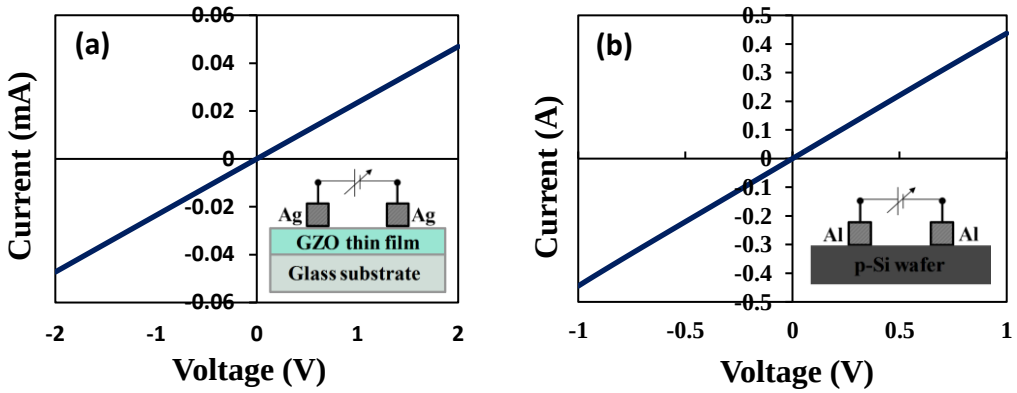


Figure 3.19: Measured *I-V* characteristics of Ag/GZO front contact (a), and Al/p-Si back contact (b).

2.4.4 Performance characterization of devices

The fabricated devices were characterized for the investigation of their overall performance and estimation of some of their parameters. A measurement setup consisting of Abet Technology Brand sun simulator and Keithley 2400 source meter unit (SMU) was used for measuring the output current-voltage (*I-V*) characteristics of the fabricated devices under dark and illumination conditions. Through Keithley 2400 SMU, the *I-V* measurement is performed using the four-wire configuration (Figure 3.20) which provides more accurate measurement compared to two-wire configuration since the voltage drop on the connection wires can be avoided. The sun simulator provides light of AM1.5 spectrum distribution of 100 mW/cm^2 intensity. The sun simulator measurement setup and a sample of measured *I-V* characteristics under dark and illumination conditions for one of the fabricated devices are shown in Figure 3.21.

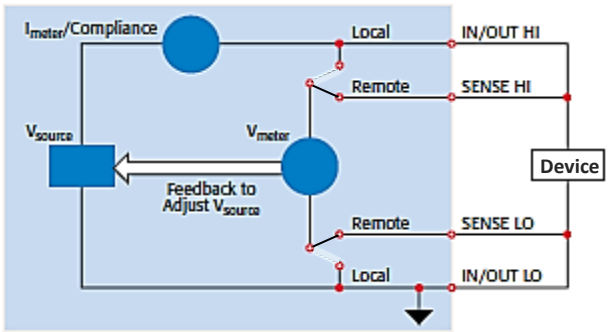


Figure 3.20: Four-wire configuration for the *I-V* measurement using Keithley 2400 SMU.

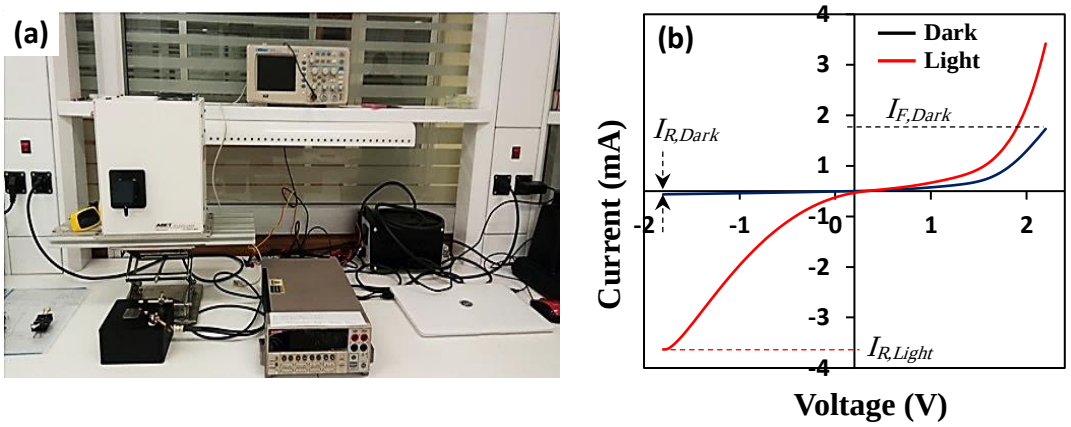


Figure 3.21: Sun simulator measurement setup (a), Dark and Light *I-V* characteristics of a fabricated device (b).

From the measured dark and illuminated *I-V* characteristics, the device can be modelled, and some parameters can be estimated as follows [66, 78, 79]:

- The dark *I-V* curve represents a diode behavior which can be modeled using the following general diode equation:

$$I = I_o\left(e^{qV/nkT} - 1\right) \qquad (\mathbf{3.30})$$

where I is the output current, I_o is the reverse saturation current, V is the applied voltage, n is the junction ideality factor, T is the absolute temperature, q is the electron charge, and k is Boltzmann constant and:

- I_o can be determined by an extrapolation of the forward bias ln(I)-V curve to $V = 0$.
- The ideality factor, n can be calculated from the slope of the straight-line region of the forward bias ln(I)-V plot and can be written as:

$$n = \frac{q}{kT}\frac{dV}{d(\ln I)} \qquad (\mathbf{3.31})$$

- The height of zero bias barrier, ϕ_{bo} can be calculated using the following formula:

$$\phi_{bo} = \frac{kT}{q}\ln\left(\frac{AA^*T^2}{I_s}\right) \qquad (\mathbf{3.32})$$

where A^* is the theoretical Richardson constant and A is the diode area.

- The rectification performance of the device is evaluated using the measure of rectification ratio (*RR*), where:

$$RR = \left| \frac{I_{F,Dark}}{I_{R,Dark}} \right|_{\pm V} \quad (\mathbf{3.33})$$

- The light to dark forward current (*LDFC*) is calculated as follows:

$$LDFC = \left| \frac{I_{F,Lght}}{I_{F,Dark}} \right|_{V_F} \quad (\mathbf{3.34})$$

- The device photosensitivity (*PS*) in the reverse bias region is calculated as follows:

$$PS = \left| \frac{I_{R,Light}}{I_{R,Dark}} \right|_{V_R} \quad (\mathbf{3.35})$$

- The device photoresponsivity (*PR*) in the reverse bias region is calculated as follows:

$$PR = \left| \frac{I_{R,Light}}{G.A} \right|_{V_R} \quad (\mathbf{3.36})$$

where G is the incident light intensity (mW/cm^2) and A is the device active area (cm^2).

- If the device exhibits good solar cell behavior, then the light *I-V* curve will be as it is shown in Figure 3.22, and it can be modeled by modifying the general diode equation as follows:

$$I = I_o \left(e^{qV/nkT} - 1 \right) - I_L \quad (\mathbf{3.37})$$

where I_L is the photogenerated (light) current which is directly proportional to the intensity of incident light.

From the light (illuminated) *I-V* curve, the following performance parameters can be extracted [66]:

- Short circuit current, I_{sc} which is approximately equal to I_L which is given by:

$$I_L = eG(L_N + W + L_p) \quad (\mathbf{3.38})$$

where G is carrier's generation rate, L_N and L_P is the diffusion length of minority carriers for electrons and holes, respectively, and W is the width of the depletion region.

▪ Open circuit voltage, V_{oc} is given by:

$$V_{oc} = \frac{kT}{e}\left(\frac{I_L}{I_s} + 1\right) \qquad (\mathbf{3.39})$$

▪ Fill factor, FF is given by:

$$FF = \frac{I_{mp}V_{mp}}{I_{sc}V_{oc}} \qquad (\mathbf{3.40})$$

▪ Efficiency, η is given by:

$$\eta = \frac{P_{max}}{P_{in}} = \frac{I_{mp}V_{mp}}{P_{in}} = \frac{I_{sc}V_{oc}FF}{P_{in}} \qquad (\mathbf{3.41})$$

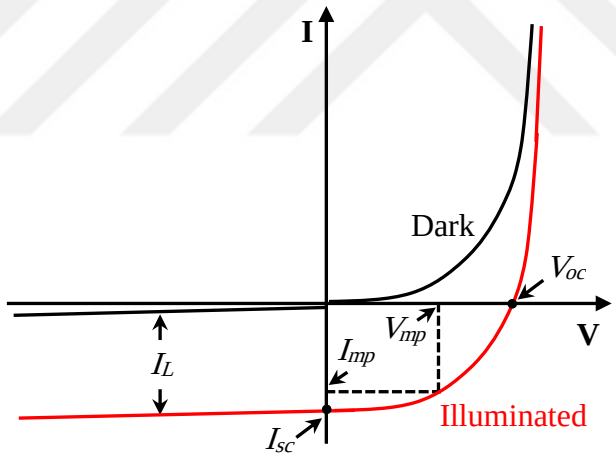


Figure 3.22: Dark and Illuminated *I-V* characteristics of a standard solar cell

CHAPTER 4

RESULTS AND DISCUSSION

4.1 Deposited ZnO:X thin films

As we mentioned in section 3.1.1.1, the experimental work included the deposition of Al, Ga and B single-doped ZnO thin films and Ga and B co-doped ZnO thin films. The Al and Ga single-doped ZnO thin films were successfully deposited and the results were very promising. The situation was different for the B single-doped and B and Ga co-doped ZnO films. No efficient doping of ZnO with B was obtained, and the results of the deposited films were not encouraging. In this chapter, therefore only the results of Al-doped and Ga-doped ZnO thin films are presented and discussed.

4.1.1 Al-doped ZnO (AZO) thin films

Many experiments for the deposition of AZO thin films were carried out in purpose of optimizing the whole process of sol-gel method. A typical recipe developed for the deposition process is given in Table 3.3. In this section, the detailed results of two important experiments for the deposition of AZO thin films are presented and discussed.

1- Investigation of solvent-stabilizer combinations for AZO thin films

In order to investigate the effects of the most used solvents and stabilizers on the properties of deposited ZnO thin films, six combinations of two solvents (ethanol and 2-methoxyethanol) and three stabilizers (monoethanolamine (MEA), diethanolamine (DEA) and triethylamine (TEA)) were used in the preparation of coating solutions for the deposition of AZO thin films. These solvent-stabilizer combinations include ethanol-MEA, ethanol-DEA, ethanol-TEA, 2-methoxyethanol-MEA, 2-methoxyethanol-DEA and 2-methoxyethanol-TEA. The corresponding deposited AZO films are designated as A-MEA, A-DEA, A-TEA, B-MEA, B-DEA, B-TEA, respectively. Aluminum nitrate nonahydrate ($Al(NO_3)_3.9H_2O$) was used as an Al dopant precursor (DP). The coating solutions were prepared under the conditions; 0.2 mol/l solution molarity, 1:1 molar ratio of stabilizer to (ZAD + DP), and 3 % doping

ratio. Five spin coating cycles was applied under the conditions; 2000 rpm spin speed for 30 sec and 10 sec spin acceleration time. The values of the other parameters of the deposition process are given in Table 3.3 and the details of the deposition process is described in section 3.1.1.1.

As shown in Table 4.1, the obtained results generally showed that the crystallinity quality, surface morphology and electrical sheet resistance of films are strongly affected by the type of solvent-stabilizer combination, while comparable optical properties were observed for the all films except for the film of B-TEA combination which had significantly lower transmittance among the other films.

Table 4.1: The estimated parameters for the AZO films of various solvent-stabilizer combinations.

Parameter	AZO films					
	A-MEA	**A-DEA**	**A-TEA**	**B-MEA**	**B-DEA**	**B-TEA**
Grain size, *D* (nm)	16.61	35.85	13.90	16.08	14.22	14.88
Preferred crystal orientation	(002)	(002)	(002)	(002)	(002)	(002)
Peak Intensity, *PI* of (002) plane	2255	289	553	533	69	585
Texture coefficient, *TC* of (002) plane	6.09	3.25	5.59	4.01	4.33	5.28
PI/*TC* of (002) plane	371	89	99	133	16	111
Lattice strain, ε (%)	0.099	0.020	0.128	0.118	0.174	0.277
Surface roughness, RMS (nm)	2.85	23.91	18.21	0.47	0.52	34.75
Average visible transmittance, T_{avg} (%)	87.85	85.22	82.90	82.28	83.96	73.04
Optical bandgap energy, E_g (eV)	3.274	3.239	3.273	3.244	3.299	3.212
Sheet resistance, R_{sh} (MΩ/□)	11.32	262.7	21.74	20.83	81.54	12.68
Figure of merit, *FOM* ($x10^{-7}\ \Omega^{-1}$)	6.82	0.24	2.45	2.46	0.70	2.51

The measured XRD patterns of the deposited films are illustrated in Figure 4.1. The results reveal the polycrystalline structure of the films with XRD patterns match that of the standard XRD pattern of ZnO crystal (JCPDS 036-1451) which confirm the formation of the hexagonal wurtzite structure of ZnO material. Generally, the all films exhibit a preferred crystal orientation corresponding to (002) plane along the *c*-axis perpendicular to the surface of the substrate and weak trace of peaks corresponding to (100) and (101) planes exists. It is clearly noticeable that the crystallinity quality of the films is altered by changing the solvent-stabilizer combination. Referring to the measured XRD patterns, both the width and intensity of the XRD peaks of the films

are significantly affected reflecting the change in crystal size, degree of material crystallinity and texture dominance of the preferred crystal orientation for these films.

Table 4.1 shows some physical parameters derived from the XRD data. The grain size (*D*) and texture dominance of the preferred plane of the films are evaluated by means of Scherer's formula and texture coefficient (*TC*), respectively. The equations 3.10 and 3.11 were applied for the calculations of *TC* and *D*, respectively. The calculated values are shown in Table 4.1. In comparison, among all films, the film of ethanol-MEA combination exhibits distinguished good crystalline material of highly preferred crystal orientation at (002) plane, while the film of 2-methoxyethanol-DEA combination exhibits very poor crystallinity. On the other hand, amongst all films, the crystal size is exceptionally larger for the film of ethanol-DEA combination (Table 4.1). The observed enhancement in material crystallinity for the MEA-stabilized AZO films was reported by P. H. Vajargah et al. [18] for sol-gel derived ZnO films. This observation confirms the advantage of using MEA stabilizer in this regard.

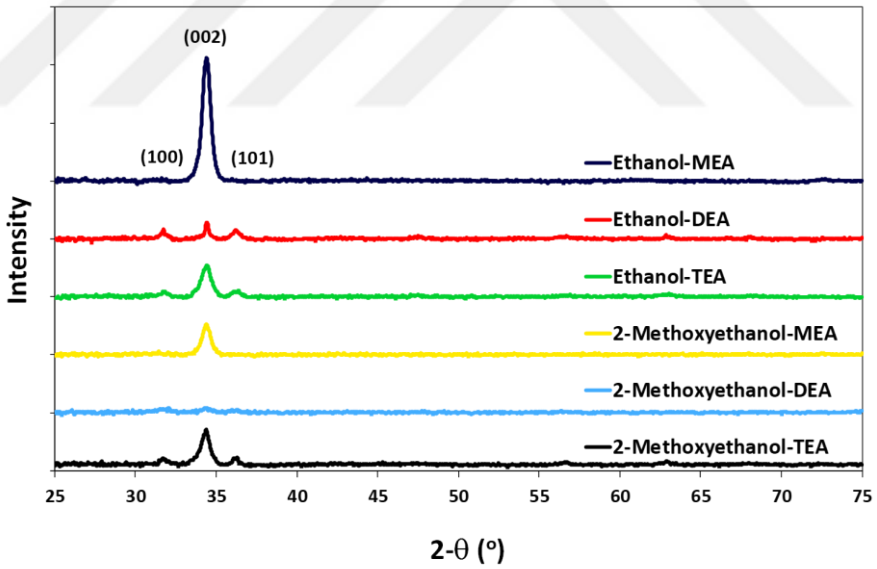


Figure 4.1: XRD patterns for the AZO films of various solvent-stabilizer combinations

The AFM images of the deposited films are shown in Figure 4.2. Similar to the case of crystal structure, the surface morphology of the films is also affected by the used solvent-stabilizer combination. Except for the case of TEA stabilizer, the 2-methoxyethanol-solved films have generally much smoother surfaces, and this may be attributed to the fact that the 2-methoxyethanol solvent has much lower volatility

compared with the ethanol solvent. This result demonstrates that the 2-methoxyethanol solvent is preferred when the low surface roughness is required. The root mean square (RMS) values of the surface roughness of the films are shown in Table 4.1. The lowest RMS value is obtained using 2-methoxyethanol-MEA combination while the highest value is obtained using 2-methoxyethanol-TEA combination. Generally, the effects of both the solvents and the stabilizers are interrelated to each other and the structural properties of the deposited films are affected by their combinations rather than as individuals.

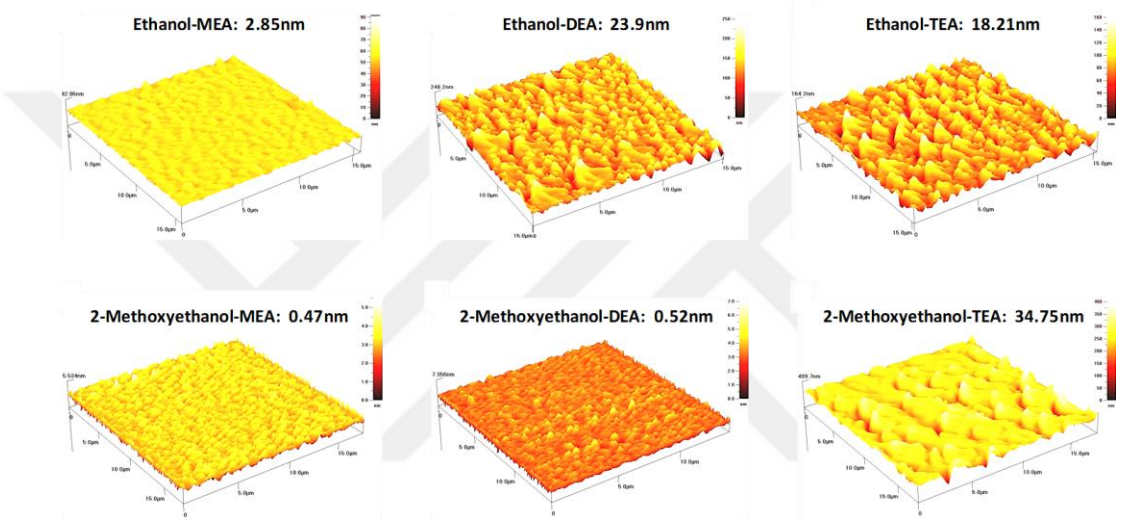


Figure 4.2: AFM images for the AZO films of the various solvent-stabilizer combinations.

As shown in Figure 4.3, except for the film of 2-methoxyethanol-TEA combination, all the films show good optical transmittance with an average value above 82% in the wavelength range from 400 to 1100 nm (Table 4.1). By comparing the group of ethanol-solved films with the group of 2-methoxyethanol-solved films, the optical transmittance is generally higher for the first group. Accordingly, it can be concluded that the ethanol solvent has an advantage over 2-methoxyethanol in this aspect. In addition, it was reported by P. H. Vajargah et. al [18] that both MEA and DEA-containing sol is so stable and maintains the as-prepared sol's transparency, while TEA-containing sol gets semitransparent and does not become clear by heating. Again, the optical properties of the deposited films are affected by the solvents and stabilizers as combinations rather than as individuals. Tauc's model (described in section 3.1.2) was applied to estimate the optical bandgap energy (E_g) for the films using the

measured transmittance data. The obtained Tauc's curves are shown in inset of Figure 4.3. As shown in Table 1, there is an observable fluctuation in the estimated values of E_g for the films of different solvent-stabilizer combinations. The highest and lowest values of E_g are 3.299 eV and 3.212 eV for the films of 2-methoxyethanol-DEA and 2-methoxyethanol-TEA combinations, respectively. Despite there is no clear trend between the E_g and film crystallinity, it may be reported here that the highest value of E_g belongs to the film of the poorest crystallinity.

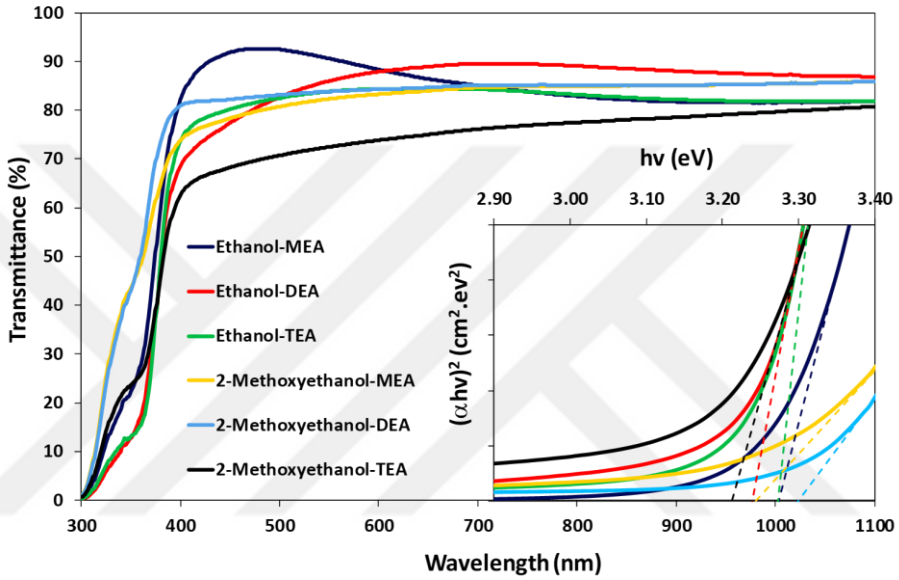


Figure 4.3: Optical transmittance spectra for the AZO films of various solvent-stabilizer combinations, the Tauc's graph is shown in the inset.

The change in the structural properties of the films affects their electric properties. As shown in Table 4.1, DEA-stabilized films have much higher sheet resistance compared with the other films. This can be attributed to the poor crystallinity of these films. Accordingly, it can be concluded that DEA stabilizer is not preferred in this side. On the other hand, lower sheet resistance was obtained for the MEA-stabilized and TEA-stabilized films. In spite both MEA and TEA stabilizers are competitive in this aspect, MEA is advantageous over TEA when the transparency feature is also considered. Taking in account both the transparency and sheet resistance, the ethanol-MEA combination is preferable over the other combinations as the film of this combination has the highest *FOM*. As a result of this experiment, the ethanol-MEA combination was used for the deposition of AZO and GZO films.

2- Investigation of doping ratio for AZO thin films

In this experiment, AZO thin films with different Al contents (0, 1, 2, 4, 3, 4 and 5 at. %) were deposited on glass substrates. According to the results of the experiment of investigating the effects of solvents and stabilizers for AZO films, the ethanol-MEA combination was used in the preparation of coating solutions for these films. Aluminum nitrate nonahydrate ($Al(NO_3)_3.9H_2O$) was used as an Al dopant precursor (*DP*). The coating solutions were prepared under the conditions; 0.5 mol/l solution molarity, 1:1 molar ratio of MEA to (ZAD + DP). Ten spin coating cycles was applied under the conditions; 2000 rpm spin speed for 30 sec and 8 sec spin acceleration time. The values of the other parameters of the deposition process are given in Table 3.3 and the details of the deposition process is described in section 3.1.1.1.

Table 4.2 summarizes the measured and estimated parameters for the deposited films. Generally, with changing the doping ratio, the obtained results showed that the crystallinity quality and electrical resistivity of the films are strongly affected, while the optical transmittance is slightly affected. Based on the FOM measure, the AZO-1 film (1 at. %) is the best among the deposited films.

Table 4.2: The estimated parameters for the deposited AZO films of various doping ratios.

Parameter	**AZO films**					
	Undoped	**1 at. %**	**2 at. %**	**3 at. %**	**4 at. %**	**5 at. %**
Film thickness, *d* (nm)	730	835	792	757	763	773
Grain size, *D* (nm)	28.0	18.6	15.9	13.5	-	-
Preferred crystal orientation	(002)	(002)	(002)	(002)	-	-
Peak intensity, *PI* of (002) plane	3262	2213	1718	594	-	-
Texture coefficient, *TC* of (002) plane	4.25	4.19	4.16	3.91	-	-
Peak intensity/*TC* of (002) plane	768	528	413	152	-	-
Lattice strain, ε (%)	0.0371	0.0385	0.0495	0.1532	-	-
Porosity, *P* (%) [at λ = 600 nm]	22	27	25	23	21	22
Average visible transmittance, T_{avg} (%)	87.56	88.44	86.58	87.65	87.44	87.47
Optical bandgap energy, E_g (eV)	3.261	3.261	3.263	3.273	3.275	3.283
Electrical resistivity, ρ ($x10^{-2}\Omega.m$)	-	47.72	61.66	72.39	137.34	178.56
Figure of merit, *FOM* ($x10^{-6}\,\Omega^{-1}$)	-	16.1	8.9	7.9	4.14	3.23

The formation of the hexagonal wurtzite polycrystalline structure of the deposited films is confirmed by the measured XRD patterns shown in Figure 4.4. The obtained XRD patterns match that was obtained for the AZO films deposited using ethanol-MEA combination (Figure 4.1). Note that the AZO film of ethanol-MEA combination shown in Figure 4.1 has 3 at. % Al content and its thickness is much thinner compared to that of the AZO films in Figure 4.4 (the solution molarity and coating cycles are 0.2 Ml^{-1} and 5 for the films in Figures 4.1 against 0.5 Ml^{-1} and 10 for the films in Figures 4.4). Generally, the all films exhibit a preferred crystal orientation corresponding to (002) plane along the *c*-axis perpendicular to the surface of the substrate and weak trace of peaks corresponding to (100), (101), (102), (110), (103), (112) and (004) planes exists. It is clearly noticeable from Figures 4.4 that the crystallinity quality of the films is deteriorating with increasing the doping ratio. The estimated values of grain size (*D*), texture coefficient (*TC*) and lattice strain (ε), shown in Table 4.2, are also confirm this note. As the doping ratio increases, both *D* and *TC* decrease and ε increases reflecting the deterioration in the crystallinity quality.

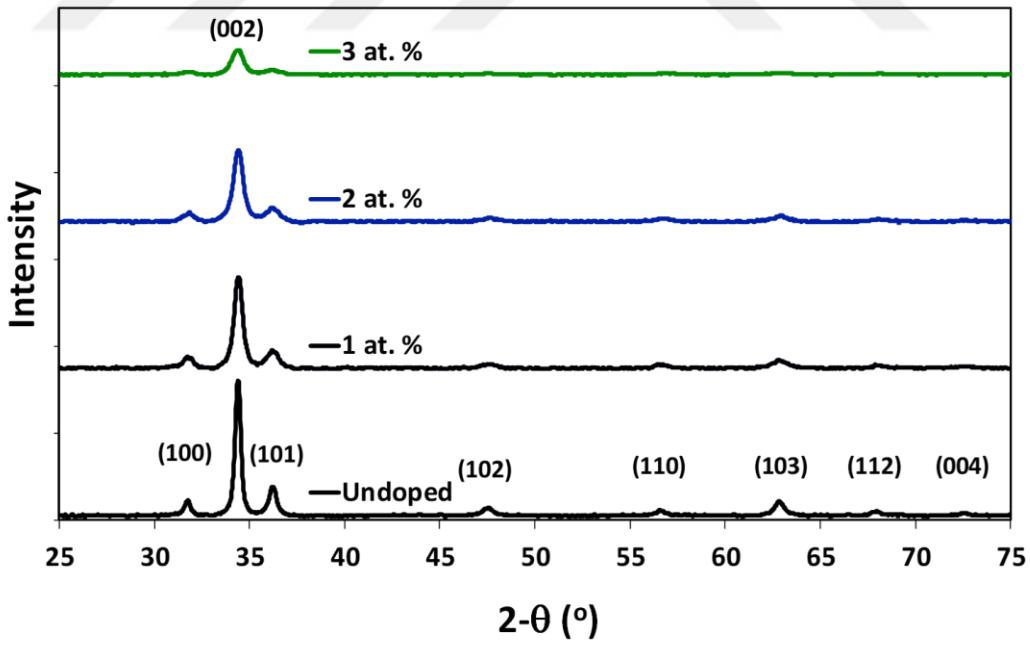


Figure 4.4: The measured XRD patterns for the deposited AZO thin films of various doping ratio.

Figure 4.5 shows the measured transmittance spectra for the films. The presence of the interference fringe patterns is an indicator for the smooth surfaces and high-optical quality of the films. As shown in Table 4.2, a transmittance of average value higher than 85 % in the wavelength range from 400 to 1100 nm is exhibited by the all films. Although no clear trend exists between the average transmittance and doping ratio, the film of 1 at. % doping ratio has the highest value of average transmittance among the other films. This film has a porosity value higher than the other films which can be the reason for its high transmittance. The values of the optical bandgap energy (E_g) estimated from Tauc's plots (the inset of Figure 4.5) for the films are shown in Table 4.2. A clear trend exits showing a widening in the optical bandgap energy with increasing the doping ratio. Such a widening in E_g is a result of the change in the structural and electrical properties of the films with doping. In particular, the change in the grain size, strain and conductivity of the films affect strongly the value of E_g [19, 20]. In our case, E_g increases with increasing the doing ratio which causes an increase in the strain and a decrease in the grain size.

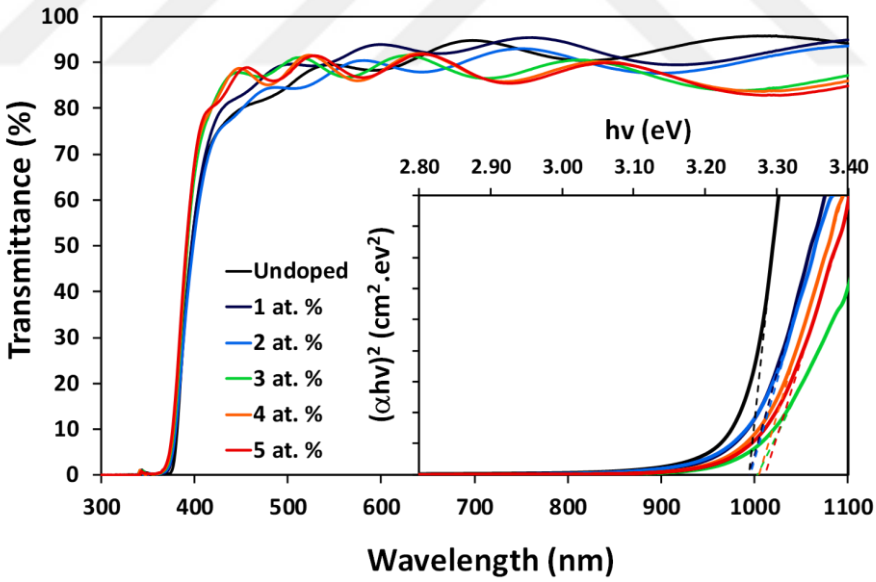


Figure 4.5: Optical transmittance spectra for the AZO films of various doping ratios, the Tauc's graph is shown in the inset.

Figure 4.6 presents the measured resistivity for the AZO films. A considerable improvement in the conductivity was obtained for the AZO film of 1 at. % doping ratio over the undoped ZnO film. Further increase in the doping ration causes a decrease in

the conductivity for the AZO films. Referring to the results shown in Table 4.2, the conductivity of AZO films has a direct relation with the grain size and inverse relation with the strain of the films. This result is consistent with literature [75, 80].

Considering both the transmittance and conductivity, the quality of the AZO films was judged using the figure of merit, *FOM* measure defined in Equation 3.29. According to this measure, the AZO film of 1 at. % doping ratio has the highest quality as clearly shown in Figure 4.6.

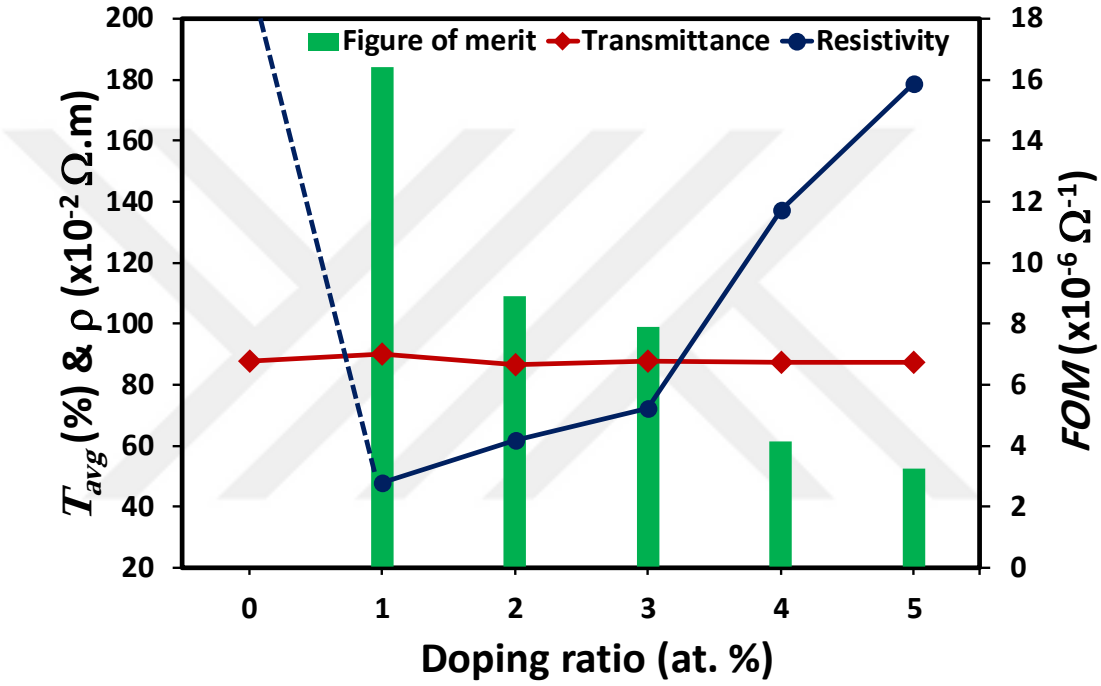


Figure 4.6: Average visible transmittance, electrical resistivity and figure of merit vs doping ratio for the AZO films.

4.1.2 Ga-doped ZnO (GZO) thin films

Through the work on the deposition of AZO thin films, the deposition process was optimized, and the obtained results were applied to develop a typical recipe for the deposition of Ga-doped ZnO (GZO) thin films (Table 3.3). GZO thin films were successfully deposited on glass substrates and their properties were investigated with altering some parameters of the deposition process. In this section, the detailed results for investigating the properties of GZO thin films under various ratios of Ga content are presented and discussed. As an original work, this section also presents the results of an experiment carried out for investigating the influence of the spin acceleration

time on the properties of GZO films. Based on the results of this experiment, a paper entitled “Influence of the spin acceleration time on the properties of ZnO:Ga thin films deposited by sol-gel method”, M. Sbeta, A. Atilgan, A. Atli, A. Yildiz, was published in the Journal of Sol-Gel Science and Technology 86 (2018) 513-520.

1- Investigation of doping ratio for GZO thin films

The properties of GZO thin films were investigated with varying the ratio of Ga content. GZO films with different Ga contents (1, 2, 3, 4, and 5 at. %) were deposited on square glass substrates. Gallium nitrate hydrate ($Ga(NO_3)_3.9H_2O$) was used as a Ga dopant precursor (DP). The ethanol solvent and MEA stabilizer were used for the synthesis of the coating solution. The concentration of ZAD in the ethanol solvent was 0.45 M/l, and the molar ratio of MEA to (ZAD + DP) was maintained at 1:1. Ten spin coating cycles were applied under the conditions; 2000 rpm spin speed for 30 sec and 10 sec spin acceleration time. The values of the other parameters of the deposition process are given in Table 3.3 and the details of the deposition process is described in section 3.1.1.1.

As shown in Table 4.3, the obtained results demonstrated that the structural, optical and electrical properties of the deposited films are significantly affected with varying the doping ratio of Ga dopant. The crystallinity of films is deteriorating with the increase in the doping ratio. For the optical and electrical properties, a turning point exists at 3 at. % of doping ratio which corresponds the best (highest) values of both the average visible transmittance and electrical conductivity. As a result, the highest (best) value of figure of merit (*FOM*) belongs to the GZO film of 3 at. % doping ratio. The high quality of the film of 3 at. % can be correlated to many parameters including texture coefficient (*TC*), lattice strain (ε), porosity (*P*) and surface roughness. Generally, carrier transport, and consequently film conductivity, is improved by maximizing grain size [75] and minimizing strain [80], porosity [81], and surface roughness [82]. As shown in Table 4-3, except the grain size, the best values of these parameters belong to the GZO film of 3 at. %. In addition, the low porosity reflects that the film has densely packed grains separated by small empty spaces which causing reduced optical scattering and leading to better transmittance for the film [4]. Generally, the different properties of the films are interrelated to each other, and any

change in the parameters related to the structural properties can affect the optical and electrical properties of the films.

Table 4.3: The estimated values of some physical parameters for the GZO films.

Parameter	GZO films				
	1 at. %	**2 at. %**	**3 at. %**	**4 at. %**	**5 at. %**
Film thickness, *d* (nm)	1067	967	1112	1161	1142
Grain size, *D* (nm)	22.8	18.4	17.8	15.9	15.8
Preferred crystal orientation	(002)	(002)	(002)	(002)	(002)
Peak intensity, *PI* of (002) plane	1879	1629	1446	1281	1036
Texture coefficient, *TC* of (002) plane	5.51	5.57	5.69	5.45	5.28
Peak intensity/*TC* of (002) plane	341	293	254	235	196
Lattice strain, ε (%)	0.1077	0.1566	0.0829	0.1993	0.3746
Refractive index, *n* [at λ = 570 nm]	1.602	1.62	1.66	1.63	1.59
Porosity, *P* (%) [at λ = 570 nm]	28.7	27.1	23.5	25.6	29.8
Surface roughness, *RMS* (nm)	8.8	4.97	4.69	4.48	8.75
Average visible transmittance, T_{avg} (%)	78.82	83.00	83.58	81.91	79.58
Optical bandgap energy, E_g (eV)	3.274	3.281	3.260	3.264	3.280
Electrical resistivity, ρ (x$10^{-2}\Omega$.m)	58.97	40.74	38.79	53.65	75.01
Figure of merit, *FOM* (x$10^{-6}\,\Omega^{-1}$)	7.6	12.7	16.0	10.9	6.7

Figure 4.7 shows the measured XRD patterns for the deposited GZO thin films which, in comparison with the standard XRD pattern of ZnO crystal (JCPDS 036-1451), confirm the formation of the hexagonal wurtzite polycrystalline structure. The curves indicate the (002) preferential orientation with the *c*-axis perpendicular to the substrate and polycrystalline nature of the films. Using the XRD data, some structural parameters were estimated for the films and their values are shown in Table 4.3. It is noticeable that the (002) peak broadens slightly and its intensity decreases as the doping ratio increases. This demonstrates that Ga dopant leads to a slight degradation n the crystal structure, and as a result, the grain size (*D*) and peak intensity decreased from 22.8 nm and 1879 a.u. to 15.8 nm and 1036 a.u. for the GZO films of 1 at. %. and 5 at. %, respectively.

A shown in Figure 4.8, the surface morphology is also affected by varying the doping ratio. Up to 4 at. % doping ratio, the film surface tends to be smoother with increasing the doping ratio then it starts to be rougher. According to the *RMS* value, the smoothest surface belongs to the films of 3 and 4 at. %.

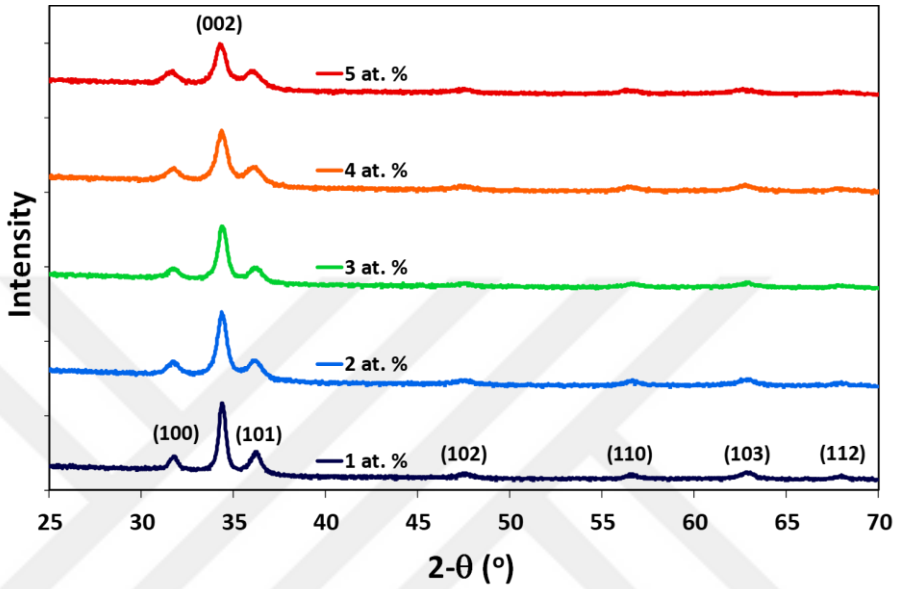


Figure 4.7: XRD patterns for the GZO films of various doping ratios

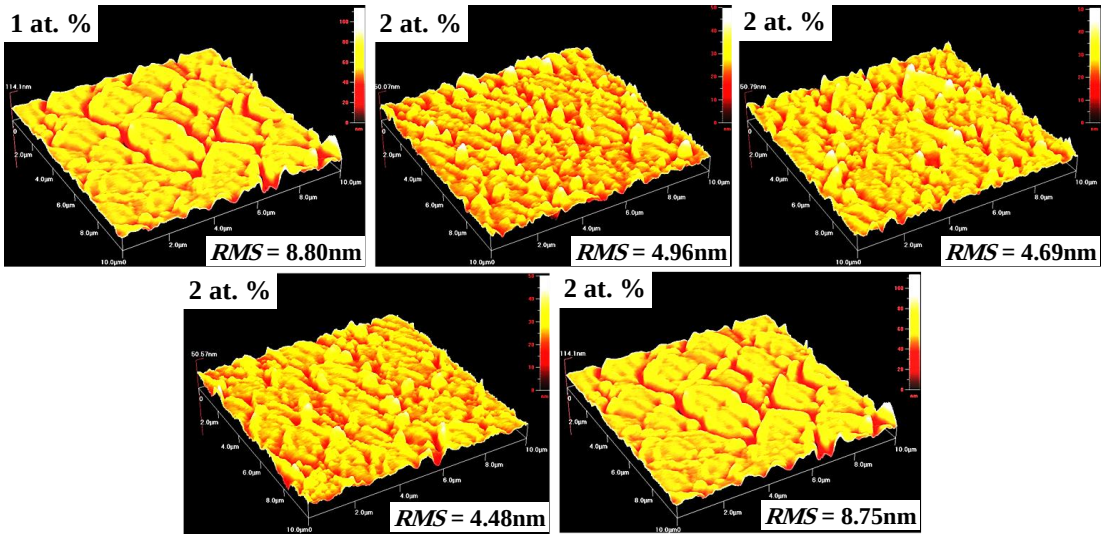


Figure 4.8: AFM images for the GZO films of various doping ratios

The transmittance spectra and the corresponding Tauc's graphs for the GZO films are shown in Figure 4.9 and it's inset, respectively. As previously reported, the presence of the interference fringes for the transmittance curves is an indicator for the smooth and uniform surface of the films. Considering their thicknesses, all the films have generally high transparency in the wavelength range from 400 to 1100 nm. Among the deposited films, the highest value of the average transmittance (83 %) belongs to the film of 3 at. % doping ratio which also has the highest value of *FOM* (Table 4.3). In addition, all the films have almost the same absorption edge at about 380 nm wavelength. As shown in Table 4.3, the estimated values of Tauc's bandgap energy (E_g) for the films have no certain trend related to the doping ratio and they are fluctuating within a small window ($\Delta E_g \cong$ 20 meV) with an average value of 3.272 eV. The largest and smallest values of E_g belong to the films of 2 and 3 at. % doping ratio, respectively. On the other hand, some kind of correlation can be recognized between E_g and film porosity (P). It seems that E_g tends to be wider for the film of higher porosity.

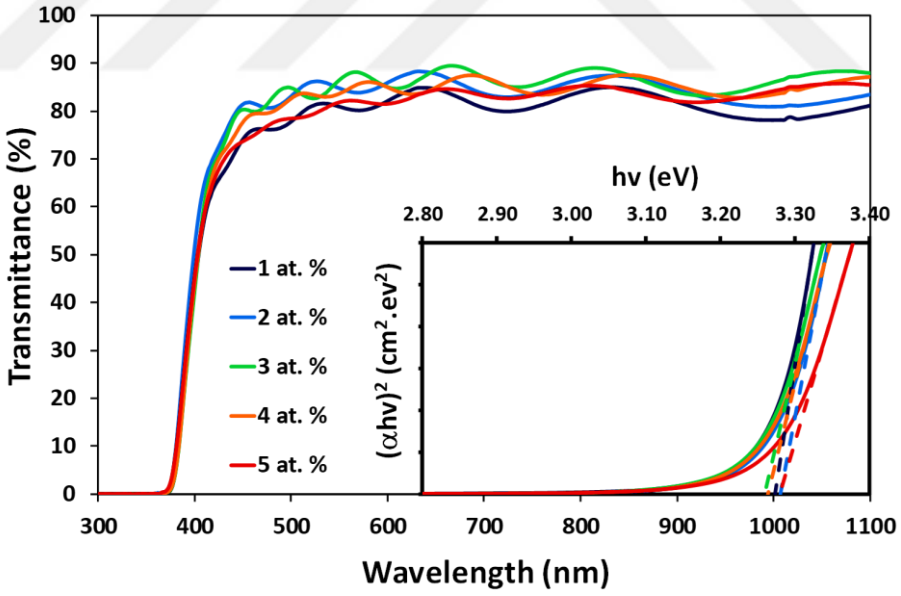


Figure 4.9: Optical transmittance spectra for the GZO films of various doping ratios, the Tauc's graph is shown in the inset.

The variation in the *FOM* for the deposited GZO films along with their average transmittance and electrical resistivity are shown in Figure 4.10. The GZO film of 3 at. % doping ratio has the highest quality since it has the highest value of *FOM*. The

values of *FOM* are generally low due to the relatively low conductivity of the films. Despite the achieved figures of the conductivity for the deposited GZO films were competitive to the published ones [8, 10], much higher figures would have been achievable by applying post-annealing process under vacuum and controlled environment. Applying such a process, the film conductivity can be significantly improved and higher *FOM* values can be achieved.

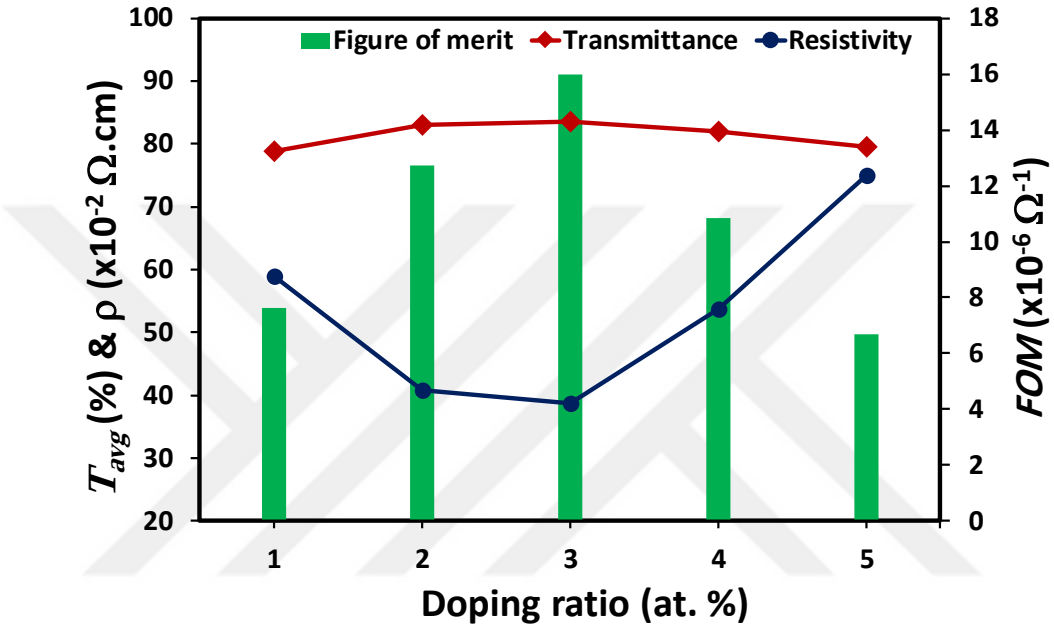


Figure 4.10: Average visible transmittance, electrical resistivity and figure of merit vs doping ratio for the GZO films.

2- Investigation of spin acceleration time for GZO thin films

This section is based on the publication “Influence of the spin acceleration time on the properties of ZnO:Ga thin films deposited by sol–gel method", M. Sbeta, A. Atilgan, A. Atli and A. Yildiz, Journal of Sol-Gel Science and Technology, 86 (2), 2018. Reproduced (or “Reproduced in part") with permission from Springer Nature. License 2019 Springer Nature Publisher.

Despite the rather good knowledge of the effect of various deposition parameters on the properties of ZnO films deposited by a spin-coating process, the effect of the spin acceleration time (t_{acc}) has not been examined. To the best of our knowledge, there is no study that has addressed various mechanisms dictating the unusual change in the properties of GZO films with varying t_{acc}. The objective of this study is to investigate

the effect of t_{acc} on the properties of GZO films deposited by a spin-coating process. The structural, morphological, optical and electrical properties of the spin-coated GZO films which are altered by varying the spin acceleration time (t_{acc}) were studied.

The GZO films were spin coated on superior quality rectangular glass substrates (ISOLAB glass) with various values of the spin acceleration time (t_{acc}). The details of the deposition process are given in section 3.1.1.1. The ethanol solvent and MEA stabilizer were used for the synthesis of the coating solution. The molarity of coating solution was 0.45 M/l, and the molar ratio of stabilizer to zinc precursor was maintained at 1:1 molar ratio. Gallium nitrate hydrate ($Ga(NO_3)_3.9H_2O$) was used as a Ga dopant precursor (*DP*) and the Ga dopant concentration ([Ga]/[Ga + Zn]) was calculated to be 2 at.%. The synthetized solution was aged for 48 h at room temperature before it was used as coating solution.

To carefully examine the effect of spin acceleration time on the properties of all the samples, they were deposited using the same solution under the same experimental conditions including the parameters of annealing and spin coating processes except for spin acceleration time. Therefore, the spin acceleration time can be considered the only variable parameter which influences all physical parameters directly or indirectly. The static dispense method was used to apply the coating solution onto the entire area of the substrate surface, then the substrate was accelerated to the final spin speed of 2000 rpm for 30 s with various spin acceleration times ($t_{acc\text{-}0}$ = 0, $t_{acc\text{-}2}$ = 2, $t_{acc\text{-}4}$ = 4, $t_{acc\text{-}6}$ = 6, $t_{acc\text{-}8}$ = 8 and $t_{acc\text{-}10}$ = 10 s). In order to avoid the differences in film quality, and have a fair comparison, only small area (0.5 x 0.5 cm^2) at the center of the coated substrate (2.5 x 2.5 cm^2) was considered to analyze properties of the deposited films.

The obtained results showed that, by varying t_{acc}, there is no significant variation in crystal size, and band gap energy of the films, while some physical parameters such as strain (ε), surface roughness (RMS), and porosity (P) are remarkably varied. By increasing t_{acc} from 0 to 8s, ε, RMS, and P, were increased by 230 %, 83 %, and 49 %, respectively. The variation in the film resistivity (ρ) was unambiguously figured out to be closely connected to the change in these parameters. To explain these findings, a simple formula was proposed in the investigated range of t_{acc}, which demonstrated that

ρ is more related to ε and P, and then to RMS. The measured and estimated parameters for the films with varying t_{acc} are summarized in Table 4.4.

The measured XRD patterns shown in Figure 4.11 reveal the polycrystalline structure of the films. In comparison with the standard XRD pattern of ZnO crystal (JCPDS 036-1451), the films are confirmed to show the formation of a hexagonal wurtzite structure that belongs to the ZnO material. In addition to the (100), (101), (102), (110) and (103) planes, all the films exhibit highly preferred crystal orientation corresponding to (002) plane along the *c*-axis perpendicular to the surface of the glass substrate. The (002) peak is dominant for the all films, and only a weak trace of other peaks exists. The texture dominance of (002) plane of films is evaluated by texture coefficient (*TC*) and their values are shown in Table 4.4. The calculated *TC* values vary between 5.1 and 5.58. The relatively strong and sharp intensity, high texture coefficient and low full width at half maximum (FWHM) intensity of the (002) peak indicates that the films exhibit a good crystalline quality.

Table 4.4: Some physical parameters of GZO films with varying spin acceleration time.

Parameters	$t_{acc\text{-}0}$	$t_{acc\text{-}2}$	$t_{acc\text{-}4}$	$t_{acc\text{-}6}$	$t_{acc\text{-}8}$	$t_{acc\text{-}10}$
Film thickness, *d* (nm)	465±11	470±10	531±6	678±7	752±6	662±5
Texture coefficient, *TC*	5.36	5.25	5.58	5.24	5.10	5.15
Lattice constant, *a* (nm)	0.3254	0.3253	0.3255	0.3252	0.3257	0.3263
Lattice constant, *c* (nm)	0.5207	0.5210	0.5208	0.5209	0.5213	0.5218
Grain size, *D* (nm)	21	20	20	21	19	20
Crystal strain, ε (%)	0.047	0.088	0.064	0.080	0.157	0.244
Surface roughness, *RMS* (nm)	1.8	2.4	1.6	1.9	3.3	2.1
Average transmittance, T_{av} (%)	88.3	87.2	87.6	86.3	86.2	88.4
Refractive index, *n* [at 550 nm]	1.76	1.77	1.75	1.72	1.68	1.71
Porosity, *P* (%)	14.5	13.6	14.9	17.9	21.6	18.5
Sheet resistance, R_{sh} (kΩ/□)	17.61	26.13	19.86	20.47	24.05	28.81

The lattice constants *a* and *c* are estimated using Equation 3.9 and their values are shown in Table 4.4. The ratio of c/a is about 1.6, confirming again the hexagonal crystal structure of the films. As shown in the inset of Figure 4.11, the (002) peaks of the films are shifted to lower angles as compared to that of bulk ZnO (c_0 = 0.5205 nm), indicating the increment of lattice parameter c. Apparently, the *c* parameter first increases with increasing t_{acc}, then it decreases with a value greater than the initial

value, but it continues to increase with increasing t_{acc} (Table 4.4). This in turn causes a disorder effect of the lattice with varying t_{acc}. The grain sizes (D) of the films are obtained by means of Scherer's equation utilizing the FWHM of (002) peak of the films. The strain (ε) in the films is defined by Equation 3.12 .The estimated results are summarized in Table 4.4. Generally, all structural parameters estimated for the films are in good agreement with those previously published on GZO films with 2 at. % of Ga [107-109]. The obtained results showed that the value of D of the films remains almost constant with varying t_{acc}. However, a significant change in the strain values with varying t_{acc} occurs. The lowest strain (%) of 0.047 belongs to the film deposited at $t_{acc\text{-}0}$, while it increases further to 0.244 for the film deposited at $t_{acc\text{-}10}$. The positive value of strain indicates the tensile strain for the films. In our case, strain increment is not accompanied by a decrease in crystallinity. The strain might be due to the different ionic size of Zn^{2+} and Ga^{3+}. A small lattice distortion is expected for GZO films due to the similar tetrahedral radii of Zn^{2+} and Ga^{3+} [85]. However, it is not the same for all films despite their same dopant ratio of 2 at. %. Compared with literature [70, 83-87], the obtained remarkable low tensile strain values confirm the high-quality crystal structure of the films. It also indicates that less disorder in the lattice occurs in the GZO films at lower values of t_{acc} (from $t_{acc\text{-}0}$ to $t_{acc\text{-}6}$) during the deposition process.

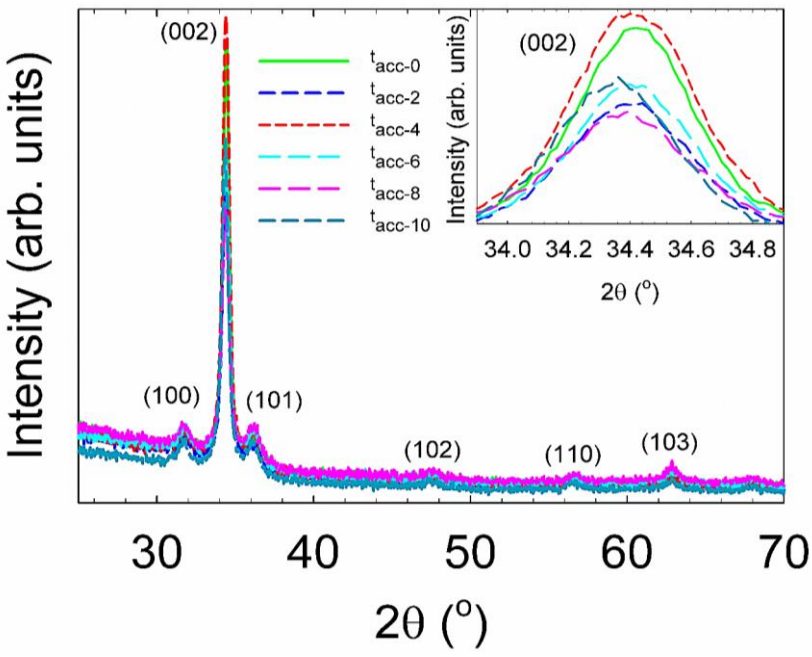


Figure 4.11: X-ray diffraction patterns for GZO films deposited at different spin acceleration time. Inset shows an enlarge (002) peak of the films.

Figure 4.12 shows the AFM images of the films. The surface of the films is seen to be very smooth and uniform. Table 4.4 lists the surface root mean square (RMS) roughness values of the films. The value of RMS is also found to be dependent on t_{acc}. It shows that the film deposited at $t_{acc\text{-}4}$ exhibits the lowest RMS value of 1.6 nm among the others. That result is in good agreement with XRD measurement results. The variation of RMS with t_{acc} observed for the films might be correlated to an enhancement in the intensity of the (002) peak. The highest (002) peak belongs to the film deposited at $t_{acc\text{-}4}$ which is accompanied by the lowest *RMS* value. The descending order of (002) peak intensity is $t_{acc\text{-}4}$, $t_{acc\text{-}0}$, $t_{acc\text{-}10}$, $t_{acc\text{-}6}$, $t_{acc\text{-}2}$ *and* $t_{acc\text{-}8}$, while the ascending order of *RMS* values is $t_{acc\text{-}4}$, $t_{acc\text{-}0}$, $t_{acc\text{-}6}$, $t_{acc\text{-}10}$, $t_{acc\text{-}2}$ and $t_{acc\text{-}8}$. This result demonstrates that variation of t_{acc} allows us to simultaneously control both morphological and structural properties.

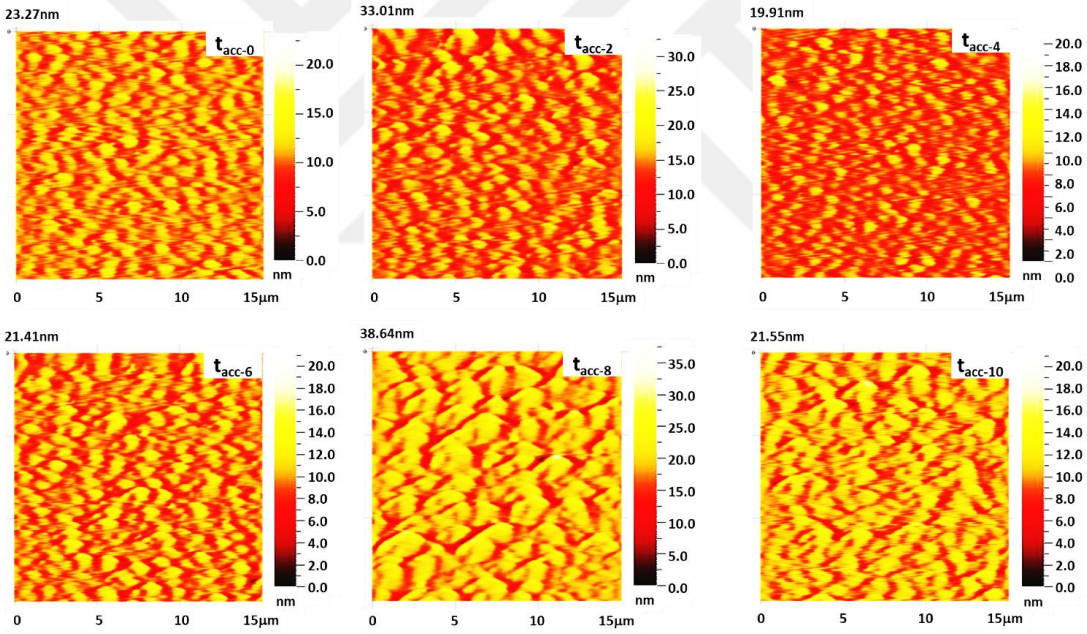


Figure 4.12: The two-dimensional AFM micrographs (15 × 15 µm) for the GZO films with different spin acceleration time, as indicated inside the pictures.

Figure 4.13 displays the SEM images of the films. The images depict that a slight change in morphology of the films occurs with varying t_{acc}. The morphology of the films has densely packed grains separated by small empty spaces. The grain sizes were found to be in the range of 36-38 nm, which are greater than those estimated from XRD data. This discrepancy is attributed to the fact that the broadening of the x-ray

diffraction beak is affected, in addition to the grain size, by other factors such as lattice strain and instrumental effect. These factors are neglected in Scherrer's formula which assumes that the broadening is only affected by the grain size. Similar observations were reported by Bandyopadhyay *et al.* [88] for ZnO films. Despite this difference in grain size values based on XRD and SEM measurements, still the values of grain size estimated from SEM are very close to each other, demonstrating that grain size of the films is insensitive to variation in t_{acc}.

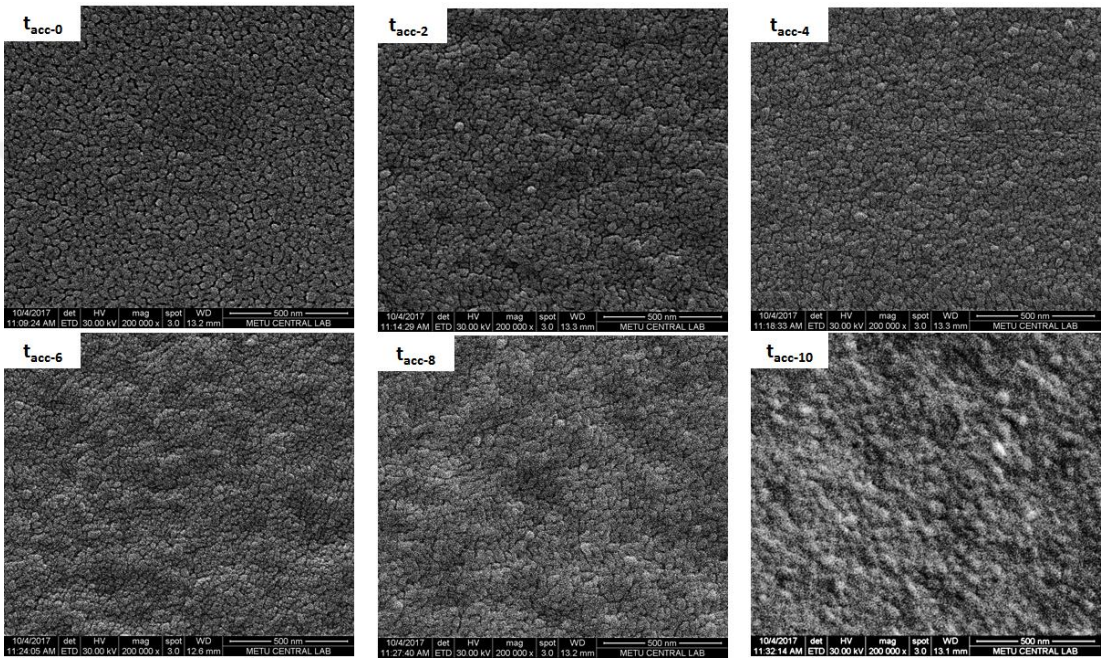


Figure 4.13: SEM micrographs of GZO films at various spin acceleration time, as indicated inside the pictures.

The measured optical transmittance spectra for the films are shown in Figure 4.14. The transmittance spectra exhibit a sharp drop at about 400 nm wavelength (in the UV region) due to the sharp absorption edge of the films. All the films show a good transmittance above the 400 nm wavelength with an average transmittance above 86% in the wavelength range from 400 to 800 nm (Table 4.4). There is a little fluctuation in the transmittance with varying t_{acc}. The transmittance can be associated with the values of grain size, *RMS*, porosity and thickness of the films. It is generally expected that increased thickness and surface roughness lead to reduced transmittance, while increasing porosity and grain size increase transmittance [15, 20]. In our case, the grain size with varying t_{acc} remains almost the same. Therefore, we rule out its impact on

the transmittance. To explain the trend in the transmittance values, we consider three competing factors which are *RMS*, porosity and thickness of the films. While the lowest transmittance value is found in the film deposited at $t_{acc\text{-}8}$, nearly equal highest values are observed for the films deposited at $t_{acc\text{-}0}$ and $t_{acc\text{-}10}$. The film deposited at $t_{acc\text{-}8}$ is the thickest of them, leading to low transmittance. Comparing the films deposited at $t_{acc\text{-}0}$ and $t_{acc\text{-}10}$, the film at $t_{acc\text{-}0}$ is relatively thinner, less rough, but less porous, while the film deposited at $t_{acc\text{-}10}$ is slightly thicker, rougher, but more porous. These might be reasons why the transmittance values of these two films are very close to each other.

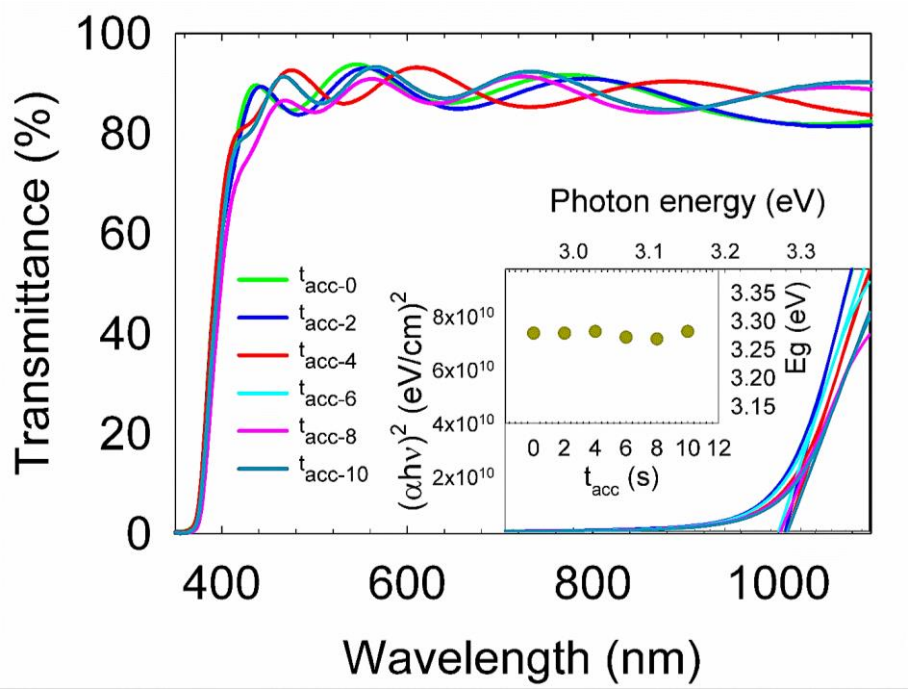


Figure 4.14: Optical transmittance of GZO films as a function of wavelength. $(\alpha h\nu)^2$ as a function of photon energy hν, and the band gap as a function of spin acceleration time are shown in the inset.

Another important observation from Figure 4.14 is the presence of well-defined interference fringe patterns for the films, indicating high optical quality of the films with their smooth surfaces [89, 90]. This behavior also allows us to extract some parameters such as film thickness (d) and optical refractive index ($n(\lambda)$). Based on the transmission interference fringes, the Swanepoel method described in section described in section 3.1.2 is applied to estimate d and $n(\lambda)$.

The estimated values of d and n (λ) of the films are shown in Table 4.4. By increasing t_{acc} from $t_{acc\text{-}0}$ to $t_{acc\text{-}8}$, the films thickness increases from 465 to 752 nm, respectively. On other hand, a further increase in t_{acc} causes the thickness to decrease again. It was reported that the change in viscosity of the coating solutions causes a change in the thickness of ZnO thin films [70]. In our case, the same coating solution was used for all films. However, the solvent evaporation of the dispensed solution can occur during the spin coating process. Since the dispensed solution starts to dry during the first part of the spin coating process, longer spin acceleration time leads to a higher solvent loss in the dispensed solution before the spin process reaches its final (maximum) speed, and consequently a solution of higher viscosity will be spun leading to a thicker coated film [91].

The noticeable changes in both d and $n(\lambda)$ with varying t_{acc} can be also due to variation in porosity (P). The variation in the thickness and porosity of the films as a function of $t_{acc.}$ is shown in Figure 4.15. The estimated value of n at 550 nm wavelength is used to calculate P using Equation 3.23 described in section 3.1.2 ($n_{bulk} = 1.944$ at 550 nm is used [92]). It is evident that as the t_{acc} increases, porosity and thickness almost exhibit the same trend, reaching a maximum value at $t_{acc\text{-}8}$ (Figure 4.15). Further increase in t_{acc} leads to a decrease in the both parameters. Therefore, the variation of thickness with t_{acc} is not only related to viscosity, the effect of porosity should be considered as well. This can explain why the thickness reduces at $t_{acc\text{-}10}$.

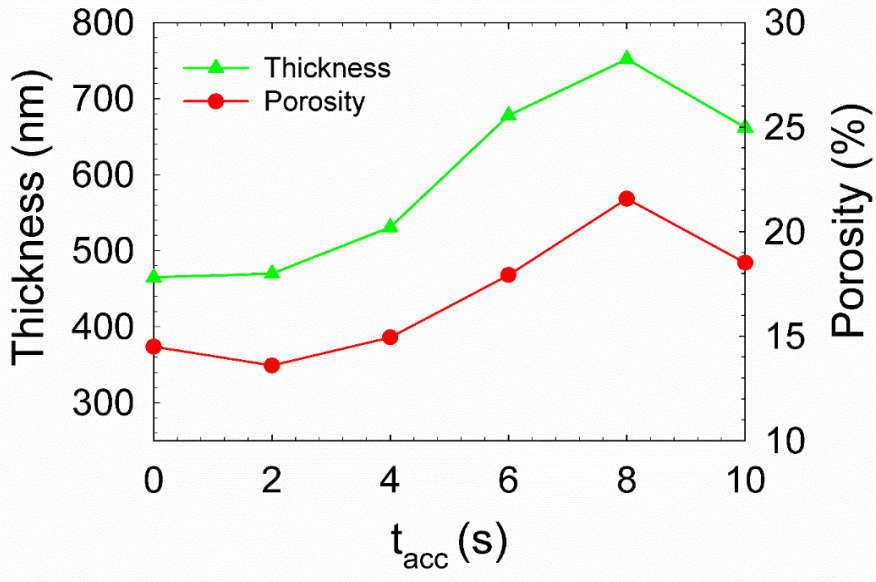


Figure 4.15: Dependence of the thickness and the porosity on spin acceleration time for GZO films.

The impact of $t_{acc.}$ on the band gap (E_g) was also investigated. E_g as a function of t_{acc} is shown in the inset of Figure 4.14. The measured transmittance spectrum along with the estimated thickness are used to estimate the E_g for the films by implementing Tauc's model described in section 3.1.2. The estimated value of E_g for the films is about 3.28 eV, which is close to that of GZO films [70]. From the inset of Figure 4.14, it seems that t_{acc} does not contribute any significant changes to E_g of the films. Plausible explanations on variation of E_g in ZnO films can be found in the literature [20, 92]. It is reported that the change in E_g for ZnO films is due to either the change in grain size or in dopant ratio [20, 92]. Since grain size is almost t_{acc} independent and the films have the same dopant ratio, this is reasonable considering that varying t_{acc} causes very little variation in the E_g of the films.

The dependency of resistivity (ρ) on t_{acc} is illustrated in Figure 4.16. The observed values of ρ agree well with the values reported on GZO films with 2 at. % of Ga [70, 83]. From Figure 4.16, it is obvious that three different regions can be distinguished. In the first region (from $t_{acc\text{-}0}$ to $t_{acc\text{-}4}$), ρ increases slowly with t_{acc}, but in the second region (from $t_{acc\text{-}4}$ to $t_{acc\text{-}8}$), it increases remarkably. Finally, it becomes weakly dependent on t_{acc} in the third region (from $t_{acc\text{-}8}$ to $t_{acc\text{-}10}$).

It is known that the resistivity of ZnO generally tends to be decreased by the film thickness because of its direct dependency on the grain size, which usually increases with film thickness [77]. This scenario does not work for our films. Contrary to the expectations, in our case, the resistivity of the films increases with thickness (Table 4.4). Therefore, we should consider other parameters affecting resistivity such as grain size, strain, porosity, and surface roughness. Generally, carrier transport, and consequently film conductivity, is improved by maximizing grain size [80] and minimizing strain [75], porosity [81], and surface roughness [82]. In our case, the effect of grain size on resistivity can be ignored, and the resistivity can be analyzed by considering the other three parameters. We propose here a formula for estimation of resistivity as a function of strain, porosity, and surface roughness over the investigated range of t_{acc}. To avoid the specifics and combine the effect of all these parameters, the normalized measured data of these parameters are used to estimate the film resistivity as follows:

$$\rho_e = \rho_{m_max}\, \rho_{e_norm} \tag{9}$$

and

$$\rho_{e_norm} = SF\left[c_1 \boldsymbol{\varepsilon}_{m_norm} + c_2 P_{m_norm} + c_3 RMS_{m_norm}\right] \tag{10}$$

where ρ_e, ρ_{e_norm}, and ρ_{m_max} are the estimated resistivity, normalized estimated resistivity, and maximum value of measured resistivity, respectively. $\boldsymbol{\varepsilon}_{m_norm}$, P_{m_norm}, and RMS_{m_norm} are normalized measured strain, porosity, and surface roughness, respectively, relative to their maximum values. SF is a scale factor, and c_1, c_2, and c_3 are weight constants of strain, porosity, and surface roughness, respectively. The weights of constants are optimized in such a way that a minimum value is obtained for the standard deviation of the curve that represents the difference between the measured and the estimated resistivity curves. Under this criterion, the optimum values are 0.4, 0.4, and 0.2, for c_1, c_2, and c_3, respectively, and the value of SF is 1.15. Note that the standard deviation is 0.07. Figure 4.16 makes a comparison between the measured and estimated resistivity curves. A good match between the two curves indicates that the proposed formula holds, to clarify the contribution of the considered parameters in determining the films' resistivity over the investigated range of t_{acc}. Therefore, the analysis strongly suggests that the film resistivity is primarily more related to strain and porosity, and then to surface roughness.

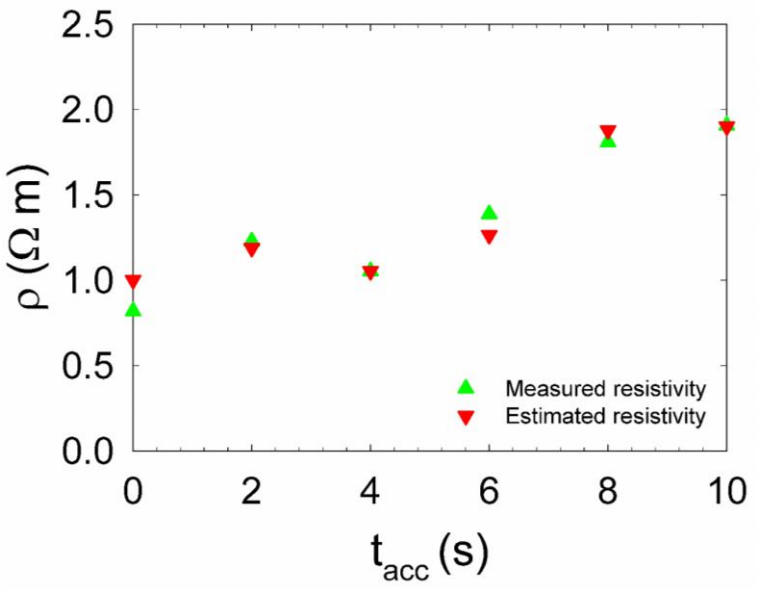


Figure 4.16: Resistivity of GZO films with various spin acceleration time.

4.2 GZO/p-Si heterojunction-based devices

4.2.1 Basic structure device

n-GZO/p-Si heterojunctions were successfully formed by the deposition of sol-gel derived n-GZO thin film on p-Si substrate. The n-GZO/p-Si heterojunction-based devices of basic structure (Figure 3.15-a) were fabricated and optimized. The details of the fabrication process of devices are explained in section 2.4.3. The fabricated devices were optimized in terms of the GZO layer parameters, the metallization of front and back sides, the specifications and cleaning process of Si wafers and the sequence of fabrication steps. Although all these aspects are crucial in determining the performance of device, the quality and specifications of GZO layer represent the most crucial issue. The best results obtained for the investigated parameters of GZO layer and fabrication process of the device are shown in Table 4.5.

Table 4.5: The investigated parameters and their best results for GZO/p-Si devices.

Fabrication step	Parameters	Variables	Result of highest performance
GZO layer	Thickness	**Spin coating cycles*:** 1, 2, 3, 4, 5	1 and 2
	Doping ratio	**Content of Ga (at. %):** 0, 2, 3	3
	Crystallinity	**Solvent-stabilizer combination:** ▪ Ethanol-MEA ▪ 2-methoxyethanol-MEA ▪ 2-methoxyethanol-DEA	Ethanol-MEA
Back metallization	Material	**Metallization paste:** ▪ Ag paste ▪ Al paste	Al paste
Cleaning of Si wafer	Removal of contamination	**Cleaning sequence:** ▪ Only Piranha ▪ Only RCA ▪ Piranha + RCA	Only Piranha
Sequence of fabrication steps	GZO coating vs back metallization	**Applied sequence:** ▪ GZO then back metallization ▪ Back metallization then GZO	Back metallization then GZO coating
p-Si wafer	Thickness and resistivity	▪ 525 μm, 1-20 Ω.cm ▪ 380 μm, 1-10 Ω.cm	525 μm, 1-20 Ω.cm

*The deposition rate is ~40 nm/cycle

The best results for the investigated parameters are the results associated with the highest performance obtained for the fabricated devices as a solar cell and a photodiode. The device performance was mainly judged through the *I-V* characteristics measured in the dark and under illumination condition. The illuminated *I-V* characteristics were measured under AM1.5 illumination of 100 mW/cm^2 intensity and 254±80 nm UV illumination of 1.85 mW/cm^2 intensity.

As explained in section 2.4.1, deposition of thin (~0.1 μm) and highly conductive n-ZnO film onto Si is required when fabricating a solar cell. With compromising between the thickness and conductivity, GZO film can act as both an active layer and antireflection coating layer. As shown in Figure 4.17a, the highest measured conductivity for our deposited GZO thin films corresponds the doping ratio of 3 at. %. As stated in Table 4.5, the best result for the device was obtained with the same value of doping ratio for GZO film. Although the achieved conductivity of our GZO films is competitive to that in literature [8, 10], higher conductivity is required to provide both wider extension for the depletion region in Si side (higher photocurrent) and lower series resistance for the device.

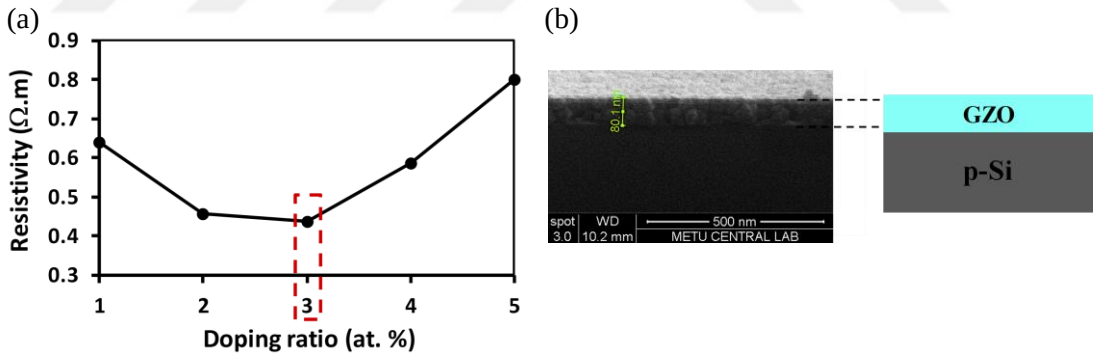


Figure 4.17: Electrical resistivity vs doping ratio of GZO films (a), cross-sectional SEM image for two cycles spin-coated GZO film on Si substrate (b).

Regarding the thickness of GZO layer, better performance was obtained for the devices of thinner GZO films deposited using one or two cycles of spin coating. This result complies with the requirements since the thin deposition of GZO can facilitate the collection of carriers at the front electrode and maximize the absorption of light in the Si. A thickness of about 80 nm for GZO films was achieved with applying two coating cycles as determined from cross-sectional scanning electron microscopy (SEM) image

(Figure 4.17b). For antireflection coating of Si substrate, the ideal refractive index value for the coating film is ~2 at 550 nm and the corresponding thickness is ~70 nm. The refractive index and thickness of antireflection coating film are derived from the relations [66]; $n_a = \sqrt{n_0 n_s}$ and $t_a = {}^{\lambda}/_{4n_a}$,respectively, where n_a and t_a are the refractive index and thickness of the antireflection coating film and n_0 (~ 1) and $n_s (\sim 4\ at\ 550\ nm)$ are the refractive indices of air and Si substrate, respectively. Considering that our deposited GZO films have a refractive index of ~1.75 (see Table 4.4), the thickness of ~80 nm for GZO layer can be close to the antireflection coating requirements.

Referring to section 4.1.1, it was showed that the quality of ZnO films in terms of their structural, electrical and optical properties are affected by the type of solvent-stabilizer combination. By comparing the combinations of ethanol-MEA, 2-methoxyethanol-MEA and 2-methoxyethanol-DEA, the films of ethanol-MEA combination exhibited the best crystallinity and highest conductivity and transparency (Figure 4.1 and Table 4.1). The preference of ethanol-MEA combination for preparing the GZO films was confirmed for the devices too. As stated in Table 4.5, among the investigated combination of solvents and stabilizers, the best result was obtained for the device of GZO film prepared using the ethanol-MEA combination.

The sequence of fabrication steps can also affect the device performance. Better result was obtained with carrying out the step of back metallization before the step of spin coating of GZO film (Figure 3.16). This result can be attributed to that a thin native SiO_2 layer could be unintentionally grown on the front side of Si substrate during the process of back metallization. The GZO layer will then in fact be deposited on SiO_2-coated Si substrate, i.e. an interlayer of SiO_2 will exist between the GZO layer and Si substrate, and the actual structure of our device is Ag/n-GZO/SiO_2/p-Si/Al. The SiO_2 interlayer can cause a significant reduction of interface defect states [127] leading to lower interface recombination of photogenerated carriers. D. G. Baik et. al [93] reported that insertion of 1 nm thick SiO_2 between ZnO and Si helped to increase the short-circuit current for n^+-ZnO/n-Si junction solar cell.

Two types of p-Si (boron-doped) substrates were used for fabricating the devices. One type is 525 μm thick and 1-20 Ω.cm resistivity, and other type is 380 μm thick and 1-

10 Ω.cm resistivity. The devices fabricated using the Si substrate of 525 μm thick exhibited better performance than those fabricated using the substrate of 380 μm thick. This result could be attributed to the difference in the bulk resistivity for the two substrates. As explained in section 2.4.1, it is required that the depletion region be more extended into p-Si side. For achieving this requirement, less doped p-Si substrate is preferred. The p-Si substrate of 525 μm thick can be assumed to be less doped since it has higher average resistivity compared to the other substrate of 380 mm thick. This reason could be behind the advantage of the 525 μm thick substrate over the 380 μm substrate. Hereafter, the detailed results of the optimized device are presented and discussed.

The measured XRD pattern for the GZO film deposited on p-Si substrate is shown in Figure 4.18. The results reveal the polycrystalline structure of the film with XRD pattern matches that of the standard XRD pattern of ZnO crystal (JCPDS 036-1451) confirming the formation of the hexagonal wurtzite structure of ZnO material with diffraction peaks marked in the figure.

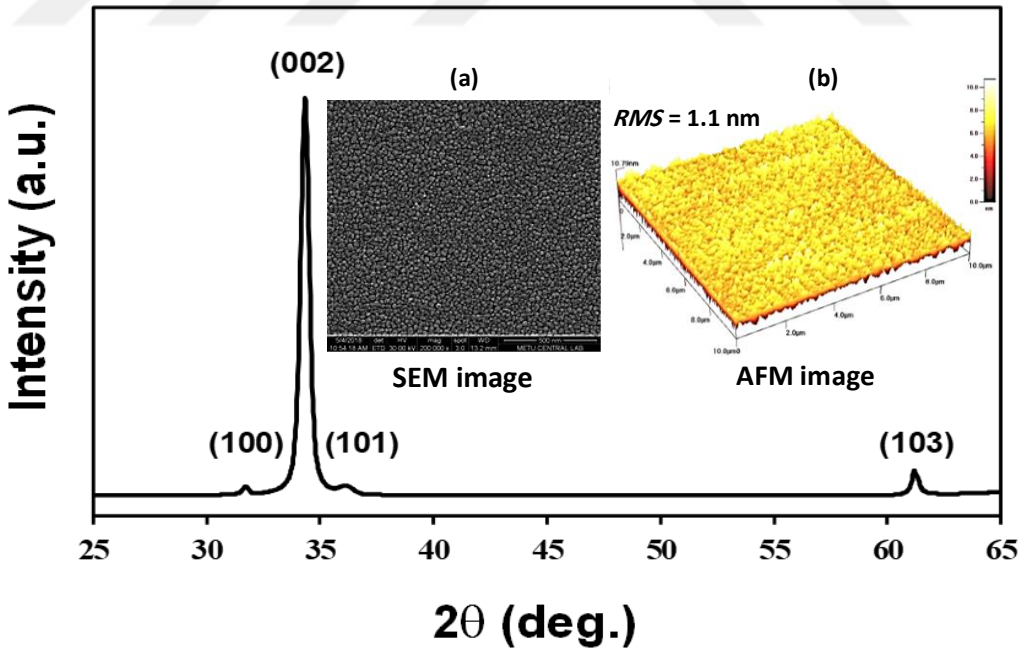


Figure 4.18: The measured XRD pattern for the GZO film deposited on Si substrates. The insets are the surface SEM (a) and AFM (b) images for the film.

The insets of Figure 4.18 depict the surface SEM and AFM images of the GZO film. The SEM images showed that the film has a uniform microstructure with densely packed grains separated by small empty spaces, and the AFM image showed the very smooth surface of the film. Some of the estimated parameters of the structural properties for the GZO layer are shown in Table 4.6.

The measured optical transmittance spectrum for GZO film deposited on glass substrate is shown in Figure 2.19. The transmittance spectrum exhibits a sharp drop at about 380 nm wavelength (in the UV region) due to the sharp absorption edge of the films. Above the 380 nm wavelength, the film has a good transmittance with an average value of about 84.5 % in the wavelength range from 380 to 1100 nm. The optical bandgap energy (E_g) of GZO film is estimated by implementing Tauc's model using the measured transmittance data. From Tauc's plot (the inset of Figure 4.19), the estimated value of E_g was about 3.27 eV which is close to that of GZO films [83]. According to E_g value of GZO film, only the wavelengths below 380 nm of the incident light can be absorbed by GZO layer, while the wavelengths above 380 nm will transmit through GZO film and can be absorbed by Si substrate.

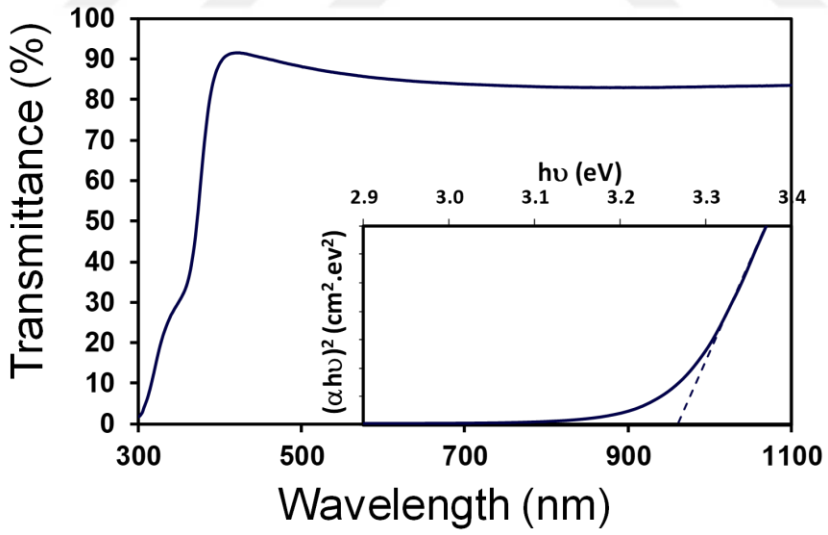


Figure 4.19: The measured transmittance spectrum for the GZO film deposited on glass substrate. The inset is Tauc's plot for the film.

Furthermore, the absorption penetration depth as a function of wavelength, $d_a(\lambda) = 1/\alpha(\lambda)$ was evaluated to determine the wavelength absorption limits by considering the thickness of GZO layer and the depletion region width in p-Si side (W_{Si} = 0.34 μm

typically for n-ZnO/p-Si [130]). $\alpha(\lambda)$ of Si material [96] was considered in the calculations. The wavelengths λ = 365 nm (corresponding to $d_a(\lambda)$ = 79.7 nm) and λ = 468 nm (corresponding to $d_a(\lambda)$ = 0.338 μm) were considered as the wavelength absorption limits $\lambda_{t,GZO}$ and $\lambda_{t,Si}$ for GZO layer and p-Si substrate, respectively. Therefore, the incident light of $\lambda < \lambda_{t,GZO}$ can directly be absorbed by GZO layer and the light of $\lambda_{t,GZO} < \lambda < \lambda_{t,Si}$ can be absorbed within W_{Si} and they can highly contribute to photocurrent. The light of $\lambda > \lambda_{t,Si}$ is absorbed out of W_{Si}, and accordingly, its contribution to photocurrent decreases exponentially as λ increases.

Table 4.6: Some physical parameters of GZO layer of GZO/p-Si device.

Parameter	Value
Thickness, *d* (nm)	~80
Grain size, *D* (nm)	31.5
Surface roughness, *RMS* (nm)	1.1
Refractive index, n [at 550nm]	1.75
Porosity, *P* (%)	13.5
Average transmittance, T_{av} (%) [380-1100nm]	84.5
Optical bandgap energy, E_g (eV)	3.27
Resistivity ($x10^{-2}\Omega$.m)	38
Carrier concentration (cm^{-3})	$8.1x10^{18}$

Figure 2.20 shows the semi-log plot of the measured current-voltage (*I–V*) characteristics in the dark and under AM1.5 and UV illumination for the device. As shown in Figure 2.20b, in the dark, the device clearly exhibits diode behavior with an excellent rectification capability and low saturation current. The dark *I-V* characteristics of device can be formulated using the general diode equation 3.30. The diode parameters including rectification ratio, *RR* at ± 3V, light to dark forward currents, *LDFC* at 3V, the saturation current, I_o, ideality factor, *n*, and height of zero bias barrier, ϕ_{bo}, were calculated adapting the formulas given in section 2.4.4. The obtained values for these parameters are listed in Table 4.7. The low value of I_o is an indicator to the low diffusive of minority carriers and low leakage of surface current [64]. The estimated values of *n* are higher than 2 for the all devices which reveal the

nonideal diode behavior and the dominancy of leakage current mechanism [97]. Generally, the deviation from ideal behavior is inherent for the p-n heterojunction-based diodes. Similar figures and even higher of ideality factor for ZnO/Si heterojunction-based diodes were reported by the others [61, 98-100].

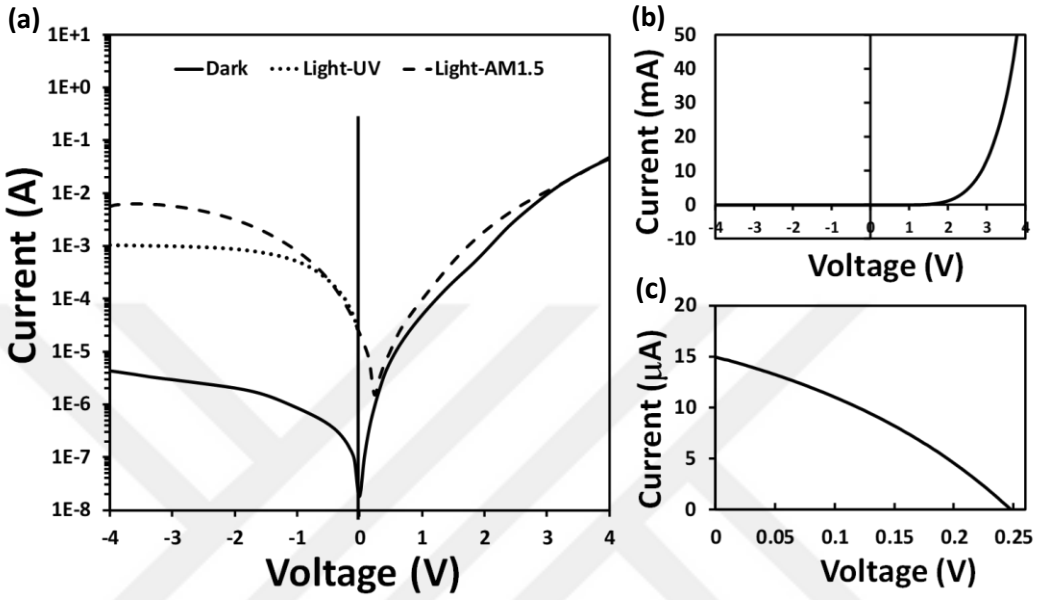


Figure 4.20: Semi-log *I-V* characteristics in the dark and under the illumination of AM1.5 and UV (reverse bias region only) (a), linear *I-V* characteristics in the dark (b), and the PV characteristics under AM1.5 illumination (c) for the device.

Table 4.7: GZO/p-Si diode parameters in the dark

Parameter	Value
Rectification ratio, *RR* x10^3 [at ±3 V]	8.74
Light to dark forward currents, *LDFC* [at 3V]	1.08
Reverse saturation current, I_o (nA)	35.69
Ideality factor, *n*	2.84
Zero bias barrier potential, ϕ_{bo} (V)	0.810

As shown in Figure 4.20a, under the illumination conditions, the device generally exhibits high optical response. The photosensitivity, *PS* and photoresponsivity, *PR* defined in Equations 3.34 and 3.35 were used as measures for the device sensitivity to light. Under UV illumination, the average *PS* and *PR* values at -3 V were 952 and 0.54 A/W, respectively. Under AM1.5 illumination, the values were 5.995x10^3 and 0.12 A/W for *PS* and *PR*, respectively. The achieved values for these two measures are

higher than the best data reported so far for the ZnO/Si based p-n junction devices [30, 100-106]. By considering the difference in the intensity of the used UV light (1.85 mW/cm^2) and the AM1.5 (100 mW/cm^2) light, we figure out that the device is more sensitivity to UV light. This result is anticipated since the UV spectrum can be fully absorbed by the device (within the depletion region) providing high contribution to photocurrent. Furthermore, one can recognize from Figure 4.20a that the reverse current under UV illumination reaches its almost maximum value at lower reverse voltage value compared to that under AM1.5 illumination (i.e. under UV illumination, the reverse current is less sensitive to the increase in the reverse voltage). This could be attributed to that wider depletion region is required for the light of longer wavelength to be absorbed within this region and contribute efficiently to photocurrent. This requirement can be achieved at relatively higher reverse voltage value in case of AM1.5 illumination.

Figure 4.20c shows the photovoltaic (PV) *I-V* characteristics for the device. The obtained values for the open circuit voltage, V_{oc} and the short circuit current, I_{sc} were 250 mV and 15 μA, respectively. It is obvious from the figure that the device exhibits low performance of PV property which could be attributed mainly to the following factors; First, the series resistance, R_s of the device is high (the estimated value was 30.8 kΩ) which could be related to the high sheet resistance of GZO layer itself and the wide gridline spacing of front contact. Second, the recombination rate of the photogenerated carriers could be high for many reasons including the GZO/Si heterojunction interface traps due to the lattice mismatch, bulk recombination in GZO layer due to its porous and polycrystalline microstructure, and top surface recombination due to the absence of surface passivation layer.

4.2.2 Metal NPs-coated devices

This section is based in part on the publication “Optical Response Enhancement of GZO/p-Si Heterostructures via Metal Nanoparticles", M. Sbeta and A. Yildiz, Journal of Material Research Express, 2019. Reproduced (or “Reproduced in part") with permission from IOP Publishing 2019.

Metal nanoparticles (NPs) were incorporated into the basic structure of the n-ZnO/p-Si heterojunction-based devices to investigate the possible improvement in the device

performance through enhancing its optical response. The schematic diagram of the fabricated metal NPs-coated devices is shown in Figure 3.15-b. The solution-processed metal NPs are spin coated on the top of GZO layer before metallization. The investigated metal NPs include 100 nm Au NPs (dispersed in Phosphate Buffered Saline (PBS), Sigma-Aldrich, no: 753688) and 100 nm Ag NPs (dispersed in aqueous buffer contains sodium citrate as stabilizer, Sigma-Aldrich, no: 730777). Using metal NPs, the light can be scattered and trapped via the surface plasmon resonance effect. The plasmonic effect of the metal NPs allows for additional scattering at the top surface thus reducing the overall reflectivity and injecting more light into the device leading to higher optical response [33]. The metal NPs-coated devices were fabricated under the same conditions and specifications that were applied for the fabrication of the optimized device of basic structure (denoted here as bare device and used as a reference to judge the performance of metal NPs-coated devices).

The obtained results showed that the inclusion of metal NPs into the devices led to improved optical absorption and consequently increased the performance of the devices in terms of photoelectric properties. Generally, higher performance was demonstrated by the Ag NPs-coated device. The devices were highly sensitive to UV illumination. Photoresponsivity (*PR*) of 0.73 A/W at -3V was exhibited by the Ag NPs-coated device against 0.60 and 0.54 A/W for the Au NPs-coated and without NPs (bare) devices, respectively. The devices also demonstrated a photovoltaic (*PV*) behavior under AM1.5 illumination. Compared to the bare device, significant improvement of 167.3 % in the short circuit current (I_{sc}) and 83.1 % in the *PV* conversion efficiency were obtained with Ag NPs-coated device.

Figure 4.21 presents the measured absorbance spectra for the metal NPs-contained dispersions along with the solar radiation spectrum of AM1.5 distribution. The results show the existence of absorbance peaks at 481 nm with 180 nm full width at half maximum (FWHM) and 568 nm with 88 nm FWHM for the Ag NPs and Au NPs, respectively. The Ag NPs have an absorbance peak of wider bandwidth centered at shorter wavelength compared to that of the Au NPs. The existence of these absorption peaks (in the near UV-visible and visible regions for Ag and Au NPs, respectively) indicate that the NPs facilitate light trapping due to the plasmonic effects inside the active layers of the devices. This particularly enhances optical response which turns

out to a boosting in the overall performance of the device. The inset of Figure 4.21 is the SEM image of the top surface showing a reasonable distribution of the 100 nm Au NPs on the GZO-coated Si substrate. The distribution density and surface coverage of the nanoparticles are estimated as 8 NPs/μm^2 and 6.28 %, respectively. The 100 nm Ag NPs might be assumed to have similar figures since the concertation of particles in the solution is almost the same for both ($3.8x10^9$ and $3.6x10^9$ particle/ml for Au and Ag NPs, respectively).

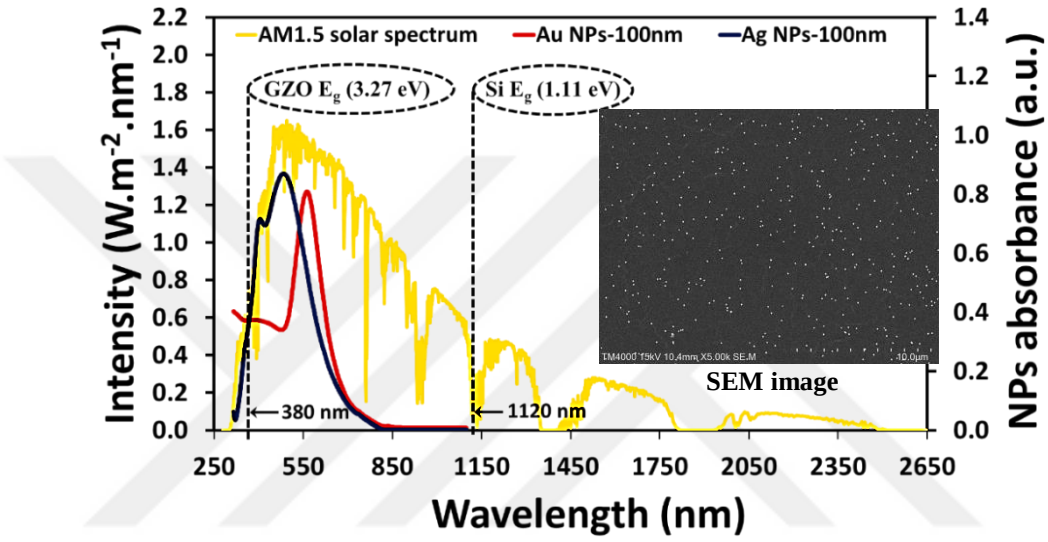


Figure 4.21: The measured absorbance spectra for the Ag and Au NPs-contained dispersions. The inset is a SEM image of the top surface of the 100 nm Au NPs deposited on the GZO-coated Si substrate.

Figure 4.22a shows the semi-log plot of the measured current-voltage (*I–V*) characteristics in the dark and under AM1.5 and UV illumination for the devices with and without metal NPs coating. As shown in Figure 4.22b, in the dark, all the devices clearly exhibit diode behavior with an excellent rectification capability and low saturation current. The rectification ratio, *RR* at ± 3V, saturation reverse current, I_o, ideality factor, *n*, and height of zero bias barrier, ϕ_{bo} parameters estimated from the dark *I-V* characteristics of devices are listed in Table 4.8. Under the illumination condition, the metal NPs-coated devices exhibit generally higher optical response compared to the bare device which reflects the contribution of metal NPs to enhance the generation of photo-carriers leading to a considerable increase in the light reverse current. Under UV illumination, the photoresponsivity, *PR*, at -3 V were 0.73 and 0.60 A/W for the Ag NPs and Au NPs-coated devices, respectively against 0.54 A/W for the bare device.

A much lower average *PR* of 0.17 A/W at -3 V was reported by C. Chen et al. for SiO_2 NPs-coated n-ZnO/p-Si photodiode [22]. It is noteworthy that Ag NPs is superior over Au NPs once they are used in the front side of the device since Ag NPs have relatively lower interband transition threshold and better wavelength dependence [22]. In our case, based on the measure of *PR*, the Ag NPs have an advantage over the Au NPs in enhancing the optical response for the device, which is consistent with those reported in the literature [22]. This result is expected since Ag NPs have an absorbance peak centered at shorter wavelength with a broad bandwidth covers part of the UV light (Figure 4.21).

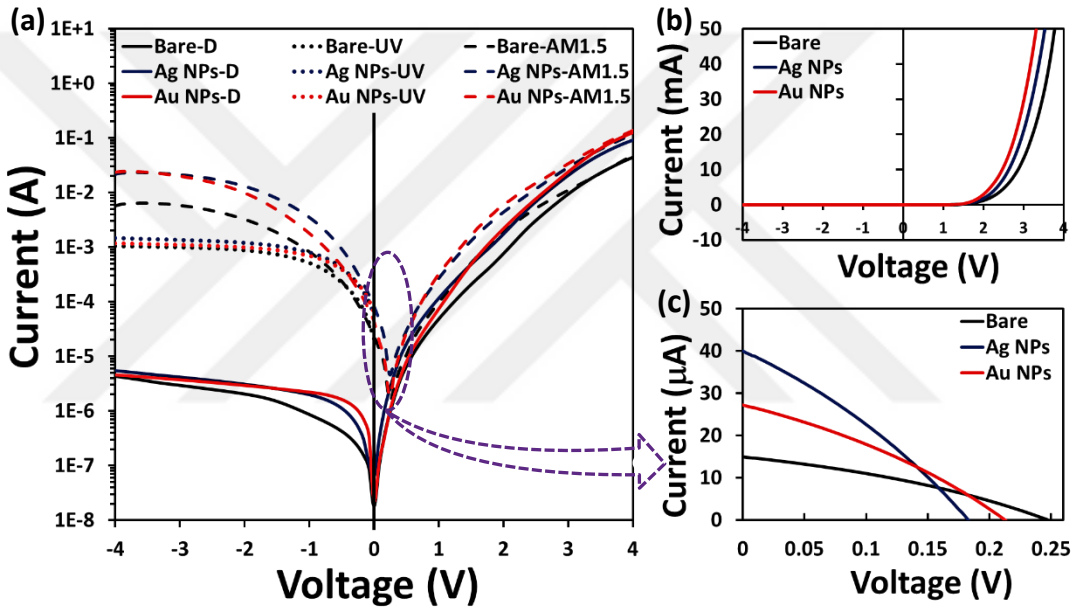


Figure 4.22: Semi-log *I-V* characteristics in the dark and under the illumination of AM1.5 and UV (reverse bias region only) (a), linear *I-V* characteristics in the dark (b), and the PV characteristics under AM1.5 illumination (c) for the metal NPs-coated devices.

Figure 4.22c shows the photovoltaic (PV) *I-V* characteristics for the devices. The PV parameters including the short circuit current, I_{sc}, open circuit voltage, V_{oc}, series resistance, R_s, and normalized efficiency, η_{norm}, are given in Table 4.9. Generally, I_{sc} is improved for the metal NPs-coated devices over the bare device showing again the potential of metal NPs in enhancing the photocurrent. As anticipated, the highest value of I_{sc} of ~ 40.1 μA belongs to the Ag NPs-coated device against 22.4 and 15.0 μA for the Au NPs-coated and bare devices, respectively. As previously explained, the Ag NPs can enhance the forward scattering of light in the near UV-visible range, this range

of wavelengths meets the portion of the highest intensity in the AM1.5 solar spectrum and contains the light spectrum of high photon energy that can be absorbed partially by GZO layer and partially by Si substrate within or close to the depletion region of GZO/Si junction. In comparison, the Au NPs can enhance the forward scattering of light of longer wavelengths that could be absorbed only by Si substrate outside the depletion region leading to less contribution to photocurrent.

Table 4.8: Bare and metal NPs-coated GZO/p-Si diodes parameters in the dark and their photoresponsivity under UV illumination

Parameter	Device		
	Bare	**Au NPs**	**Ag NPs**
RR x10^3 [at ±3 V]	8.74	12.81	7.25
I_o (nA)	35.69	40.43	119.38
n	2.84	2.94	3.00
ϕ_{bo} (V)	0.810	0.789	0.777
PR (A/W) [at -3V]	0.54	0.60	0.73

Table 4.9: PV parameters under AM1.5 illumination for the bare and metal NPs-coated GZO/p-Si devices

Parameter	Device		
	Bare	**Au NPs**	**Ag NPs**
I_{sc} (μA)	15.0	22.4	40.1
V_{oc} (mV)	250	205	185
η_{norm}	1.000	1.169	1.831
Rs (kΩ)	30.58	14.78	6.92

On the other side, as shown in Table 4.9, a decay in the open circuit voltage (V_{oc}) exists for the metal NPs-coated devices indicating a degradation in the electrical properties. Although the metal NPs could reduce the sheet resistance of GZO layer providing lower series resistance (R_s), additional surface recombination owing to the presence of the metal NPs [21] can occur, causing a decay in V_{oc}. This result reveals that the achievable enhancement in the optical properties via the metal NPs coating comes at the expense of degrading some electrical properties. Table 4.9 shows the normalized values of the PV conversion efficiency (η_{norm}). In the overall, the decay in V_{oc} is well compensated with the enhancement in I_{sc}. Compared to the bare device, the PV conversion efficiency increased by 83.1 % and 16.9 % for the Ag NPs and Au NPs-coated devices, respectively.

CHAPTER 5

Conclusions

Undoped ZnO, Al-doped (AZO) and Ga-doped ZnO (GZO) thin films were successfully prepared by sol-gel method spin coating technique. The films were characterized by XRD and SEM, AFM, UV-vis spectroscopy, the four-point probe and Hall effect measurement systems. All the deposited films exhibited highly preferred crystal orientation corresponding to (002) plane with very smooth and uniform surface. A competitive quality in terms of optical and electrical properties was obtained for the prepared AZO and GZO thin films. The highest values of average visible transmittance and electrical conductivity were obtained at 1 and 3 atomic percentage of doping ratio for the AZO and GZO films, respectively. At the optimum doping ratios, figure of merit (*FOM*) value of ~1.6×10^{-5} Ω^{-1} was measured for the deposited AZO and GZO thin films. This value of *FOM* corresponds average visible transmittance of ~87 and ~84 % and electrical resistivity of 47.72×10^{-2} and 38.97×10^{-2} Ω.m for the AZO and GZO films, respectively. Despite the achieved quality of the deposited films was competitive to that in the literature, much better quality would have been achievable by applying the step of post-annealing under vacuum and controlled environment which was unfortunately not available in our lab. Applying this step can significantly improve the electrical conductivity of the films due to the outgassing of oxygen from the film and into the vacuum ambient. Outgassing of oxygen severs bonds, creating oxygen deficiencies in the film and frees electrons resulting an increase in the carrier concentration.

The optical and electrical properties of the films were optimized by altering many parameters of sol-gel process. Among the investigated parameters, the type of solvent-stabilizer combination was found crucial in determining the structural properties and consequently the optical and electrical properties of the films. Based on *FOM* measure, the best quality for the films was obtained using the ethanol-MEA combination. The spin acceleration time was also found as an important parameter for controlling some properties of the films. With varying the spin acceleration time, no significant change in grain size and band gap energy of the films was observed. On contrary, a remarkable

change was asserted in strain, porosity, and surface roughness. Also, a variation in the resistivity closely connected to the change in these parameters was unambiguously confirmed.

As an application for the optimized GZO thin films, GZO/p-Si heterojunction-based photoelectric devices were successfully fabricated. The performance of devices was characterized by the current-voltage (*I*-*V*) measurements performed in the dark and under AM1.5 and UV illumination conditions. The fabricated devices were optimized in many aspects including GZO layer parameters (doping ratio and thickness), ohmic contact realization of front and back metallization, and conditions and sequence of fabrication process steps. Among these aspects, the device performance was found to be strongly affected by tuning the thickness and doping ratio of the GZO layer. Due to its porosity and nanocrystalline microstructure, GZO layer has high concentration of bulk defect states which significantly hinder the transportation of free charges and reduce the diffusion length of minority carriers. Accordingly, a comparable thickness of GZO layer is required for facilitating the collection of photogenerated carriers at the electrodes. In addition, it is required for GZO layer to background carrier concentration higher than that of p-Si substrate in order to make the depletion region more extended into p-Si side of GZO/p-Si junction. Good performance was obtained for the devices of GZO layer having thickness of ~80 nm and doping ratio of 3 at. % (corresponds the highest electrical conductivity of GZO film). GZO layer of such thickness can act as both an active n-type semiconductor and an antireflection coating layer with Si substrate. Ag and Al metals were used for realization of ohmic contact for the front and back electrodes, respectively. The ohmic behavior of Ag/GZO and p-Si/Al contacts were experimentally approved.

Compared to the published results, the optimized devices exhibited excellent rectification behavior, remarkably high optical response, and competitive photovoltaic property. Rectification ratio value of 8.74×10^3 at ±3 V was measured under dark condition and photoresponsivity values of 0.54 and 0.12 A/W were measured at -3 V under UV and AM1.5 illuminations, respectively. The devices are more sensitivity to UV light which is anticipated since the UV spectrum can be fully absorbed within the depletion region of the device providing higher contribution to photocurrent. From the photovoltaic current-voltage (*I*-*V*) characteristics measured for the devices under

AM1.5 illumination, the obtained values for the open circuit voltage and the short circuit current were 250 mV and 15 μA, respectively. The devices generally exhibited low performance of photovoltaic property which could be attributed mainly to the high series resistance and the high recombination rate of the photogenerated carriers.

For investigating the potential of metal nanoparticles (NPs) in enhancing their optical response, GZO/p-Si heterojunction-based devices with incorporation of metal nanoparticles (NPs) were fabricated. Solution-processed 100 nm Ag and Au NPs were spin-coated on the top of GZO layer before metallization. The results clearly showed an improvement in performance of the metal NPs-coated devices over the devices without metal NPs in terms of optical response. This proves that the plasmonic effect of the metal NPs allows for additional forward scattering and injecting more light into the device permitting higher light absorption. It was found that the Ag NPs are superior over Au NPs in enhancing the optical response of the devices. Under UV illumination, the Ag NPs-coated devices exhibited remarkably high photoresponsivity of 0.73 A/W at -3V against 0.60 and 0.54 A/W for the Au NPs-coated and without NPs devices, respectively. According to our survey, this value of photoresponsivity (0.73 A/W) is higher than that reported in the literature so far for the ZnO/p-Si heterojunction-based photodiodes. In terms of photovoltaic property, significant improvement of 167.3 % in the short circuit current and 83.1 % in the photovoltaic conversion efficiency were obtained for the Ag NPs-coated devices over the devices without metal NPs. On the hand, a decay in the open circuit voltage was measured for metal NPs-coated devices indicating a degradation in the electrical properties. Although the metal NPs could reduce the sheet resistance of GZO layer providing lower series resistance, additional surface recombination owing to the presence of the metal NPs can occur, causing a decay in the open circuit voltage. This result reveals that the achievable enhancement in the optical properties via the metal NPs coating comes at the expense of degrading some electrical properties.

For further work on GZO/p-Si heterojunction-based devices, the following main issues can be investigated in purpose of improving the performance of these device:

- Improving the quality of GZO films in term of the structural and electrical properties. In principle, GZO layer of high crystallite quality characterized with

high carrier concentration (higher than that of the p-Si substrate) is required for solar cells applications. Such high quality GZO layer can provide reduced bulk carrier recombination and higher generation rate and collection of photogenerated carriers in addition to reduced series resistance of device.

- Reducing the recombination of photogenerated carriers through:
  1. Introducing intermediate layer between the GZO layer and Si substrate for reducing the interface defect states that result from the lattice mismatch at the GZO/p-Si junction. Amorphous undoped ZnO can be an option in this regard.
  2. Top surface passivation of GZO layer.
- Reducing the series resistance through:
  1. Efficient ohmic contact for front and back electrodes.
  2. Proper design and application of front grid.
- Enhancing the coupling of light into device via the application of light trapping techniques including surface texturing of Si substrate, antireflection coating, and introducing of metal NPs.

REFERENCES

[1] Janotti, A., & Van de Walle, C. G. (2009). Fundamentals of zinc oxide as a semiconductor. *Reports on progress in physics*, *72*(12), 126501.

[2] Jun, M. C., Park, S. U., & Koh, J. H. (2012). Comparative analysis of Al-doped ZnO and Ga-doped ZnO thin films. *Integrated Ferroelectrics*, *140*(1), 166-176.

[3] Chen, S., Warwick, M. E., & Binions, R. (2015). Effects of film thickness and thermal treatment on the structural and opto-electronic properties of Ga-doped ZnO films deposited by sol–gel method. *Solar Energy Materials and Solar Cells*, *137*, 202-209.

[4] Varol, S. F., Babür, G., Çankaya, G., & Kölemen, U. (2014). Synthesis of sol-gel derived nano-crystalline ZnO thin films as TCO window layer: effect of sol aging and boron. *RSC Advances*, *4*(100), 56645-56653.

[5] Serrao, F. J., Sandeep, K. M., & Dharmaprakash, S. M. (2016). Annealing-induced modifications in sol–gel spin-coated Ga: ZnO thin films. *Journal of Sol-Gel Science and Technology*, *78*(2), 438-445.

[6] Al Dahoudi, N. (2014). Comparative study of highly dense aluminium-and gallium-doped zinc oxide transparent conducting sol-gel thin films. *Bulletin of Materials Science*, *37*(6), 1243-1248.

[7] Yoon, H., Kim, S., Park, H., Nam, G., Kim, Y., Leem, J. Y., ... & Park, Y. (2014). Effects of Ga concentration on the structural, electrical and optical properties of Ga-doped ZnO thin films grown by sol-gel method. *Journal of the Korean Physical Society*, *64*(1), 109-113.

[8] Ebrahimifard, R., Golobostanfard, M. R., & Abdizadeh, H. (2014). Sol-gel derived Al and Ga co-doped ZnO thin films: An optoelectronic study. *Applied Surface Science*, *290*, 252-259.

[9] Paul, G. K., & Sen, S. K. (2002). Sol-gel preparation, characterization and studies on electrical and thermoelectrical properties of gallium doped zinc oxide films. *Materials letters*, *57*(3), 742-746.

[10] Tsay, C. Y., Fan, K. S., & Lei, C. M. (2012). Synthesis and characterization of sol–gel derived gallium-doped zinc oxide thin films. *Journal of alloys and compounds*, *512*(1), 216-222.

[11] Houng, B., Huang, C. L., & Tsai, S. Y. (2007). Effect of the pH on the growth and properties of sol-gel derived boron-doped ZnO transparent conducting thin film. *Journal of Crystal Growth*, *307*(2), 328-333.

[12] Kim, S., Yoon, H., Kim, D. Y., Kim, S. O., & Leem, J. Y. (2013). Optical properties and electrical resistivity of boron-doped ZnO thin films grown by sol-gel dip-coating method. *Optical Materials*, *35*(12), 2418-2424.

[13] Tsay, C. Y., & Hsu, W. T. (2013). Sol-gel derived undoped and boron-doped ZnO semiconductor thin films: preparation and characterization. *Ceramics International*, *39*(7), 7425-7432.

[14] Chaitra, U., Kekuda, D. & Rao, K.M. (2017). Effect of annealing temperature on the evolution of structural, microstructural, and optical properties of spin coated ZnO thin films. *Ceramics International*, *43*(9), 7115-7122.

[15] Yildiz, A., Cansizoglu, H., Turkoz, M., Abdulrahman, R., Al-Hilo, A., Cansizoglu, M. F., ... & Karabacak, T. (2015). Glancing angle deposited Al-doped ZnO nanostructures with different structural and optical properties. *Thin solid films*, *589*, 764-769.

[16] Wang, F. H., & Chang, C. L. (2016). Effect of substrate temperature on transparent conducting Al and F co-doped ZnO thin films prepared by rf magnetron sputtering. *Applied Surface Science*, *370*, 83-91.

[17] Edalati, K., Shakiba, A., Vahdati-Khaki, J., & Zebarjad, S. M. (2016). Low-temperature hydrothermal synthesis of ZnO nanorods: Effects of zinc salt concentration, various solvents and alkaline mineralizers. *Materials Research Bulletin*, *74*, 374-379.

[18] Vajargah, P. H., Abdizadeh, H., Ebrahimifard, R., & Golobostanfard, M. R. (2013). Sol-gel derived ZnO thin films: effect of amino-additives. *Applied Surface Science*, *285*, 732-743.

[19] Patil, S. L., Chougule, M. A., Pawar, S. G., Raut, B. T., Sen, S., & Patil, V. B. (2011). New process for synthesis of ZnO thin films: Microstructural, optical and electrical characterization. *Journal of Alloys and Compounds*, *509*(41), 10055-10061.

[20] Yildiz, A., Cansizoglu, H., Abdulrahman, R., & Karabacak, T. (2015). Effect of grain size and strain on the bandgap of glancing angle deposited AZO nanostructures. *Journal of Materials Science: Materials in Electronics*, *26*(8), 5952-5957.

[21] Ko, Y. U., Yun, H. J., Jeong, K. S., Kim, Y. M., Yang, S. D., Kim, S. H., ... & Lee, G. W. (2015). Enhanced photo current in n-ZnO/p-Si diode via embedded Ag nanoparticles for the solar cell application. *Journal of Semiconductor Technology and Science*, *15*(1), 35-40.

[22] Chen, C. P., Lin, P. H., Chen, L. Y., Ke, M. Y., Cheng, Y. W., & Huang, J. (2009). Nanoparticle-coated n-ZnO/p-Si photodiodes with improved photoresponsivities and acceptance angles for potential solar cell applications. *Nanotechnology*, *20*(24), 245204.

[23] Jeong, I. S., Kim, J. H., & Im, S. (2003). Ultraviolet-enhanced photodiode employing n-ZnO/p-Si structure. *Applied physics letters*, *83*(14), 2946-2948.

[24] Hussain, B., Ebong, A., & Ferguson, I. (2015). Zinc oxide as an active n-layer and antireflection coating for silicon based heterojunction solar cell. *Solar Energy Materials and Solar Cells*, *139*, 95-100.

[25] Shen, L., Ma, Z. Q., Shen, C., Li, F., He, B., & Xu, F. (2010). Studies on fabrication and characterization of a ZnO/p-Si-based solar cell. *Superlattices and microstructures*, *48*(4), 426-433.

[26] Wei-Ying, Z., Sheng, Z., Li-Jie, S., & Zhu-Xi, F. (2008). Dependence of photovoltaic property of ZnO/Si heterojunction solar cell on thickness of ZnO films. *Chinese Physics Letters*, *25*(5), 1829.

[27] Zhang, W., LIUa, Z. H. E. N. Z. H. O. N. G., HANa, Y. U. N. X. I. A., & FUb, Z. H. U. X. I. (2010). Effect of doping concentration on photovoltaic property of ZnO: Al/Si heterojunction. *Optoelectronics and Advanced Materials-Rapid Communications*, *4*(5), 681-684.

[28] Bhat, S., S., B. V., & Gopalakrishna Naik, K. (2016). Temperature dependent electrical properties of n-ZnO/p-Si heterojunction prepared by spray pyrolysis growth of ZnO thin film on p-Si. *IOSR Journal of Applied Physics*, *8*(2), 126-130.

[29] Hussain, B. (2017). Improvement in open circuit voltage of n-ZnO/p-Si solar cell by using amorphous-ZnO at the interface. *Progress in Photovoltaics: Research and Applications*, *25*(11), 919-927.

[30] Karataş, Ş., El-Nasser, H.M., Al-Ghamdi, A.A. & Yakuphanoglu, F. (2018). High photoresponsivity Ru-doped ZnO/p-Si heterojunction diodes by the sol-gel method. *Silicon*, *10*(2), 651-658.

[31] Singh, S.K., Hazra, P., Tripathi, S. & Chakrabarti, P. (2016). Performance analysis of RF-sputtered ZnO/Si heterojunction UV photodetectors with high photo-responsivity. *Superlattices and Microstructures*, *91*, 62-69.

[32] Atwater, H.A. & Polman, A. (2010). Plasmonics for improved photovoltaic devices. *Nature materials*, *9*(3), 205.

[33] Islam, K., Alnuaimi, A., Battal, E., Okyay, A. K. & Nayfeh, A. (2014). Effect of gold nanoparticles size on light scattering for thin film amorphous-silicon solar cells. *Solar Energy*, *103***,** 263.

[34] Shokeen, P., Jain, A., & Kapoor, A. (2017). Plasmonic ZnO/p-silicon heterojunction solar cell. *Optical Materials*, *67*, 32-37.

[35] Beck, F. J., Polman, A., & Catchpole, K. R. (2009). Tunable light trapping for solar cells using localized surface plasmons. *Journal of Applied Physics*, *105*(11), 114310.

[36] Derkacs, D., Lim, S. H., Matheu, P., Mar, W., & Yu, E. T. (2006). Improved performance of amorphous silicon solar cells via scattering from surface plasmon polaritons in nearby metallic nanoparticles. *Applied Physics Letters*, *89*(9), 093103..

[37] Look, D. C., Claflin, B. B., Kiefer, A. M., & Leedy, K. D. (2014). Interfacial properties of Ga-doped ZnO thin films on Si. *Optical Engineering*, *53*(8), 087108.

[38] Chen, C. P., Lin, P. H., Hung, Y. J., Hsu, S. S., Chen, L. Y., Cheng, Y. W. & Kuo, H. C. (2010). Investigation of light absorption properties and acceptance angles of nanopatterned GZO/a-Si/p+-Si photodiodes. *Nanotechnology*, *21*(21), 215201.

[39] Izyumskaya, N., Avrutin, V., Özgür, Ü., Alivov, Y. I., & Morkoç, H. (2007). Preparation and properties of ZnO and devices. *Physica Status Solidi (b)*, *244*(5), 1439-1450.

[40] Ohtomo, A., Kawasaki, M., Koida, T., Masubuchi, K., Koinuma, H., Sakurai, Y., ... & Segawa, Y. (1998). $Mg_xZn_{1-x}O$ as a II–VI widegap semiconductor alloy. *Applied Physics Letters*, *72*(19), 2466-2468.

[41] Jin, Y., Zhang, B., Yang, S., Wang, Y., Chen, J., Zhang, H., ... & Chang, R. P. (2001). Room temperature UV emission of $Mg_xZn_{1-x}O$ films. *Solid State Communications*, *119*(6), 409-413.

[42] Stavola, M., Weber, E. R., & Willardson, R. K. (1998). *Identification of defects in semiconductors*. Elsevier Science.

[43] Hu, J., & Gordon, R. G. (1992). Textured aluminum-doped zinc oxide thin films from atmospheric pressure chemical-vapor deposition. *Journal of Applied Physics*, *71*(2), 880-890.

[44] Hu, J., & Gordon, R. G. (1992). Atmospheric pressure chemical vapor deposition of gallium doped zinc oxide thin films from diethyl zinc, water, and triethyl gallium. *Journal of Applied Physics*, *72*(11), 5381-5392.

[45] Jagadish, C., & Pearton, S. J. (Eds.). (2011). *Zinc oxide bulk, thin films and nanostructures: processing, properties, and applications*. Elsevier.

[46] Brinker, C. J., & Scherer, G. W. (2013). *Sol-gel science: the physics and chemistry of sol-gel processing*. Academic press.

[47] Danks, A. E., Hall, S. R., & Schnepp, Z. (2016). The evolution of 'sol-gel'chemistry as a technique for materials synthesis. *Materials Horizons*, *3*(2), 91-112.

[48] Bahadur, H., Srivastava, A. K., Sharma, R. K., & Chandra, S. (2007). Morphologies of sol-gel derived thin films of ZnO using different precursor materials and their nanostructures. *Nanoscale Research Letters*, *2*(10), 469.

[49] Murali, K. R. (2007). Properties of sol-gel dip-coated zinc oxide thin films. *Journal of Physics and Chemistry of Solids*, *68*(12), 2293-2296.

[50] Sahal, M., Hartiti, B., Ridah, A., Mollar, M., & Mari, B. (2008). Structural, electrical and optical properties of ZnO thin films deposited by sol-gel method. *Microelectronics Journal*, *39*(12), 1425-1428.

[51] Miller, J. B., Hsieh, H. J., Howard, B. H., & Broitman, E. (2010). Microstructural evolution of sol-gel derived ZnO thin films. *Thin Solid Films*, *518*(23), 6792-6798.

[52] Li, H., Wang, J., Liu, H., Yang, C., Xu, H., Li, X., & Cui, H. (2004). Sol-gel preparation of transparent zinc oxide films with highly preferential crystal orientation. *Vacuum*, *77*(1), 57-62.

[53] Znaidi, L., Illia, G. S., Le Guennic, R., Sanchez, C., & Kanaev, A. (2003). Elaboration of ZnO thin films with preferential orientation by a soft chemistry route. *Journal of Sol-Gel Science and Technology*, *26*(1-3), 817-821.

[54] Norrman, K., Ghanbari-Siahkali, A., & Larsen, N. B. (2005). 6 Studies of spin-coated polymer films. *Annual Reports Section "C" (Physical Chemistry)*, *101*, 174-201.

[55] Ahmad, T., & Khan, W. (2013). Size variation of gold nanoparticles synthesized using tannic acid in response to higher chloroauric acid concentrations. *World Journal of Nano Science and Engineering*, *3*(03), 62.

[56] García, M. A. (2011). Surface plasmons in metallic nanoparticles: fundamentals and applications. *Journal of Physics D: Applied Physics*, *44*(28), 283001.

[57] Thouti, E., Chander, N., Dutta, V., & Komarala, V. K. (2013). Optical properties of Ag nanoparticle layers deposited on silicon substrates. *Journal of Optics*, *15*(3), 035005.

[58] Lu, X., Rycenga, M., Skrabalak, S. E., Wiley, B., & Xia, Y. (2009). Chemical synthesis of novel plasmonic nanoparticles. *Annual review of physical chemistry*, *60*, 167-192.

[59] Catchpole, K. A., & Polman, A. (2008). Plasmonic solar cells. *Optics express*, *16*(26), 21793-21800.

[60] Lozano, G., Louwers, D. J., Rodríguez, S. R., Murai, S., Jansen, O. T., Verschuuren, M. A., & Rivas, J. G. (2013). Plasmonics for solid-state lighting: enhanced excitation and directional emission of highly efficient light sources. *Light: Science & Applications*, *2*(5), e66.

[61] Yakuphanoglu, F., Caglar, Y., Caglar, M., & Ilican, S. (2010). ZnO/p-Si heterojunction photodiode by sol-gel deposition of nanostructure n-ZnO film on p-Si substrate. *Materials Science in Semiconductor Processing*, *13*(3), 137-140.

[62] Streetman, B. G., & Banerjee, S. (1995). *Solid state electronic devices* (Vol. 4). Englewood Cliffs, NJ: Prentice Hall.

[63] Muller, R. S., Kamins, T. I., Sah, C. T., Singh, J., Pierret, R. F., Neudeck, G. W., & Neamen, D. A. (2006). Device Electronics for Integrated Circuits.

[64] Neamen, D. A. (2012). *Semiconductor physics and devices: basic principles*. New York, NY: McGraw-Hill,.

[65] Bücher, K., Bruns, J., & Wagemann, H. G. (1994). Absorption coefficient of silicon: An assessment of measurements and the simulation of temperature variation. *Journal of applied Physics*, *75*(2), 1127-1132.

[66] Jäger, K. D., Isabella, O., Smets, A. H., van Swaaij, R. A., & Zeman, M. (2016). *Solar Energy: Fundamentals, Technology and Systems*. UIT Cambridge.

[67] http://www.osioptoelectronics.com/application-notes/AN-Photodiode-Parameters-Characteristics.pdf

[68] Sbeta, M., Atilgan, A., Atli, A. & Yildiz, A. (2018). Influence of the spin acceleration time on the properties of ZnO: Ga thin films deposited by sol-gel method. *Journal of Sol-Gel Science and Technology*, *86*(2), 513-520.

[69] Schroder, D. K. (2006). *Semiconductor material and device characterization*. John Wiley & Sons.

[70] Tsay, C. Y., & Lee, W. C. (2013). Effect of dopants on the structural, optical and electrical properties of sol-gel derived ZnO semiconductor thin films. *Current Applied Physics*, *13*(1), 60-65.

[71] Grobelny, J., DelRio, F. W., Pradeep, N., Kim, D. I., Hackley, V. A., & Cook, R. F. (2011). Size measurement of nanoparticles using atomic force microscopy. In *Characterization of nanoparticles intended for drug delivery* (pp. 71-82). Humana Press.

[72] Gobrecht, A., Bendoula, R., Roger, J. M., & Bellon-Maurel, V. (2015). Combining linear polarization spectroscopy and the Representative Layer Theory to measure the Beer–Lambert law absorbance of highly scattering materials. *Analytica chimica acta*, *853*, 486-494.

[73] Swanepoel, R. (1983). Determination of the thickness and optical constants of amorphous silicon. *Journal of Physics E: Scientific Instruments*, *16*(12), 1214.

[74] Varol, S. F., Babür, G., Çankaya, G., & Kölemen, U. (2014). Synthesis of sol-gel derived nano-crystalline ZnO thin films as TCO window layer: effect of sol aging and boron. *RSC Advances*, *4*(100), 56645-56653.

[75] Kara, I. L. K. E. R., Atilgan, A., Serin, T., & Yildiz, A. (2017). Effects of Co and Cu dopants on the structural, optical, and electrical properties of ZnO nanocrystals. *Journal of Materials Science: Materials in Electronics*, *28*(8), 6088-6092.

[76] Smits, F. M. (1958). Measurement of sheet resistivities with the four-point probe. *Bell System Technical Journal*, *37*(3), 711-718.

[77] Gordon, R. G. (2000). Criteria for choosing transparent conductors. *MRS bulletin*, *25*(8), 52-57.

[78] Keskenler, E. F., Tomakin, M., Doğan, S., Turgut, G., Aydın, S., Duman, S., & Gürbulak, B. (2013). Growth and characterization of Ag/n-ZnO/p-Si/Al heterojunction diode by sol–gel spin technique. *Journal of Alloys and Compounds*, *550*, 129-132.

[79] Chabane, L., Zebbar, N., Trari, M., & Kechouane, M. (2017). Opto-capacitive study of n-ZnO/p-Si heterojunctions elaborated by reactive sputtering method: Solar cell applications. *Thin Solid Films*, *636*, 419-424.

[80] Ghosh, R., Basak, D., & Fujihara, S. (2004). Effect of substrate-induced strain on the structural, electrical, and optical properties of polycrystalline ZnO thin films. *Journal of Applied Physics*, *96*(5), 2689-2692.

[81] Valle, G. G., Hammer, P., Pulcinelli, S. H., & Santilli, C. V. (2004). Transparent and conductive ZnO: Al thin films prepared by sol-gel dip-coating. *Journal of the European Ceramic Society*, *24*(6), 1009-1013.

[82] Ko, H., Tai, W. P., Kim, K. C., Kim, S. H., Suh, S. J., & Kim, Y. S. (2005). Growth of Al-doped ZnO thin films by pulsed DC magnetron sputtering. *Journal of Crystal Growth*, *277*(1-4), 352-358.

[83] Tsay, C. Y., Wu, C. W., Lei, C. M., Chen, F. S., & Lin, C. K. (2010). Microstructural and optical properties of Ga-doped ZnO semiconductor thin films prepared by sol-gel process. *Thin Solid Films*, *519*(5), 1516-1520.

[84] Cheong, K. Y., Muti, N., & Ramanan, S. R. (2002). Electrical and optical studies of ZnO: Ga thin films fabricated via the sol-gel technique. *Thin Solid Films*, *410*(1-2), 142-146.

[85] de Souza Gonçalves, A., de Lima, S. A. M., Davolos, M. R., Antoˆnio, S. G., & de Oliveira Paiva-Santos, C. (2006). The effects of $ZnGa_2O_4$ formation on structural and optical properties of ZnO: Ga powders. *Journal of Solid State Chemistry*, *179*(5), 1330-1334.

[86] Serin, T., Atilgan, A., Kara, I., & Yildiz, A. (2017). Electron transport in Al-Cu co-doped ZnO thin films. *Journal of Applied Physics*, *121*(9), 095303.

[87] Yildiz, A., Uzun, S., Serin, N., & Serin, T. (2016). Influence of grain boundaries on the figure of merit of undoped and Al, In, Sn doped ZnO thin films for photovoltaic applications. *Scripta Materialia*, *113*, 23-26.

[88] Bandyopadhyay, S., Paul, G. K., Roy, R., Sen, S. K., & Sen, S. (2002). Study of structural and electrical properties of grain-boundary modified ZnO films prepared by sol-gel technique. *Materials Chemistry and Physics*, *74*(1), 83-91.

[89] Farrag, A. A. G., & Balboul, M. R. (2017). Nano ZnO thin films synthesis by sol-gel spin coating method as a transparent layer for solar cell applications. *Journal of Sol-Gel Science and Technology*, *82*(1), 269-279.

[90] Kaur, G., Mitra, A., & Yadav, K. L. (2015). Pulsed laser deposited Al-doped ZnO thin films for optical applications. *Progress in Natural Science: Materials International*, *25*(1), 12-21.

[91] Atthi, N., Nimittrakoolchai, O. U., Jeamsaksiri, W., Supothina, S., Hruanun, C., & Poyai, A. (2009). Study of optimization condition for spin coating of the photoresist film on rectangular substrate by Taguchi design of an experiment. *Songklanakarin J. Sci. Technol*, *31*(3), 331-335.

[92] Yildiz, A., Ozturk, E., Atilgan, A., Sbeta, M., Atli, A., & Serin, T. (2017). An understanding of the band gap shrinkage in Sn-doped ZnO for dye-sensitized solar cells. *Journal of Electronic Materials*, *46*(12), 6739-6744.

[93] Kobayashi, H., Mori, H., Ishida, T., & Nakato, Y. (1995). Zinc oxide/n-Si junction solar cells produced by spray-pyrolysis method. *Journal of applied physics*, *77*(3), 1301-1307.

[94] Baik, D. G., & Cho, S. M. (1999). Application of sol-gel derived films for ZnO/n-Si junction solar cells. *Thin Solid Films*, *354*(1-2), 227-231.

[95] Hassan, M. A. M., Saleh, A. F., & Mezher, S. J. (2014). Energy band diagram of In: ZnO/p-Si structures deposited using chemical spray pyrolysis technique. *Applied Nanoscience*, *4*(6), 695-701.

[96] https://refractiveindex.info/?shelf=other&book=Al-nO&page=Treharn

[97] Ay, I., & Tolunay, H. (2007). The influence of ohmic back contacts on the properties of a-Si: H Schottky diodes. *Solid-state electronics*, *51*(3), 381-386.

[98] Ilican, S., Gorgun, K., Caglar, Y., & Caglar, M. (2017). Influence of irradiation time on structural, morphological properties of ZnO-NRs films deposited by MW-CBD and their photodiode applications. *Journal of Nanomaterials*, *2017*.

[99] Orak, I., Kocyigit, A., & Turut, A. (2017). The surface morphology properties and respond illumination impact of ZnO/n-Si photodiode by prepared atomic layer deposition technique. *Journal of Alloys and Compounds*, *691*, 873-879.

[100] Mridha, S., Dutta, M., & Basak, D. (2009). Photoresponse of n-ZnO/p-Si heterojunction towards ultraviolet/visible lights: thickness dependent behavior. *Journal of Materials Science: Materials in Electronics*, *20*(1), 376-379.

[101] Lu, Y., Huang, J., Li, B., Tang, K., Ma, Y., Cao, M., ... & Wang, L. (2018). A boron and gallium co-doped ZnO intermediate layer for ZnO/Si heterojunction diodes. *Applied Surface Science*, *428*, 61-65.

[102] Tsay, C. Y., & Hsu, W. T. (2017). Comparative studies on ultraviolet-light-derived photoresponse properties of ZnO, AZO, and GZO transparent semiconductor thin films. *Materials*, *10*(12), 1379.

[103] Hendi, A. A. (2015). Electrical and photoresponse properties of graphene oxide: ZnO/Si photodiodes. *Journal of Alloys and Compounds*, *647*, 259-264.

[104] Baydogan, N., Karacasu, O., & Cimenoglu, H. (2012). Effect of annealing temperature on ZnO: Al/p-Si heterojunctions. *Thin Solid Films*, *520*(17), 5790-5796.

[105] Bo, H., Quan, M. Z., Jing, X., Lei, Z., Sheng, Z. N., Feng, L., ... & Ting, Y. Y. (2009). Characterization of AZO/p-Si heterojunction prepared by DC magnetron sputtering. *Materials Science in Semiconductor Processing*, *12*(6), 248-252.

[106] Park, C. H., Lee, J. Y., Im, S., & Kim, T. G. (2003). n-ZnO/p-Si photodiodes fabricated using ion-beam induced isolation technique. *Nuclear Instruments and Methods in Physics Research Section B: Beam Interactions with Materials and Atoms*, *206*, 432-435.

CURRICULUM VITAE

PERSONAL INFORMATION



Name Surname : Mohamed Nouri Sbeta

Date of Birth : 18/05/1968

Phone : 05414399687

E-mail : sbita6@yahoo.com

EDUCATION

High School : (1986) Shuhada Al-ddamur, Tripoli-Libya

Bachelor : (1992) Tripoli University, Tripoli-Libya

Master's degree : (2006) Libyan Academy, Tripoli-Libya

WORK EXPERIENCE

1995 up to date : Researcher at Center for Solar Energy Research and Studies, Tripoli-Libya

1993-1995 : Engineer At the General Company for Computers, Tripoli-Libya

TOPICS OF INTEREST

- Electronics
- Solar cells physics and technology
- Thin films technology
- Photovoltaic systems

PUBLICATION

1- **M. Sbeta** and A. Yildiz, "Optical Response Enhancement of GZO/p-Si Heterostructures via Metal Nanoparticles", Material Research Express 6 (2019) 058018.

2- I. K. Er, T. Nurtayeva, **M. Sbeta**, A. O. Cagirtekin, S. Acar and A. Yildiz, “Carbon monoxide gas sensing performance of ZnO: Al thin films prepared using different solvent–stabilizer combinations”, Journal of Materials Science: Materials in Electronics (2019) 1-11.

3- N. Koksal, **M. Sbeta**, and Abdullah Yildiz, 2019 “GZO/Si Photodiodes Exhibiting High Photocurrent-to-Dark-Current Ratio”, IEEE Transactions on Electron Devices, Vol. 66, No. 5 (2019).

4- S. Horzum, F. Iyikanat, R. T. Senger, C. Çelebi, **M. Sbeta**, A. Yildiz, T. Serin, “Monitoring the characteristic properties of Ga-doped ZnO by Raman spectroscopy and atomic scale calculations”, Journal of Molecular Structure 1180 (2019) 505-511.

5- **M. Sbeta** and A. Yildiz, “Determination of the critical carrier concentration for the metal-insulator in Ga-doped ZnO”, Journal of Materials Science: Materials in Electronics 29 (2018) 14111-14115.

6- **M. Sbeta**, A. Atilgan, A. Atli, A. Yildiz, “Influence of the spin acceleration time on the properties of ZnO:Ga films deposited by sol-gel method”, Journal of Sol-Gel Science and Technology 86 (2018) 513-520.

7- A. Yildiz, E. Ozturk, A. Atilgan, **M. Sbeta**, A. Atli, T. Serin, "An understanding of the band gap shrinkage in Sn-doped ZnO for dye-sensitized solar cells", Journal of Electronic Materials 46 (2017) 6739.

8- **M. Sbeta** and S. Sasi, “On the field performance of PV water pumping system in libya”, Journal of Solar Energy and Sustainable Development, Vol. 1, No. 1 (2012) 1-7.

9- **M. Sbeta**, “Equipment of thin film silicon solar cells" (Arabic), Journal of Solar Energy and Sustainable Development, Volume 1, No. 1 (2012) 7-16.

10- K. Agha and **M. Sbeta**, “On the sizing parameters of stand-alone solar energy systems”, Journal of Applied Energy 65 (2000) 73-84.